# Characterization of Single- and Multi-antenna Wireless Channels

Wyne, Shurjeel

2009

*Citation for published version (APA):*
Wyne, S. (2009). *Characterization of Single- and Multi-antenna Wireless Channels*. [Doctoral Thesis (compilation), Department of Electrical and Information Technology].

*Total number of authors:*
1

# Characterization of Single- and Multi-Antenna Wireless Channels

Shurjeel Wyne

Lund 2009

Department of Electrical and Information Technology
Lund University
Box 118, SE-221 00 LUND
SWEDEN

Series of licentiate and doctoral theses
No. 15
ISSN 1654-790X

Printed in Sweden by *Tryckeriet i E-huset*, Lund.
February 2009.

# Abstract

The wireless propagation channel significantly influences the received signal, so that it needs to be modeled effectively. Extensive measurements and analysis are required for investigating the validity of theoretical models and postulating new models based on measurements. Such measurements, analysis, and modeling are the topic of this thesis. The focus of the included contributions are Multiple-Input Multiple-Output (MIMO) propagation channels and radio channels for sensor network applications.

Paper I presents results from one of the first MIMO measurements for a double-directional characterization of the outdoor-to-indoor wireless propagation channel. Such channels are of interest for both cellular and wireless LAN applications. We discuss physical aspects of building penetration, and also provide statistics of angle and delay spreads in the channel. The paper also investigates the coupling between DOD and DOA and the two spectra are found to have non-negligible dependence. We test the applicability of three analytical channel models that make different assumptions on the coupling between DODs and DOAs. Our results indicate that analytical models, that impose fewer restrictions on the DOD to DOA coupling, should be used preferrably over models such as the Kronecker model that have more restrictive assumptions.

Paper II presents a cluster-based analysis of the outdoor-to-indoor MIMO measurements analyzed in Paper I. A subset of parameters of the COST 273 channel model, a generic model for MIMO propagation channels, are characterized for the outdoor-to-indoor scenario. MPC parameters are extracted at each measured location using a high-resolution algorithm and clusters of MPCs are identified with an automated clustering approach. In particular, the adopted clustering approach requires that *all* MPC parameters must be similar in order for the MPCs to form a cluster. A statistical analysis of the identified clusters is performed for both the intra- and inter-cluster properties.

Paper III analyzes the spatial fading distribution for a range of canonical sensor deployment scenarios. The presented results are relevant to communicating within, and between, clusters of nodes. Contrary to the widely accepted assumption in published literature that the channel is AWGN at a small-enough distance, our measurements indicate that values of the Rice factor do not, in general, increase monotonically as the Tx-Rx distance is reduced. A probability mixture model is presented, with distance dependent parameters, to account for the distance dependent variations of the Rice factor. A simulation model that includes small- and large-scale fading effects is presented. According to the modeling approach, a sensor node placed anywhere within the spatial extent of a small-scale region will experience the channel statistics applicable to that region.

Paper IV presents results characterizing a radio channel for outdoor short-range sensor networks. A number of antennas are placed on the ground in an open area and time-variation of the channel is induced by a person moving in the vicinity of the nodes. The channel statistics of both the LOS path and the overall narrowband signal are non-stationary. We investigate the stationarity interval length to be used for small-scale analysis. Our analysis of the various measured links shows that the Rx signal strength is significantly influenced by a moving person only when the person blocks the LOS path. We present a generic approach for modeling the LOS blockage, and also model the time-variant Doppler spectrum of the channel's scattered components.

# Preface

This doctoral thesis is comprised of two parts, the first part gives a brief introduction to the field of research and a summary of my contributions. The second part contains the included papers:

[1] S. Wyne, A. F. Molisch, P. Almers, G. Eriksson, J. Karedal and F. Tufvesson,"Outdoor-to-Indoor Office MIMO Measurements and Analysis at 5.2 GHz," in *IEEE Transactions on Vehicular Technology*, vol. 57, no. 3, pp. 1374–1386, May 2008.

[2] S. Wyne, N. Czink, J. Karedal, P. Almers, F. Tufvesson and A. F. Molisch, "A Cluster-Based Analysis of Outdoor-to-Indoor Office MIMO Measurements at 5.2 GHz," in *Proc. IEEE Vehicular Technology Conference (VTC2006-Fall)*, Montreal, Canada, vol. 1, pp. 22–26, September 2006.

[3] S. Wyne, A. Singh, F. Tufvesson, and A. F. Molisch, "A Statistical Model for Indoor Office Wireless Sensor Channels," accepted with minor revisions and resubmitted to *IEEE Transactions on Wireless Communications*, February 2009.

[4] S. Wyne, T. Santos, A. Singh, F. Tufvesson, and A. F. Molisch, "Characterization of a Time-Variant Wireless Propagation Channel for Outdoor Short-Range Sensor Networks," submitted to *IET Journal on Communications*, February 2009.

During my graduate studies, I have also contributed to the following publications, though they are not included in the thesis:

[5] J. Karedal, S. Wyne, P. Almers, F. Tufvesson and A. F. Molisch, “A Measurement-Based Statistical Model for Industrial Ultra-Wideband Channels,” in *IEEE Transactions on Wireless Communications*, vol. 6, no. 8, pp. 3028–3037, August 2007.

[6] S. Wyne, T. Santos, F. Tufvesson, and A. F. Molisch, “Channel Measurements of an Indoor office Scenario for Wireless Sensor Applications,” in *Proc. IEEE Global Telecommunications Conference (GLOBECOM)*, Washington, DC, USA, pp. 3831–3836 , November 2007.

[7] N. Czink, R. Tian, S. Wyne, G. Eriksson, T. Zemen, J. Ylitalo, F. Tufvesson, and A. F. Molisch, “Cluster Parameters for Time-variant MIMO Channel Models,” in *Proc. European Conference on Antennas and Propagation (EuCAP) 2007*, Edinburgh, UK, pp. 1–8, November 2007.

[8] N. Czink, R. Tian, S. Wyne, F. Tufvesson, J. P. Nuutinen, J. Ylitalo, E. Bonek, and A. F. Molisch, “Tracking Time-variant Cluster Parameters in MIMO Channel Measurements,” in *Proc. International Conference on Communications and Networking in China (CHINACOM)*, Shanghai, China, pp. 1147–1151, August 2007.

[9] S. Wyne, T. Santos, F. Tufvesson, and A. F. Molisch, “Measurement of Small-scale Fading for Indoor Wireless Sensor Networks,” in *Proc. URSI 2007*, Ottawa, Canada, February 2007.

[10] N. Czink, R. Tian, S. Wyne, G. Eriksson, F. Tufvesson, T. Zemen, J. P. Nuutinen, J. Ylitalo, E. Bonek, and A. F. Molisch, “Tracking Time-variant Cluster Parameters in MIMO Channel Measurements: Algorithm and Results,” in *COST2100*,TD(07)336, Duisburg, Germany, September 2007.

[11] S. Wyne, A. F. Molisch, P. Almers, G. Eriksson, J. Karedal and F. Tufvesson, “Statistical Evaluation of Outdoor-to-Indoor Office MIMO Measurements at 5.2 GHz,” in *Proc. IEEE Vehicular Technology Conference (VTC2005-Spring)*, Stockholm, Sweden, vol. 1, pp. 146–150, May–June 2005.

[12] P. Almers, S. Wyne, F. Tufvesson, and A. F. Molisch, “Effect of Random Walk Phase Noise on MIMO Measurements,” in *Proc. IEEE Vehicular Technology Conference (VTC2005-Spring)*, Stockholm, Sweden, vol. 1, pp. 141–145, May–June 2005.

[13] J. Karedal, S. Wyne, P. Almers, F. Tufvesson and A. F. Molisch, “UWB Channel Measurements in an Industrial Environment,” in *Proc. IEEE*

*Global Telecommunications Conference (GLOBECOM)*, Dallas, USA, vol. 6, pp. 3511–3516, November 2004.

[14] J. Karedal, S. Wyne, P. Almers, F. Tufvesson and A. F. Molisch, "Statistical Analysis of the UWB Channel in an Industrial Environment," in *Proc. IEEE Vehicular Technology Conference (VTC2004-Fall)*, Los Angeles, USA, vol. 1, pp. 81–85, September 2004.

[15] S. Wyne, P. Almers, G. Eriksson, J. Karedal, F. Tufvesson and A. F. Molisch, "Outdoor-to-Indoor Office MIMO Measurements at 5.2 GHz," in *Proc. IEEE Vehicular Technology Conference (VTC2004-Fall)*, Los Angeles, USA, vol. 60, pp. 101–105, September 2004.

[16] S. Wyne, P. Almers, B. K. Lau, G. Eriksson, J. Karedal, F. Tufvesson and A. F. Molisch, "Why Channel Matrix in LOS Scenarios has Zero Mean Entries," in *COST273*, TD(04)194, Duisburg, Germany, pp. 20–22 September 2004.

[17] S. Wyne, P. Almers, G. Eriksson, J. Karedal, A. Waern, B. Lundborg, F. Tufvesson and A. F. Molisch, "Outdoor to Indoor Office MIMO Measurements at 5.2 GHz," in *COST273* TD(04)152, Duisburg, Germany, 20–22 September 2004.

[18] A. F. Molisch, F. Tufvesson, P. Almers, S. Wyne, and G. Eriksson, "Statistical MIMO Propagation Channel Models - An Overview," in *Proc. IEEE European Microwave Conference (EuMC)*, Amsterdam, Netherlands, October 2004.

[19] P. Almers, O. Edfors, F. Florén, A. J Johansson, J. Karedal, B. K. Lau, A. F. Molisch, A. Stranne, F. Tufvesson and S. Wyne, "Exercises," in *Wireless Communications*, A. F. Molisch, Chichester, U.K.: Wiley, 2005.

# Acknowledgments

I am thankful to a number of people for their help and support. First, I would like to express deep gratitude to my main advisor Prof. Andreas F. Molisch for giving me the opportunity to work under his supervision. His vast knowledge of wireless communications is truly inspirational. I am grateful for his intuition in pointing to interesting new directions of research, and his allocating time for scientific discussions irrespective of his numerous commitments. I am also grateful to my co-advisor Dr. Fredrik Tufvesson, who has provided vital support in scientific matters and also in numerous administrative issues, and to Prof. Ove Edfors for acting as my second co-advisor. Thanks are due to my colleagues Dr. Johan Kåredal, Andrés Alayon, Dr. Peter Almers, Telmo Santos, and Gunnar Eriksson for countless discussions from which I have gained a lot. I would also like to thank Dr. Nicolai Czink and Amit Singh for fruitful research collaboration outside the department.

For a friendly atmosphere at work, thanks are due to present and past colleagues in the Radio systems and signal processing groups; Dr. Buon Kiong Lau, Dr. Anders J. Johansson, Peter Hammarberg, Ulrike Richter, Dr. Fredrik Florén, Dr. Kristian Solem, Frida Sandberg, Fredrik Harrysson, Dr. André Stranne, Dr. Jianjun Chen, Ruiyuan Tian, Palmi Thor Thorbergsson, Danny Smith, Farzad Foroughi, and Dr. Martin Stridh.

Thanks to Lars Hedenstjerna for always making excellent measurement fixtures, and Birgitta Holmgren, Pia Bruhn, and Doris Glock for help with administrative matters.

My PhD studies have been financed by a grant from the Swedish Science Council (Vetenskapsrådet) and an INGVAR grant of the Swedish Strategic Research Foundation (SSF).

I am eternally grateful for the support extended by my family - my parents Danyal Rashid and Nasira Parveen, whose blessings brought me this far. My wife Farah for her patience and support in all circumstances, and my daughters Anosha and Amal for being what they are.

Shurjeel Wyne

# List of Acronyms and Abbreviations

**AWGN** Additive White Gaussian Noise

**CDF** Cumulative Distribution Function

**COST** COoperation européenne dans le domaine de la recherche Scientifique et Technique

**CSI** Channel State Information

**DMC** Dense Multi-path Components

**DOA** Direction Of Arrival

**DOD** Direction Of Departure

**FFT** Fast Fourier Transform

**GSM** Global System for Mobile communications

**IEEE** Institute of Electrical and Electronics Engineers

**i.i.d.** Independent Identically Distributed

**LOS** Line-Of-Sight

**LR-WPAN** Low Rate Wireless PAN

**MCD** Multi-path Component Distance

**ML** Maximum Likelihood

**MPC** Multi-Path Component

**MIMO** Multiple-Input Multiple-Output

**PDF** Probability Density Function

**PAN** Personal Area Network

**RMS** Root Mean Square

**Rx** Receive

**SAGE** Space Alternating Generalized Expectation maximization

**SER** Symbol Error Rate

**SISO** Single-Input Single-Output

**SNR** Signal-to-Noise Ratio

**SSA** Small-Scale Area

**TDOA** Time Delay Of Arrival

**Tx** Transmit

**UCA** Uniform Circular Array

**ULA** Uniform Linear Array

**UWB** Ultra-Wideband

**WLAN** Wireless Local Area Network

**ZMCSCG** Zero-Mean Circularly-Symmetric Complex Gaussian

**3GPP** 3rd Generation Partnership Project

# Contents

# Part I

# Thesis Introduction

# Chapter 1

# Introduction

Though origins of radio communication can be traced to the experiments of O. Lodge [1] and Marconi [2], wireless communication became accessible to the masses only after introduction of cellular telephony around 1980. Since then, mobile phone technology has evolved into economically the most significant form of wireless communication, with currently over 3 billion registered users worldwide. From the humble beginnings of first-generation networks that provided voice-only service, modern day mobile networks are capable of providing reliable voice and high data-rate services such as multi-media messaging and internet access. In addition to cellular networks, e.g., Global System for Mobile Communication (GSM) [3], Wireless Local Area Networks (WLANs) [4] are in widespread use in airports, public businesses and homes. Such networks connect multiple computers or devices in a limited area, either to the internet through an access point or to each other as in an adhoc network. For coverage areas smaller than WLANs, Personal Area Networks (PANs), e.g., Bluetooth [5] and IEEE 802.15 [6], are being used. These networks can be used for a number of applications, e.g., cable replacement as in the wireless link between a computer and its peripherals. An emerging field is that of wireless sensor networks that can be used in applications ranging from security surveillance and remote health care to automated homes.

The data rates for wireless communication applications range from a few kbits/sec or lower (for sensor networks) to in excess of a few 100 Mbits/sec, refer Fig. 1.1. The demand for ever increasing data rates translates to a requirement for more bandwidth, a traditionally scarce resource in commercial wireless communication systems. This has driven research into methods for supporting increased data rates without disturbing frequency allocations of existing systems. One promising approach has been the exploitation of the spatial domain

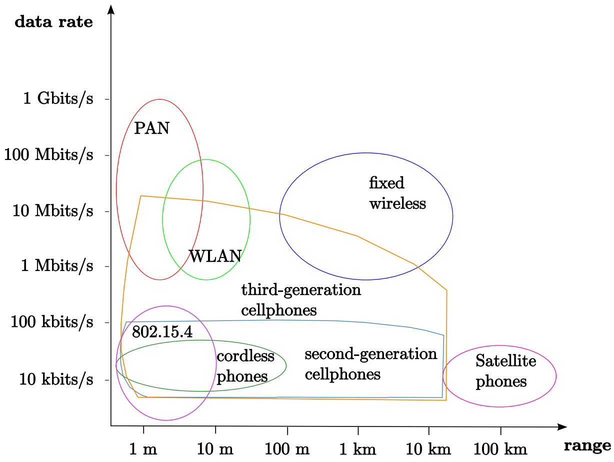

**Figure 1.1:** Data rates versus range for various applications [10].

by using multiantenna systems at both link ends, together with requisite signal processing [7], [8], [9], so called Multiple-Input Multiple-Output (MIMO) systems.[1] While the study of MIMO systems encompasses disciplines traditionally dealing with wireless communications, e.g., signal processing, communication theory, antennas etc., the investigation of the wireless propagation channel is equally important. This is the medium between the transmitter and receiver, and for MIMO systems, it determines the benefits that can be achieved with MIMO techniques. In the separate context of emerging sensor networks, investigation of the wireless channel is also of relevance because the deployment scenarios are considerably different from well-investigated cellular radio and other access point type scenarios.

This thesis deals with a measurement-based effort to characterize and model wireless channels. The included papers address some channel related issues for MIMO systems and sensor networks. The remainder of Part I is organized as follows. Chapter 2 contains an overview of some fundamentals of MIMO and sensor network systems, chapter 3 discusses wireless channel modeling in the context of the included contributions whereas chapter 4 describes principles for measuring wireless channels and the data analysis tools that are used. Finally, Chapter 5 provides a summary of the included papers and some general conclusions.

---

[1] Systems with single antenna at each end are correspondingly termed Single-Input Single-Output (SISO) systems.

# Chapter 2

# Emerging Wireless Systems

The SISO approach to transmitting with high data rates would be through an increase in size of signal constellation and/or transmission bandwidth. However, these options are not practical; due to constraints on transmit power and receive Signal-to-Noise Ratio (SNR) in the former case, and lack of bandwidth in the latter [11]. If multiple antenna elements are used at both link ends, the relative benefit with MIMO techniques is that increased data rates can be obtained without increasing transmit power or bandwidth.

In a different application sphere, wireless sensor and adhoc networks have great potential to realize home and office automation and related benefits. This chapter gives a brief overview of these two systems and their respective benefits.

## 2.1 MIMO

The concept of using multiple antennas at both ends of the radio link to boost throughput was first proposed by Winters [7], followed a few years later by the widely cited theoretical work of Foschini [8] and Telatar [9]. This has lead to tremendous research interest in MIMO over the past decade. While research continues, MIMO techniques have begun to be incorporated into wireless communication standards such as IEEE 802.11n [12] for WLAN, and 3GPP release 8 [13] for the next generation of cellular networks.

Spatial multiplexing is the enabling MIMO technique that allows potential increases in Shannon capacity. Though it has been the major source of research interest in MIMO, beamforming gain and spatial diversity are also provided by MIMO systems as a means to improve transmission quality. However, the radio channel determines which of these benefits can be exploited in a given scenario

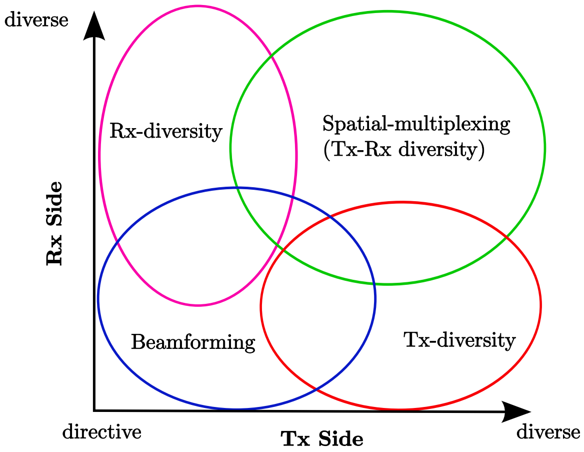

**Figure 2.1:** Inter-relation between a MIMO channel and the gains provided by MIMO techniques [14].

through signal processing, refer to Fig. 2.1. This is the motivation for MIMO channel investigations. The following sections give a brief overview of these MIMO techniques, the number of Transmit (Tx) and Receive (Rx) antenna elements is assumed to be $N_T$ and $N_R$, respectively.

### 2.1.1 Beamforming Gain

The Tx and Rx antenna patterns can be steered towards a particular angular direction by appropriate linear combination of baseband signals at the Tx and Rx elements, respectively. *Beamforming gain* is the resulting increase in average[1] SNR, relative to the average SNR at the individual elements [15], [16]. The higher the correlation of antenna signals, the higher is the beamforming gain. The maximum beamforming gain is $N_R$ when only the Rx side has channel state information (CSI), while it is $\mathrm{E}[\lambda_{max}]$ for CSI at both link ends, where $\lambda_{max}$ is the largest eigenvalue of the MIMO channel and $\mathrm{E}[\cdot]$ denotes statistical expectation operator.

### 2.1.2 Spatial Diversity

In the presence of scatterers in the environment, the signal received in a wireless channel is composed of attenuated and phase-shifted replicas of the transmitted signal arriving from different directions. The constructive or destructive

---

[1] The average is over random realizations of the wireless channel

interference of these replicas causes fluctuations in the Rx signal, termed *fading*. The fact that the Tx signal replicas come from different directions allows spatial diversity to be exploited.

Fading in a wireless channel degrades reliabilty, e.g., the average Symbol Error Rate (SER), of the communication link. Diversity techniques combat fading by increasing the probability that the Rx SNR remains above some arbitrary threshold relative to the average Rx SNR. This in turn improves the average SER relative to a system with same averge SNR but no diversity.

The diversity order[2] achieved by a MIMO system depends on the channel characteristics and the CSI available at Tx and Rx. The diversity order that can be achieved with a MIMO system decreases as the correlation of the antenna signals increases. The maximum achievable diversity order with a MIMO system is $N_R \cdot N_T$ provided that CSI is available at both Tx and Rx, and the channel is uncorrelated at both link ends. Diversity techniques in MIMO systems are not limited to spatial domain, rather those can be applied separately or jointly with diversity in, e.g., the frequency or time domain.

An in-depth analysis of diversity techniques can be found in, e.g., [17], [18]. For a discussion on coding over space and time to achieve diversity, i.e., *space-time codes*, we refer to [15], [19], [20], and references therein.

### 2.1.3 Spatial Multiplexing

Spatial multiplexing aims to transmit several *independent* data streams in parallel by exploiting the spatial dimension. The transmission of these substreams, which do not interfere at the Rx, can increase the link capacity linearly with the number of antennas. For high-data rate applications this concept is of immense practical importance given that Shannon's capacity formula predicts that capacity increases only logarithmically in SNR. Furthermore, the increased transmission rates provided by spatial multiplexing do not incur overhead in terms of bandwidth and transmit power.

In practice the channel influences the degree to which spatial multiplexing can be exploited. The number of independent data streams is upper-bounded by $\min\{N_R, N_T, N_S\}$, where $N_S$ is the number of significant scatterers. Furthermore, correlation among the entries of the channel matrix also reduces the spatial multiplexing gain relative to the un-correlated case.

For an $N_R \times N_T$ channel matrix, $\mathbf{H}$, known at Tx and Rx the channel capacity is given by [9],

$$C = \max_{\mathbf{Q}:\mathrm{Tr}\{\mathbf{Q}\}=P_T} \log_2 \det\left(\mathbf{I}_{N_R} + \frac{1}{\sigma_n^2}\mathbf{H}\mathbf{Q}\mathbf{H}^H\right), \tag{2.1}$$

---

[2] Diversity order is the slope of the average SER versus SNR curve in the high SNR regime.

where $\mathbf{I}_{N_R}$ is an identity matrix of order $N_R$, $\sigma_n^2$ is the noise power at each Rx branch. Furthermore, $\mathbf{Q} = E[\mathbf{s}\mathbf{s}^H]$ is the transmit signal covariance matrix, $\mathrm{Tr}\{\cdot\}$ is the matrix trace operator and $P_T$ is the total transmit power. The entries , $Q_{ii}$, on the main diagonal of $\mathbf{Q}$ indicate the transmit power allocated to each antenna.

When elements of the transmit signal vector, $\mathbf{s}$, are assumed to be independent Zero-Mean Circularly-Symmetric Complex Gaussian (ZMCSCG) random variables, then capacity is achieved when setting $\mathbf{Q} = \mathbf{V}\mathbf{\Lambda}\mathbf{V}^H$ where the non-zero entries of the diagonal matrix $\mathbf{\Lambda}$ give the power allocation to the Tx antennas and $\mathbf{V}$ is a unitary matrix obtained by a singular value decomposition (SVD) of the channel matrix, $\mathbf{H} = \mathbf{U}\mathbf{S}\mathbf{V}^H$. Here $\mathbf{S}$ is a diagonal matrix whose entries $\mathbf{S}_{ii}$ are the singular values of the channel.[3] The number of non-zero singular values, $\sigma_k, k = 1, \ldots, \mathrm{rank}\,(\mathbf{H})$ determines the number of independent data streams the channel can support for spatial multiplexing. Consequently, the channel capacity may be expressed as,

$$C = \sum_{k=1}^{\mathrm{rank}(\mathbf{H})} \log_2 \left(1 + \frac{\mathbf{\Lambda}_{kk}\sigma_k^2}{\sigma_n^2}\right), \tag{2.2}$$

where the $\mathbf{\Lambda}_{kk}$ are determined from the *water-filling* solution, see e.g. [21], to achieve capacity.

When channel state information is available only at Rx, the Tx side divides power equally among Tx antennas, i,e., $\mathbf{Q} = \frac{P_T}{N_T} \cdot \mathbf{I}_{N_T}$ and the capacity expression becomes [8],

$$C = \log_2 \det \left(\mathbf{I}_{N_R} + \frac{P_T}{N_T \sigma_n^2} \mathbf{H}\mathbf{H}^H\right), \tag{2.3}$$

In a random fading channel, the capacity associated with the channel is also a random variable. The analysis in such cases makes use of statistics such as *ergodic capacity* and *outage capacity*; both conventionally used to compare MIMO performance. The ergodic capacity is defined as,

$$\overline{C} = \mathrm{E}\left[\log_2 \det \left(\mathbf{I}_{N_R} + \frac{\rho}{N_T} \mathbf{H}\mathbf{H}^H\right)\right], \tag{2.4}$$

where the expectation is taken over all possible realizations of the ergodic channel.[4] Furthermore, $\rho$ is the average SNR at each Rx antenna subject to

---

[3] By definition of the SVD, $\mathbf{U}$ and $\mathbf{V}$ are both unitary, i.e., $\mathbf{U}^H = \mathbf{U}^{-1}$ and $\mathbf{V}^H = \mathbf{V}^{-1}$. Furthermore $\mathbf{V}^H$ denotes $(\mathbf{V}^*)^T$ where $\mathbf{V}^T$ denotes transpose($\mathbf{V}$) and $\mathbf{V}^*$ denotes conjugate($\mathbf{V}$).

[4] Transmit code words of arbitrary long length are assumed that experience all channel fading states.

normalizing the channel matrix as, $\frac{1}{N_R N_T}\mathrm{E}\left[\sum_{i=1}^{N_R}\sum_{j=1}^{N_T}|H_{ij}|^2\right] = 1$, i.e., the average SISO channel gain is unity. In paper I, the ergodic capacity is used to compare the performance of three analytical MIMO channel models in the outdoor-to-indoor scenario.

The $p\%$ outage capacity, $C_{\text{out},p}$, is defined as, $P\left(C \leq C_{\text{out},p}\right) = p\%$, i.e., it is the information rate achievable for $(100 - p)\,\%$ of the channel realizations [15].[5]

## 2.2 Sensor networks

A wireless sensor network is usually constituted of a number of low-cost, low-power sensor nodes, which can perform sensing, simple computation, and communication over short distances [22]. The nodes transmit the data to a nearby sink either directly or via intermediate nodes. Each sensor node essentially consists of one or more sensors, storage memory, a processor, power supply, and a radio transceiver.

Sensor networks have been traditionally associated with military applications such as battlefield surveillance and target tracking etc. However, availability of highly integrated wireless components at competitive prices has motivated interest in sensor networks for home/office networking, industrial automation and health care. In the year 2000, the ZigBee Alliance and IEEE 802 working group 15 initiated joint efforts towards development of a low-power low-cost wireless networking standard for residential and industrial environments. Work on the IEEE 802.15.4 standard was initiated the same year with the aim to define the physical (PHY) and media access control (MAC) layer specifications for a Low-Rate Wireless Personal Area Network (LR-WPAN). Some key advantages of using wireless over wired sensor networks within buildings is deployment flexibility and reduction in installation costs, i.e., new wiring does not have to be routed through conduits.

In the indoor scenario, wireless sensor networks have potential applications like security surveillance [23], inventory management [24], smart offices [25], and telemedicine sensors for advanced health care services [26]. Generally, sensor nodes communicate in one of two hierarchical structures; in a *star* topology a number of *end nodes* can only communicate with a master device termed the *coordinator*, whereas in a *peer-to-peer* (also termed *mesh*) network, all nodes can communicate with each other directly, see Fig. 2.2. The radio resources

---

[5] The theoretical concept of capacity requires transmission of infinitely long codewords. With outage capacity, the assumption is that the product of data rate and coherence time approaches infinity, so that a sufficiently long codeword can be transmitted within a coherence time of the channel.

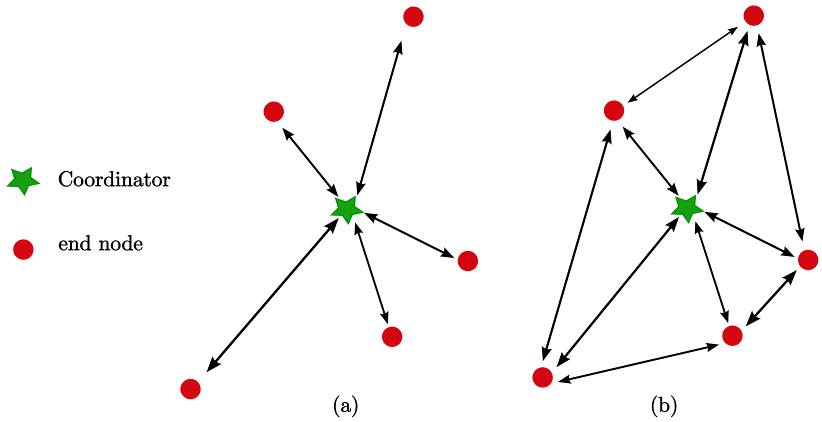

**Figure 2.2:** Network topology, (a) Star, (b) Mesh.

for such networks are often constrained, i.e., bandwidth is shared among a large number of nodes and the transmit power is usually limited. Furthermore, the network may face diverse channel conditions among its nodes. These issues can be alleviated through multihop relaying [6] or cooperative communication among the nodes, see e.g., [27], [28]. The statistics of the fading channel influence the performance of such networks. Furthermore, the placement of sensor nodes typically close to walls and floor, and *plausibly*, at office table/wall-socket heights introduce some unique channel characteristics. For example, this deployment scenario is different from the case of a mobile/laptop communicating with an access-point elevated above the *clutter* (tables, computers etc.) that can be found at and below 1 m height in an office environment. While a joint spatio-temporal analysis of the fading would be required for a complete characterization, it is still relevant to look at the spatial fading patterns in isolation, as they determine the statistics of the Rx SNR when nodes are deployed densely over a short range. This is especially relevant for deployment of sensor node clusters in relatively static channel conditions, which is the motivation for the investigations in paper III.

### 2.2.1 PHY Layer in IEEE 802.15.4

The IEEE 802.15.4 standard [29] is a widely used specification for PHY and MAC layers of commercial LR-WPANs. Taken together, the PHY and the MAC layer govern the transmission of bits over the wireless channel. The PHY layer supports Direct Sequence Spread Spectrum (DSSS) communication over two frequency bands, both located in the un-licensed Industrial/Scientific/Medical

**Table 2.1:** Some Characteristics of 802.15.4 .

| | | |
|---|---|---|
| Frequency Band | 868;915 MHz | 2.4 GHz |
| Data rate | 20 kb/s;40 kb/s | 250 kb/s |
| Modulation | BPSK | O-QPSK |
| Range | 10–20 m | |
| Channel access | CSMA-CA | |

(ISM) band. The use of DSSS communication reduces potential interference to neighbouring receivers. Furthermore, the MAC layer controls access to the wireless channel using Carrier Sense Multiple Access with Collision Avoidance (CSMA-CA) which also helps to avoid causing interference to neighbours. The DSSS transmission in combination with intended short transmission distance means that the transmit power is low, typically around 1 mW. In addition, depending on the application, some sensor nodes may conserve energy by performing the sensing operation with a low duty cycle which leads to a longer battery life-time. Some features of the PHY layer are summarized in Table 2.1 [29].

### 2.2.2 Higher layer protocols and applications

There are a number of network/application layer protocols that currently use 802.15.4. The most well known is ZigBee [30] which caters to applications dealing with home and office automation, e.g., heating and lighting controls, intrusion or motion detection etc. as well as industrial automation. Another protocol, Wireless Hart [31], is specifically geared towards industrial wireless sensor networks. Various commercial entities are now providing turn-key solutions for wireless sensor networks.

# Chapter 3

# Wireless Channel Modeling

The wireless propagation channel is the medium between the transmitter and receiver. Since the channel modifies the transmitted signal, mathematical models are needed that capture channel characteristics relevant to performance of wireless systems. These models may be deterministic, or based on stochastic theory. This chapter provides an overview of basic models, relevant to a single wireless link and to MIMO channels, in the context of the included contributions.

## 3.1 Single link aspects of Channel modeling

The transmitted signal generally reaches the receiver through different paths and may experience propagation mechanisms such as transmission, reflection, scattering, and diffraction along these paths. One of the major influences the wireless channel has on the Rx signal is an *attenuation* relative to the Tx signal. The Rx power is influenced by a deterministic attenuation factor and random fluctuations, termed *fading*. More specifically, the Rx power is influenced by a product of three factors; pathloss, large-scale fading and small-scale fading [32]. These are briefly described below.

### 3.1.1 Pathloss

Pathloss is the attenuation of the average[1] Rx power that increases with distance. Conventionally, pathloss is modeled as increasing with a power law in distance [10], [33]. Alternatively, pathloss can be expressed as an average path

---

[1] The average is over the small- and large-scale fading.

power gain, $G_{\text{avg}}(d)$, that has a power law decay in distance,

$$G_{\text{avg}}\left(d\right) = G_0 d^{-n} \tag{3.1}$$

where d is the Tx-Rx distance, $G_0 = G_{\text{avg}}\left(d\right)$ at the reference distance $d_0$ (usually assumed 1 m) and $n$ is called the *pathloss* exponent, or *propagation* exponent. The environment is characterized through the parameters $G_0$ and $n$. The parameter values are estimated from measurements by a least-squares fit of $G_{0,\text{dB}} - 10nlog\left(d\right)$ to the dB values of measured path gains over log-distance [34]. These parameters are characterized in paper III for a set of indoor sensor scenarios. The estimates are found to have a Gaussian distribution and modeled as such rather than specifying the mean values only.

### 3.1.2 Large-scale fading

Large-scale fading is defined as random variations of locally averaged Rx power, as the receiver travels a distance typically on the order of a few hundred wavelengths while maintaining approximately the same distance to transmitter [10], [35]. Fading is observed when Interacting Objects (IOs), such as buildings or terrain, block the Line-Of-Sight (LOS) or other dominant multipath components. For power samples measured along a linear trajectory of the receiver, the large-scale fading can be interpreted as the variation of small-scale averaged Rx power, about $G_{\text{avg}}(d)$. The latter concept is used in paper III to characterize the large-scale fading.

### 3.1.3 Small-scale fading

Multiple copies of the Tx signal arrive at the receiver with different attenuations and time-delay of arrival.[2] These copies are often termed *Multi-Path Components* (MPCs), and their superposition gives the Rx signal. Small-scale fading refers to random fluctuation of the Rx signal caused by an interference pattern of these MPCs. The pattern may change in space due to motion of the receiver or in time due to motion of the transmitter or scatterers. Over a small-scale region[3] the time-variant impulse response of the channel is written as [36],

$$h\left(t,\tau\right) = \sum_{l=1}^{L} \alpha_l\left(t\right)\delta\left(t-\tau_l\right), \tag{3.2}$$

---

[2] The different delays contribute to relative phase-shifts among the MPCs.

[3] Small-scale refers to the spatial extent of such a region, which is on the order of a few carrier wavelengths, $\lambda$.

where $\delta(\cdot)$ is the Dirac delta function, $L$ is the number of MPCs, and $\{\alpha_l(t)\}$ are the time-variant complex gains at the delays $\{\tau_l\}$. The time dependence of the delays is omitted because they change on a time-scale much larger than that of the complex channel gains. Since the $\{\alpha_l(t)\}$ can vary quite rapidly over the interference pattern of MPCs, they are modeled as stochastic processes.

When analyzing wireless systems, the work of Bello [37] leads to two simplifying assumptions[4] on Eq. (3.2): (i) It is assumed that the $\{\alpha_l(t)\}$ are wide-sense stationary (WSS) [37], i.e., their first and second order moments are independent of the origin of the time axis. This implies that the mean powers of the $\{\alpha_l(t)\}$ do not change with time. (ii) *Uncorrelated scattering* (US) is assumed, i.e., the $L$ paths originate from independent scatterers. The implication in this case is that the $\{\alpha_l(t)\}$ can be treated as independent stochastic processes. The above two assumptions are collectively termed wide-sense stationary uncorrelated scattering (WSSUS). The envelopes, $\{X_l(t)\} = \{|\alpha_l(t)|\}$, are of interest because they determine the Rx SNR. Different probability density functions (PDFs) are used to characterize the random fading behavior of $\{X_l(t)\}$. The Rayleigh and Rice distributions, both based on a complex Gaussian distribution of the $\{\alpha_l(t)\}$, are two of the most commonly used models. The Rayleigh is a special case of the Ricean distribution which is written as,

$$f_{X_l}(x) = \frac{x}{\sigma^2} \exp\left\{-\frac{x^2 + A^2}{2\sigma^2}\right\} I_0\left(\frac{Ax}{\sigma^2}\right), \tag{3.3}$$

where $A$ is the amplitude of the dominant MPC, $2\sigma^2$ is the power of the random components, and $I_0$ is the modified Bessel function of the first kind and zero order. The Ricean K-factor, $K = \frac{A^2}{2\sigma^2}$, is an important parameter of the Ricean distribution, as it determines the amount of fading. A value $K \longrightarrow \infty$ corresponds to no fading while $K = 0$ corresponds to a Rayleigh fading distribution.[5]

From a system design aspect, the type of envelope fading distribution is important because it determines the fading margin [10] required to achieve coverage with a certain outage probability. At large $K$, a Ricean fading channel exhibits minimal fading and approximates an AWGN channel. This concept has implications for clustering of sensor nodes in that an AWGN channel between the nodes in a cluster is often assumed in theoretical analysis. In paper III the assumption of an AWGN channel at gradually decreasing Tx-Rx separation is tested, and it is observed that K-factors have a non-monotonic behavior with decreasing distance, so that the AWGN assumption is not necessarily valid at

---

[4] Ultra-Wideband systems are an exception to this rule, and are not covered in this thesis.

[5] A Rayleigh envelope implies a zero-mean for the underlying complex Gaussian distribution.

small Tx-Rx distances. A related issue, in the context of wireless transmission, is the definition of the Ricean $K$ factor. In paper I, a distinction is made between the LOS power factor and the Ricean K-factor, valid for the case of high resolution parameter estimates.

### 3.1.4 Narrowband and Wideband channels

In modeling wireless channels, a distinction is made between *narrowband* and *wideband* channels that is based on the inter-relation between transmission bandwidth and the coherence bandwidth [10] of the wireless channel. A wireless communication link experiences a narrowband channel if the transmission bandwidth is less than the coherence bandwidth of the channel. In this case the receiver will not be able to resolve the various MPCs, i.e., in the context of Eq. (3.2), the receiver observes $L = 1$. For narrowband systems, the frequency response of the channel is invariant over the transmission bandwidth, hence the term *frequency flat* flading for such channels. For the converse case, i.e., transmission bandwidth larger than coherence bandwidth, the channel is termed *wideband* and the system is able to resolve the MPCs based on their Time-Delay-of-Arrival (TDOA). For such communication systems, the frequency response of the channel varies over the transmission bandwidth, hence the term *frequency-selective* fading for such channels. For the measurements discussed in this thesis, a wideband channel sounding equipment was used to record the complex channel frequency response. When performing a narrowband analysis of the measured data, the channel samples at different tones are considered as random realizations of the narrowband channel, though sometimes correlated.

### 3.1.5 WSSUS considerations

In a statistical analysis of wireless channels, the WSSUS assumption is invariably used. In practice, the spatial structure of the channel, i.e., the number, strength, and direction of arrival of the MPCs change considerably over time and/or space, so that stationarity intervals need to be determined. For outdoor mobile scenarios a stationarity region on the order of $10\lambda$ has been used conventionally [10], though for indoor scenarios, the size of the spatial stationarity region can be considerably smaller.

For the indoor measurements in paper III, stationarity is estimated based on variations of the small-scale averaged power. A fixed length of the small-scale stationary region is defined by the consideration to maintain the running average of Rx power below 5 dB over the chosen window length. A window length of $5\lambda$ is determined to be a reasonable choice for the small-scale analysis. For the outdoor fixed node measurements in paper IV, temporal stationarity intervals are estimated by thresholding the correlation between average power delay profiles [38].

A survey of the open literature reveals that there are no universally accepted criteria to determine stationarity intervals within measurements, and this is a topic of ongoing research, see e.g., [39], [40], [38] and references therein.

## 3.2 Aspects of MIMO channel modeling

As discussed in chapter 2, the MIMO channel influences the type of gains achievable by MIMO techniques. Therefore, accurate models of the MIMO channel are needed both for network planning and for system simulation to design and compare MIMO algorithms. While a model should capture channel propagation effects, significantly influencing system design, channel models are also desired to be simple to use. This inherent trade-off has been one of the motivating factors for research in the field of MIMO channel modeling, and a number of MIMO channel models have been proposed over the years. A comprehensive and systematic survey of MIMO channel models can be found in [41], [10]. This section briefly reviews these concepts with an aim to provide context to the included contributions.

We start with the MIMO channel matrix that essentially provides an input-output relation between the Tx and Rx signal vectors. A schematic illustration of a MIMO system is shown in Fig. 3.1. The multiple antennas at Tx and Rx sides require that the MIMO channel is specified for all Tx and Rx antenna pairs. This means that for an $N_R \times N_T$ MIMO system, the general case of a time-variant wideband channel is represented by an $N_R \times N_T$ channel matrix,

$$\mathbf{H}(t,\tau) = \begin{bmatrix} h_{11}(t,\tau) & h_{12}(t,\tau) & \cdots & h_{1N_T}(t,\tau) \\ h_{21}(t,\tau) & h_{22}(t,\tau) & \cdots & h_{2N_T}(t,\tau) \\ \cdots & \cdots & \ddots & \cdots \\ h_{N_R 1}(t,\tau) & h_{N_R 2}(t,\tau) & \cdots & h_{N_R N_T}(t,\tau) \end{bmatrix}, \tag{3.4}$$

where $h_{i,j}(t,\tau) \in \mathbb{C}$ represents the time-variant impulse response between the $j$-th Tx and $i$-th Rx antenna, $t$ is the absolute time and $\tau$ is the TDOA.

Assuming that a signal $s_j(t) \in \mathbb{C}$ is transmitted from the $j$-th Tx element, the signal received at the $i$-th Rx element is written as,

$$r_i(t) = \sum_{j=1}^{N_T} h_{i,j}(t,\tau) * s_j(t) + n_i(t), \tag{3.5}$$

where $*$ denotes the convolution operation and $n_i$ is the additive ZMCSCG noise at the $i$-th Rx element. When the channel is time-invariant, the time-

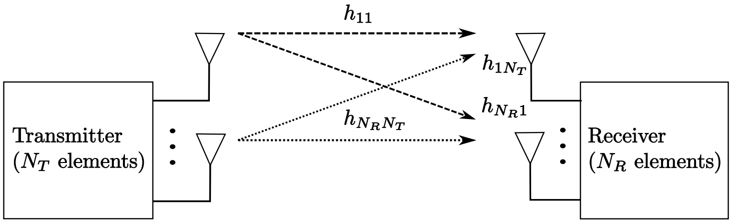

**Figure 3.1:** An $N_R \times N_T$ MIMO system showing channel gains for individual links.

dependence can be disregarded so that $\mathbf{H}(t,\tau) = \mathbf{H}(\tau)$. Furthermore, if the channel is frequency-flat fading, it has only a single tap so that $\mathbf{H}(\tau) = \mathbf{H}$. Under these assumptions the MIMO system equation corresponding to Eq. (3.5) reduces to,

$$\mathbf{r}(t) = \mathbf{H}\mathbf{s}(t) + \mathbf{n}(t), \tag{3.6}$$

where $\mathbf{r}(t) = [r_1(t) \ldots r_{N_R}(t)]^T$, $\mathbf{s}(t) = [s_1(t) \ldots s_{N_T}(t)]^T$, and for the noise, $\mathbf{n}(t) = [n_1(t) \ldots n_{N_R}(t)]^T$.

The channel matrix in Eqs. (3.5) and (3.6) does not capture the propagation effects only; other additional effects such as the influence of the Tx and Rx antennas are also included. These considerations have lead to a fundamental classification of MIMO channel models into two categories; *physical models* and *analytical models* [41], [10].

### 3.2.1 Physical Models

Physical models are independent of antenna configuration.[6] Such models are based on characterizing the electromagnetic waves propagating between the Tx and Rx stations. In most models the waves are assumed to have a plane wave front, i.e., a *plane wave assumption* is used and the waves are represented by rays. These rays and the MPCs described earlier have a one to one correspondence, so that the two terms can be used interchangeably.

One approach to describe the propagation environment is in terms of MPC parameters such as attenuation, phase, TDOA, direction of departure (DOD) at the Tx, and direction of arrival (DOA) at the Rx. An alternative approach for the propagation description, is in terms of locations of the actual physical processes such as reflection and diffraction. The following paragraphs provide a short overview of the different approaches.

---

[6] The antenna configuration is described, in general, by antenna pattern, number of elements, array geometry, polarization, and mutual coupling [41].

### Deterministic physical models

A deterministic way to model the propagation channel is through the channel's double-directional impulse response [42], [43],

$$h\left(\mathbf{r}_{\mathrm{Tx}}, \mathbf{r}_{\mathrm{Rx}}, \tau, \phi, \psi\right) = \sum_{l=1}^{L} h_l\left(\mathbf{r}_{\mathrm{Tx}}, \mathbf{r}_{\mathrm{Rx}}, \tau, \phi, \psi\right), \tag{3.7}$$

where $\mathbf{r}_{\mathrm{Tx}}$ and $\mathbf{r}_{\mathrm{Rx}}$ denote position of the transmitter and receiver, respectively. The variables $\tau$,$\phi$, and $\psi$ represent TDOA, DOD, and DOA, respectively. Furthermore $L$ is the total number of MPCs. The $h_l\left(\mathbf{r}_{\mathrm{Tx}}, \mathbf{r}_{\mathrm{Rx}}, \tau, \phi, \psi\right)$ is the contribution of the $l$-th wave and given by,

$$h_l\left(\mathbf{r}_{\mathrm{Tx}}, \mathbf{r}_{\mathrm{Rx}}, \tau, \phi, \psi\right) = a_l \delta\left(\tau - \tau_l\right) \delta\left(\phi - \phi_l\right) \delta\left(\psi - \psi_l\right), \tag{3.8}$$

where $a_l$,$\tau_l$,$\phi_l$, and $\psi_l$, denote complex amplitude, TDOA, DOD, and DOA, respectively, of the $l$-th MPC. In a time variant channel, these individual MPC parameters, as well as the number of MPCs, $L$ may become functions of time. For a more general description antenna polarization can also be taken in to account [42], [43].

The double-directional modeling effort requires MIMO measurements in representative scenarios, followed by a determination of the MPC parameters with high-resolution algorithms, e.g., [44], [45]. The scattering geometry can then be re-generated from signal processing methods, e.g., [46]. Finally, new channel realizations can be generated by moving the Tx and/or Rx along trajectories other than the ones used in measurements [47], [48].

Other deterministic approaches to channel modeling are *Ray tracing* [49] and/or *Ray launching* [50]. These are especially useful for site-specific channel modeling, e.g., when a geographical database of significant scatterers in an urban environment is available and optimum placement of a base-station antenna is desired.

### Geometry-based stochastic channel models

In a geometry-based stochastic channel model (GSCM) the location of the scatterers is specified in a stochastic manner according to suitable probability distributions. Subsequently ray tracing is performed to obtain the channel impulse response. The concept of multipath clusters is used in most variants of this approach. The GSCM approach is suitable for modeling time-variant channels; parameters of the MPCs are adjusted automatically with movement of terminals or scatterers so that the correct fading correlation is generated. Furthermore, large-scale fading effects are also incorporated, see e.g. [51].

**Non-geometric stochastic channel models**

These models assign values to the physical parameters of the MPCs, i.e., TDOA, DOD, DOA etc. using stochastic probability distribution functions. The geometry of the physical environment is not considered, see, e.g. [52].

### 3.2.2 Analytical models

Analytical models mathematically describe a narrowband MIMO channel matrix, without going into details of the wave propagation.[7] The influence of antennas is included in the model so that the models are applicable to the MIMO system under consideration. The parameters of these models are usually extracted from MIMO measurements.

Analytical channel models assume that the entries of the MIMO channel matrix are drawn from a ZMCSCG distribution with the possible addition of a dominant (deterministic) component. For the latter case of Ricean fading, the $N_R \times N_T$ channel matrix, $\mathbf{H}$, is written as [53],

$$\mathbf{H} = \sqrt{\kappa}\mathbf{H}_{\mathrm{d}} + \sqrt{1-\kappa}\mathbf{H}_{\mathrm{Res}}, \tag{3.9}$$

where $\kappa = \frac{K}{1+K}$, $K$ is the Ricean $K$-factor, $\mathbf{H}_{\mathrm{d}}$ represents the LOS or other dominant contributions, and $\mathbf{H}_{\mathrm{Res}}$ is the zero-mean residue (stochastic) part of $\mathbf{H}$, that the analytical models aim to represent. This is also the approach used in paper I to test the performance of some of these analytical models in an outdoor-to-indoor Ricean fading environment.

Analytical models can be classified as correlation-based or propagation-based models. In the following paragraphs we describe these classifications. Furthermore, for ease of exposition we set $K = 0$ in Eq. (3.9) so that $\mathbf{H} = \mathbf{H}_{\mathrm{Res}}$.

**Correlation-based analytical models**

The underlying principle of this modeling approach is that the spatial structure of the channel can be modeled by the spatial correlation of the channel matrix entries. MIMO channel matrices with correlated elements can be generated by correlating Independent Identically Distributed (i.i.d.) Gaussians. When the *full correlation matrix*, $\mathbf{R}$, is estimated from measurements on $\mathbf{H}$, the procedure

---

[7] An extension to wideband channel modeling is possible by applying the analytical model to each tap.

is,

$$\begin{aligned} \mathbf{h} &= \mathrm{vec}\left\{\mathbf{H}\right\}, \\ \mathbf{R} &= E\left[\mathbf{h}\mathbf{h}^H\right], \\ \mathbf{H}_{\text{full-corr}} &= \text{un-vec}\left\{\mathbf{R}^{1/2}\mathbf{g}\right\}. \end{aligned} \tag{3.10}$$

where the operator $\mathrm{vec}\left\{\mathbf{A}\right\}$ stacks the columns of its matrix argument, $\mathbf{A}$, on top of each other, and un-vec$\left\{\cdot\right\}$ is the inverse operation. Furthermore, $\mathbf{A}^{\frac{1}{2}}$ denotes matrix square-root defined such that $\mathbf{A}^{\frac{1}{2}}\left(\mathbf{A}^{\frac{1}{2}}\right)^H = \mathbf{A}$, and $\mathbf{g}$ is an $N_R N_T \times 1$ random vector with elements which are i.i.d. ZMCSCG random variables with unit variance.

The analytical model with $\mathbf{R}$ a scaled identity matrix is popularly termed the *i.i.d model*. This corresponds to all entries of the Gaussian channel matrix, $\mathbf{H}$, being independent of each other. The physical interpretation is that MPCs are uniformly distributed in all directions, referred to as a *rich-scattering* environment in the literature, and the antenna elements are spaced apart by at least half the carrier wavelength.

For large array sizes, the manipulation of a size $N_R N_T \times N_R N_T$ full correlation matrix, $\mathbf{R}$, becomes cumbersome. This has lead to some correlation based models that approximate $\mathbf{R}$ with certain assumptions. Here we discuss two such models, the *Kronecker* and the *Weichselberger model* that are used in analyzing the outdoor-to-indoor scenario in paper I.

### Kronecker model

The Kronecker model [54] approximates $\mathbf{R}$ by a Kronecker product of the antenna correlation matrices,

$$\mathbf{R} = \mathbf{R}_{\mathrm{Tx}} \otimes \mathbf{R}_{\mathrm{Rx}}, \tag{3.11}$$

where $\mathbf{R}_{\mathrm{Tx}} = E\left[\mathbf{H}^H\mathbf{H}\right]$ and $\mathbf{R}_{\mathrm{Rx}} = E\left[\mathbf{H}\mathbf{H}^H\right]$ are the antenna spatial correlation matrices at the Tx and Rx side, respectively, and $\otimes$ denotes the Kronecker matrix product. Equivalently, the MIMO channel matrix is modeled as,

$$\mathbf{H}_{\mathrm{Kronecker}} = \frac{1}{\sqrt{tr\left\{\mathbf{R}_{\mathrm{Rx}}\right\}}}\mathbf{R}_{\mathrm{Rx}}^{\frac{1}{2}}\mathbf{G}\mathbf{R}_{\mathrm{Tx}}^{\frac{T}{2}}. \tag{3.12}$$

Here $\mathbf{G} = \text{un-vec}\left\{\mathbf{g}\right\}$ is a random i.i.d. Gaussian matrix. The Kronecker model has been used extensively in published work due to its simplicity, ability to fit some measurement scenarios, and a smaller number of required parameters compared to the full correlation model. However, the Kronecker model makes the joint DOA-DOD spectrum to be an outer product of the marginal spectra, such that an MPC with a unique combination of DOA and DOD cannot be modeled. In other words, the Kronecker model assumes that the Rx side correlation matrix is independent of which direction the Tx side sends the signal. In [55] it was suggested that the Kronecker model, in general, underestimates the channel capacity. In paper I this result is validated for the outdoor-to-indoor scenario.

### Weichselberger model

The Weichselberger model [55] allows for joint modeling of the Tx and Rx side correlations, by introducing a power coupling matrix, $\Omega$, that governs the average power coupled between the $N_T$ eigenvectors of the Tx side correlation matrix and the $N_R$ eigenvectors of the Rx side correlation matrix. The eigenbasis of the antenna correlation matrix at each link end remains independent of the transmit direction from the other end.[8] Realizations of the channel matrix are generated as,

$$\mathbf{H}_{\text{weichsel}} = \mathbf{U}_{\text{Rx}} \left( \tilde{\boldsymbol{\Omega}} \odot \mathbf{G} \right) \mathbf{U}_{\text{Tx}}^{T}, \tag{3.13}$$

where $\mathbf{U}_{\text{Rx}}$ and $\mathbf{U}_{\text{Tx}}$ are Rx and Tx side eigenbasis of respective antenna correlation matrix,

$$\begin{aligned} \mathbf{R}_{\text{Tx}} &= \mathbf{U}_{\text{Tx}} \Lambda_{Tx} \mathbf{U}_{\text{Tx}}^{T}, \\ \mathbf{R}_{\text{Rx}} &= \mathbf{U}_{\text{Rx}} \Lambda_{Rx} \mathbf{U}_{\text{Rx}}^{T}, \end{aligned} \tag{3.14}$$

and $\Lambda_{\text{Tx}}$ and $\Lambda_{\text{Rx}}$ are diagonal matrices of eigenvalues at respective link end.

### Propagation based models

In this approach the channel matrix is modeled through propagation parameters. We discuss here only the virtual channel representation (VCR) model introduced in [56] for uniform linear arrays at each link end.

The virtual channel representation (VCR) was introduced in [56] assuming a Uniform Linear Array (ULA) at each link end, and allows arbitrary power coupling between pre-determined directions at the Tx and Rx sides. The model uses discrete Fourier transform matrices $\mathbf{A}_{\text{Rx}}$ and $\mathbf{A}_{\text{Tx}}$ at respective link ends, to sample the spatial characteristics of the channel. Realizations of the channel model can be generated as,

$$\mathbf{H}_{\text{VCR}} = \mathbf{A}_{\text{Rx}} \left( \tilde{\boldsymbol{\Omega}} \odot \mathbf{G} \right) \mathbf{A}_{\text{Tx}}^{T}. \tag{3.15}$$

---

[8] The Kronecker model is included as a special case with a rank one coupling matrix [55].

The columns of $\mathbf{A}_{\mathrm{Rx}}$ and $\mathbf{A}_{\mathrm{Tx}}$are based on the array response (steering) vectors computed at fixed virtual directions, and the matrix $\tilde{\mathbf{\Omega}}$ is the element-wise square root of the power coupling matrix $\mathbf{\Omega}$; the entry $\mathbf{\Omega}_{ij}$ gives the average power coupled between the $i$-th receive and $j$-th transmit direction.

In our measurement setup, the Rx array was not a ULA, but rather a Uniform Circular Array (UCA) with an absorber in the center. We thus use a generalization of Eq. (3.15) that combines the standard (virtual channel model) at the Tx side, with a *canonical* representation, based on the channel statistics, at the Rx side

$$\mathbf{H}_{\mathrm{VCR}} = \hat{\mathbf{U}}_{\mathrm{Rx}} \left( \tilde{\mathbf{\Omega}} \odot \mathbf{G} \right) \mathbf{A}_{\mathrm{Tx}}^{T}, \tag{3.16}$$

where $\hat{\mathbf{U}}_{\mathrm{Rx}}$ is an estimate of the receive eigenvector matrix obtained by eigenvalue decomposition of $\hat{\mathbf{R}}_{\mathrm{Rx}}$.

In addition to the above described classifications, there exist comprehensive standardized models, e.g., the 3GPP spatial channel model (SCM) [57], and the COST 273 model [58]. We refer to [41] for a comparative study of these and other models.

# Chapter 4

# Channel Measurements

Research in the field of channel modeling would not be possible without channel measurements. While stochastic channel models need to be parametrized from extensive measurements, performance of deterministic models needs to be verified by actual measurements.

The measurements reported in this thesis were performed with the RUSK Lund channel sounder [59], for papers III and IV, and the RUSK ATM sounder for papers I and II. A brief review of measurement principles is given below, followed by specifications of the channel sounders that were used. This chapter concludes with a brief introduction to data analysis tools, high resolution algorithms, and a clustering procedure that were used in the included papers.

## 4.1 Measurement Principles

A *channel sounder* is an equipment that can measure the wireless channel's complex baseband impulse reponse or equivalent frequency transfer function, over the system bandwidth of the sounder. A transmit signal known to the receiver is transmitted through the channel and recorded at the equipment's receiver. In order to measure phase information, either a common frequency reference is employed at Tx and Rx, or separate references, if used, are phase-locked prior to the measurements. Wideband measurements allow a characterization of the delay dispersion, or equivalently the frequency selectivity, exhibited by the channel. Furthermore, sampling the spatial domain with appropriate antenna arrays at both link ends allows to measure the double-directional properties of the wireless channel.

For MIMO measurements the transfer functions or impulse responses for all combinations of Tx and Rx elements need to be measured. A common hardware configuration is the *switched antenna array*, i.e., a fast RF multiplexer (switch) is used to sequentially connect antenna elements to a common RF electronics chain at Tx and Rx side. This approach saves cost and calibration effort inherent with multiple chains and allows flexibility to use different array sizes. The synchronized switching of the Tx and Rx elements allows the channel sounder to keep track of which Tx-Rx combination is measured at any given time. The switching times are synchronized to the period of the sounding signal, $T_p$. For each Rx switching, and optionally for Tx switching, a *guard period* is used to avoid switching transients in the measurements. A conventional measurement timing diagram is shown in Fig. 4.1, but other arrangements are also possible.

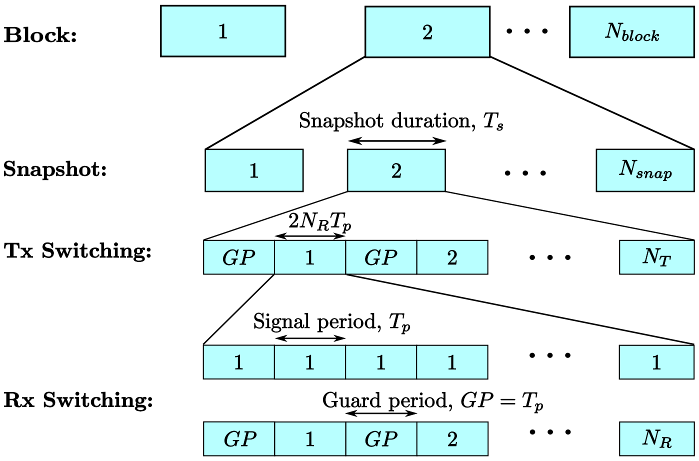

**Figure 4.1:** MIMO measurement timing diagram. The snapshot duration is, $T_s = N_T\left(2N_R + 1\right)T_p$.

A *MIMO snapshot* is defined by one complete cycle of measurements of the channel transfer functions for all Tx-Rx combinations, refer Fig. 4.1. It is assumed that the channel does not change during the snapshot duration, $T_s$. Therefore, when a time-variant wireless channel is to be measured, $T_s$ is upper bounded by the Nyquist sampling criteria,

$$T_s \leq \frac{1}{2f_{\mathrm{D,\ max}}}, \tag{4.1}$$

where $f_{\mathrm{D,\ max}}$ is the maximum Doppler shift induced by the channel. When this in-equality is satisfied, channel variations during a MIMO snapshot can

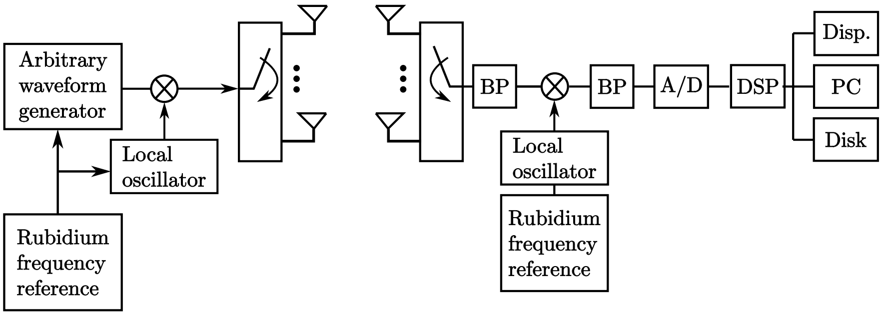

**Figure 4.2:** Block diagram of RUSK Lund channel sounder [59].

be disregarded, i.e., a *quasi-static* channel is assumed. It should be noted, however, that by re-arranging the measurement timing diagram it is possible to measure larger Doppler shifts for a given snapshot duration [60].

## 4.2 RUSK Lund Channel Sounder

The RUSK Lund channel sounder is based on a sounding principle known as *frequency domain correlation processing* [61]. At the Tx side, the channel sounder excites all frequencies within its bandwidth simultaneously to allow fast measurement speed. This is done by designing a periodic multifrequency signal with identically powered spectral lines. The phases of these spectral lines (sub-carriers) are fixed to optimize on a minimum peak-to-average ratio, i.e., *crest factor*, of the sounding signal which allows the Tx amplifier to be used efficiently. The time duration of the sounding signal, $T_p$, is set to a value larger than the maximum excess delay, $\tau_{max}$, expected in the measured channel. The time duration of the signal determines the spacing of the spectral lines, $f_\Delta = \frac{1}{T_p}$, and hence the number of spectral lines within the measurement bandwidth. The sounding signal is designed in the frequency domain, converted to a time domain signal and stored in the arbitrary waveform generator from where it is continously transmitted as a periodic signal.

A block diagram of the sounder is shown in Fig. 4.2. At the Rx side, the signal is filtered and down-converted, demodulated and then sampled at 640 MHz. The sampled signal is Fourier transformed to the frequency domain in the DSP block shown in Fig. 4.2. The time variant channel transfer function, $H\left(t,k\right)$, is then estimated from a correlation,

$$H\left(t,k\right) = \frac{Y\left(k\right) X^*\left(k\right)}{X\left(k\right) X^*\left(k\right)} = \frac{Y\left(k\right)}{X\left(k\right)}, \tag{4.2}$$

**Table 4.1:** Measurement parameters of RUSK Lund and RUSK ATM sounder that were used in the campaigns.

| Parameter | RUSK Lund | RUSK ATM |
|---|---|---|
| Center Frequency [GHz] | 2.6 | 5.2 |
| Bandwidth [MHz] | 200 | 120 |
| Test signal length [$\mu$s] | 1.6 | 1.6 |
| Tx power [dBm] | 27 | 33 |

where $Y(k)$ is the Discrete Fourier Transform (DFT) of the signal received through the measured wireless channel, and $X(k)$ is the DFT of the received signal measured during the system calibration, whereby a cable connects Tx and Rx unit.[1] This compensates for the frequency response of the channel sounder hardware from measurement data.

In papers I and II, the RUSK ATM channel sounder was used for measurements. Though the working principles are the same as those described for RUSK Lund, the salient differences relevant to the measurements are provided in Table 4.1.

## 4.3 Data Analysis

### 4.3.1 Parameter Estimation Algorithms

For the double-directional characterization of MIMO channels, it is required to estimate the propagation parameters, TDOA ($\tau$), azimuth and elevation DOD ($\phi_{\text{DOD}}, \theta_{\text{DOD}}$), azimuth and elevation DOA ($\phi_{\text{DOA}}, \theta_{\text{DOA}}$), Doppler and complex path-weight of the waves impinging at the Rx. This task is performed by various channel parameter estimation algorithms. Though sub-space based methods such as ESPRIT [62] were originally used for this purpose, these methods require symmetric array structures and assume identical response of individual antenna elements.

The above-mentioned restrictions have motivated research into *maximum-likelihood* (ML) based methods and their subsequent use in the channel measurement community. ML methods are based on the assumption that the Rx signal is a superposition of planar wave fronts (scatterers assumed to be in far-field of the Tx and Rx antennas). A signal model for the measured channel is pre-assumed and is based on parameters of the MPCs that are to be estimated. Furthermore, the signal model also incorporates the complex gain (magnitude

---

[1] The calibration is a necessary step before actual measurements.

and phase) patterns of the antennas used for the measurements. In this way the channel can be characterized independent of the antenna configuration that was used for measurements.

One of the most widely used of the ML methods is the Space Alternating Generalized Expectation maximization (SAGE) algorithm [44]. The SAGE assumes a finite number, $L$ of *specular* plane waves impinging at the Rx location, and the signal model is based on parameters of the $L$ MPCs. The ML estimator of the parameter vector is found by iteratively maximizing the likelihood function of the signal model under the assumption of i.i.d. Gaussian additive noise. The SAGE avoids the complex multi-dimensional optimization, over all parameters of $L$ MPCs, by sequentially estimating parameters of individual MPCs in each iteration. Furthermore, the parameters of the individual MPCs are themselves estimated in subsets, sequentially, to reduce the complexity further. For a rigorous explanation of SAGE, refer to [44]. The SAGE is used for parameter extraction in paper I, where a signal model for the channel transfer function is also provided.

The RIMAX algorithm [45] is another ML based algorithm, which estimates *specular* components jointly with the *dense multipath components* (DMC) of the channel. The DMC is an aggregate description of components, e.g., due to diffuse reflections, that cannot be assigned to specific DOAs, DODs, or TDOA etc. The effect of DMC can be observed, e.g., in a measured power delay profile - it is the exponentially decaying residue that remains after the contribution of specular components has been estimated and removed. In [45] a parametric modeling approach for the DMC is provided with reference to the measured power delay profile. The RIMAX additionally estimates the reliability of parameter estimates, MPCs that fail some pre-defined reliability threshold are dropped from consideration. This means that the number of paths finally estimated from a MIMO snapshot can be less than the source order (number of MPCs) assumed when beginning the estimation process for that snapshot. In paper II the RIMAX is used for parameter extraction. A commercial implementation of the RIMAX by MEDAV [59] is used for this purpose.

Some related issues are well-known open research topics, e.g., using the measured data to estimate the unknown source order is still under investigation. Additionally, the plane wave assumption is less than accurate in some scenarios, e.g., indoors where reflecting surfaces may not be in the far-field of the antennas. Therefore signal models may need to incorporate spherical waves to deal with such cases. Furthermore, in a recent investigation [63], the authors have performed tests in an anechoic chamber to study effects of incomplete antenna data models on parameter extraction results. A *complete* data model in this context was defined as (i) the antenna response characterized in

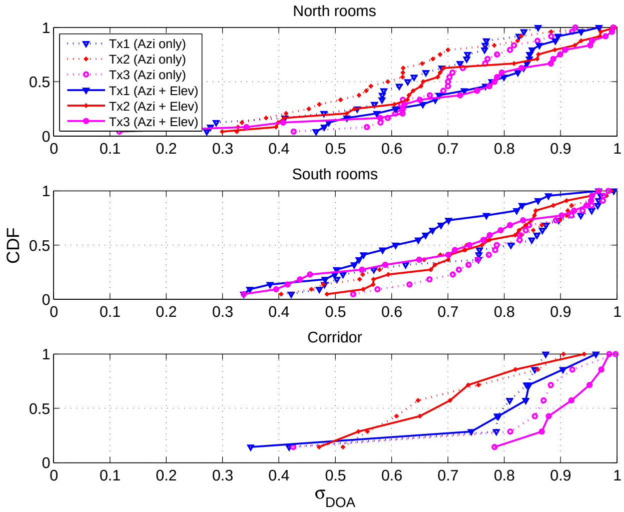

**Figure 4.3:** Influence of including elevation, on the RMS spread of azimuth component of DOA.

both azimuth and elevation over the full sphere (2D-pattern), and (ii) each antenna port response characterized for both vertical and horizontal polarization states of the excitation field. The authors conclude that channel parameters estimated with incomplete antenna data models result in artificially large angle spreads.

The parameter extraction procedure in paper I makes use of only the azimuth antenna pattern (1D) for the UCA used at the Rx side. Extending the antenna data to also include elevation information, however, does not provide any conclusive relation between the DOA spreads (in azimuth only) estimated with the two antenna data models, see Fig. 4.3.[2] It should be noted though, that there are some open issues in the presented analysis, e.g., both the 1D and 2D patterns had been measured with verticaly polarized excitation only. Therefore, our most recent antenna data may not be *complete* in the sense of [63]. Additional plots of DOD and delay spread from the same analysis are provided in Figs. 4.4 and 4.5, respectively.

---

[2] The parameter extraction is performed with RIMAX using a maximum source order of 100 MPCs. This value is selected to minimize any potential influence of source order effects on the comparison.

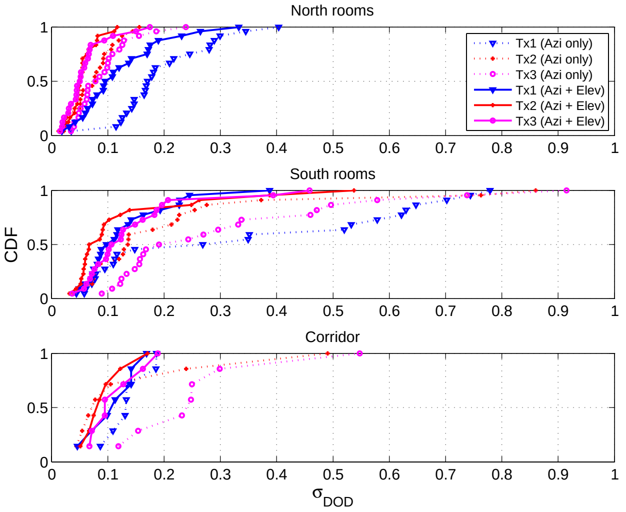

**Figure 4.4:** RMS spread of azimuth component of DOD.

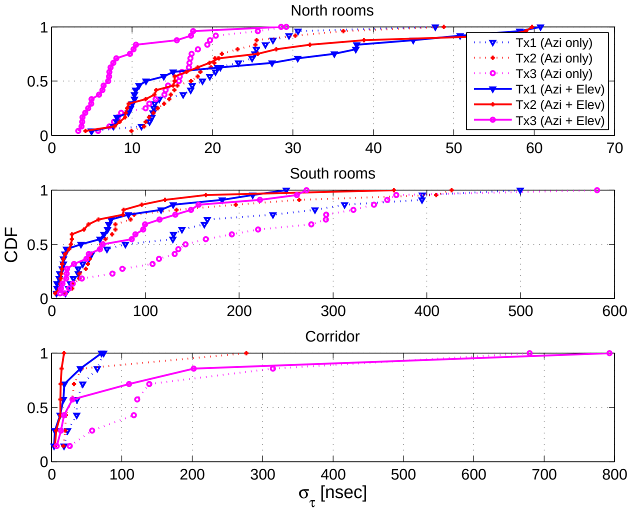

**Figure 4.5:** RMS spread of TDOA.

### 4.3.2 Clustering Algorithm

Traditionally MPC clusters have been visually identified from measurement results, see e.g., [64], [65]. This method becomes cumbersome for the large volume of multi-dimensional data generated by processing MIMO measurements. Furthermore, the results of visual clustering may be subject to individual interpretation. These reasons have motivated research into automating the clustering procedure, see e.g., [66] and references therein.

Paper II presents a statistical analysis of MPC clusters. The MPC parameters were extracted by applying the high-resolution channel parameter estimation algorithm RIMAX [45] to MIMO measurements. Identification of MPC clusters was carried out by an automatic clustering approach presented in [67]. Since a general description of the clustering algorithm could not be included in paper II due to space constraints, a brief summary based on the descriptions in [67], [66] is provided below.

The clustering of MPCs is performed in the parameter space, i.e., TDOA ($\tau$), azimuth and elevation DOD ($\phi_{\mathrm{DOD}}, \theta_{\mathrm{DOD}}$), and azimuth and elevation DOA ($\phi_{\mathrm{DOA}}, \theta_{\mathrm{DOA}}$) of the MPCs are jointly considered when identifying clusters. To enable joint use of parameters with different units, the *multipath component distance* (MCD) metric [68] is used as a distance measure between two MPCs in parameter space. The MCD between the $i$-th and $j$-th MPCs for DOD and DOA is written as,

$$MCD_{\mathrm{DOD/DOA},ij} = \frac{1}{2}\left| \begin{pmatrix} \sin(\theta_i)\cos(\phi_i) \\ \sin(\theta_i)\sin(\phi_i) \\ \cos(\theta_i) \end{pmatrix} - \begin{pmatrix} \sin(\theta_j)\cos(\phi_j) \\ \sin(\theta_j)\sin(\phi_j) \\ \cos(\theta_j) \end{pmatrix} \right|. \quad (4.3)$$

The scaling of $\frac{1}{2}$ normalizes the maximum distance to 1. The TDOA distance is,

$$MCD_{\tau,ij} = \varsigma \cdot \frac{|\tau_i - \tau_j|}{\Delta\tau_{\max}} \cdot \frac{\tau_{\mathrm{std}}}{\Delta\tau_{\max}}, \quad (4.4)$$

where $\Delta\tau_{\max} = \max_{i,j}\{|\tau_i - \tau_j|\}$, $\tau_{\mathrm{std}}$ is the RMS delay spread, and $\varsigma$ is a scale factor to give delays more importance. The joint distance measure then becomes,

$$MCD_{ij} = \sqrt{\|MCD_{\mathrm{DOD},ij}\|^2 + \|MCD_{\mathrm{DOA},ij}\|^2 + MCD_{\tau,ij}^2}. \quad (4.5)$$

MPCs extracted from one MIMO snapshot are analyzed for clustering. The identification of clusters is done by a modified K-means algorithm [69] which additionally considers MPC powers in the clustering process. The modified algorithm, termed *KPowerMeans*, identifies clusters by their centroids and these are iteratively moved through parameter space to minimize the sum of the power-weighted MCD between each MPC and its associated cluster centroid given by

$$D = \sum_{l=1}^{L} P_l \cdot MCD\left(\mathbf{x}_l, \mu_{I_l^{(i)}}\right), \tag{4.6}$$

where $L$ is the number of extracted MPCs, and for the $l$-th MPC $P_l, l = 1, \ldots, L$ is the power and $\mathbf{x}_l$ is the parameter vector used in the MCD. Furthermore, $\mu_{I_l^{(i)}}$ is the parameter vector for the cluster centroid assigned to $l$-th MPC in the $i$-th iteration. The relation in Eq. (4.6) has been proposed by [67] as a formal definition of a cluster, i.e., for a given number of clusters, $N_c$, in parameter space, the clusters are chosen in order to minimize the global distance function, $D$ in Eq. (4.6). This selection also minimizes the cluster-spread in angle and delay domains amongst the possible partitions of MPCs into $N_c$ clusters.

For a given MIMO snapshot, the partition of MPCs into $N_c$ clusters is performed for $N_c$ spanning a range of values, $N_c \in [N_{c_{min}}, N_{c_{max}}]$. The KPowerMeans algorithm is executed for each value of $N_c$. From this set of candidate partitions of the MPCs, only *one* can be chosen to represent the measured snapshot. This task is performed by the *cluster validation* procedure. A combined application of two criteria, the Calinski-Harabasz and Davies-Bouldin indices, selects as an optimum partition the one that gives the most compact clusters and separated clusters.

Since the work in [67], the authors have developed significant variants of the initial automatic clustering approach. This includes joint cluster identification and tracking that is applicable to time-variant channels. A comprehensive overview of these efforts and related work can be found in [66].

# Chapter 5

# Contributions and Conclusions

This chapter summarizes the main research contributions of the included papers. Some general conclusions regarding the research area are also provided as a separate section.

## 5.1 Research contributions

My work has been supervised by Prof. Andreas F. Molisch as the main advisor, and Dr. Fredrik Tufvesson as co-advisor, both of whom are co-authors on all papers.[1] I am the main contributor to the scientific work presented in the included papers, the contributions of my co-authors are mentioned below each paper.

### 5.1.1 Paper I: "Outdoor-to-Indoor Office MIMO Measurements and Analysis at 5.2 GHz"

This paper presents results from one of the first measurements for a double-directional characterization of the outdoor-to-indoor wireless propagation channel. Such channels are of interest for both cellular and wireless LAN applications. We discuss physical aspects of building penetration, and also provide statistics of relevant channel parameters; the presented CDFs of angular spreads gauge spatial correlations that can be encountered in such scenarios,

---

[1] Dr Tufvesson has also participated in most of the measurements.

while similar analysis for the delay spreads gives an idea of the frequency selectivity. Our analysis highlights the fact that the Ricean $K$-factor does not necessarily have strict correspondence with the power of the LOS component. For modeling LOS channels it is proposed to use the LOS power factor, rather than the Ricean $K$-factor, for scaling the normalized LOS contribution. Our analysis of the small-scale fading also reveals that antenna elements, within some array configurations, may experience shadow fading. Therefore, the common practice of averaging the Rx signal over *all* array elements to remove small-scale fading, should be preceded by ruling out presence of shadow fading.

The paper investigates the coupling between DOD and DOA for the outdoor-to-indoor scenario, and the two spectra are found to have non-negligible dependence. We test the applicability of three analytical channel models that make different assumptions on the coupling between DODs and DOAs. Our results indicate that analytical models, that impose fewer restrictions on the DOD to DOA coupling, should be used preferrably over models such as the Kronecker model that have more restrictive assumptions.

This transaction paper is based on two conference papers and additional material. I wrote the manuscript, and performed the analysis with the exceptions noted as follows: for the first conference paper, the channel parameter extraction results were from an implementation of the SAGE by Gunnar Eriksson, Dr Peter Almers contributed to part of the paper-writing. Dr Almers and Dr Johan Karedal also contributed to the measurements. Prof. Andreas F. Molisch and Dr. Fredrik Tufvesson supervised the work.

### 5.1.2 Paper II: "A Cluster-based Analysis of Outdoor-to-Indoor Office MIMO Measurements at 5.2 GHz"

Numerous MIMO channel measurements show that MPCs tend to arrive at the Rx in clusters, i.e., groups of MPCs which have similar parameters such as TDOA, DOD, and DOA. The concept of MPC clusters is integral to many channel models, e.g., the COST 273 model, a generic model for MIMO propagation channels. This paper presents a cluster-based analysis of the outdoor-to-indoor MIMO measurements also analyzed in Paper I. A subset of parameters of the COST 273 channel model are characterized for the outdoor-to-indoor scenario. The MPC parameters are extracted for 159 measurement locations using the RIMAX algorithm, and the clusters of MPCs are identified using an automated clustering approach. In particular, our clustering approach requires that *all* MPC parameters must be similar in order for the MPCs to form a cluster. For a subset of the locations, results of the automated clustering method are also cross-checked with an independent visual clustering. A statistical analysis of the identified clusters is performed for both the intra- and inter-cluster properties. For the intra-cluster properties, the number of MPCs is observed to be exponentially distributed while the angle and delay-spreads are found to be log-normally distributed. For the intercluster properties, the distribution of number of clusters is found to be better represented by the exponential distribution rather than the Poisson distribution specified in the COST 273 model. The cluster delays are observed to follow a log-normal distribution.

I performed the statistical analysis on the clusters and wrote the manuscript. For MPC parameter extractions, I used a commercial implementation of RIMAX by MEDAV. Dr Nicolai Czink performed the automated cluster identification on the processed MPC data. Prof. Andreas F. Molisch and Dr. Fredrik Tufvesson supervised the work.

### 5.1.3 Paper III: "A Statistical Model for Indoor Office Wireless Sensor Channels"

Sensor networks have recently attracted interest due to potential use in industrial, environmental, and safety-related applications. Though the indoor channel for elevated access-point to mobile/laptop scenario is well investigated, there are relatively few investigations on channels for sensor deployment scenarios. Such channels present some unique properties due to the nodes placed typically in close proximity to the walls and floor. This paper analyzes the spatial fading distribution for a range of canonical sensor deployment scenarios. The presented results are relevant to communicating within, and between, clusters of nodes.

Results indicate that the fading channel is mostly Ricean distributed for both the same-wall and opposite-wall scenarios, though the Ricean $K$-factors are often not very large. Contrary to the widely accepted assumption in published literature that the channel is AWGN at a small-enough distance, our measurements indicate that values of the Ricean $K$-factor do not, in general, increase monotonically as the Tx-Rx distance is reduced. A probability mixture model is proposed, with distance dependent parameters, to account for the distance dependent variations of the $K$-factors.

A simulation model that includes small- and large-scale fading effects is presented. Acccording to the modeling approach, a sensor node placed anywhere within the spatial extent of a small-scale region will experience the channel statistics applicable to that region. Our model is relevant for SNR investigations and interference analysis between different links (small-scale regions) in the indoor office scenario.

I performed the analysis and modeling and also wrote the manuscript. Amit Singh and I did the measurements. Prof. Andreas F. Molisch and Dr. Fredrik Tufvesson supervised the work.

### 5.1.4 Paper IV: "Characterization of a Time-Variant Wireless Propagation Channel for Outdoor Short-Range Sensor Networks"

Outdoor short-range sensor networks are of interest for surveillance, environmental monitoring, and communications applications. The scenario most relevant for practical applications has the nodes at fixed positions near the ground, so that temporal variations occur only due to people/objects moving in the vicinity of the sensors. This paper presents sample results to characterize such channels.

The channel statistics of both the LOS path and the overall narrowband signal are non-stationary. Our analysis of the simultaneously measured links shows that the Rx signal strength is influenced significantly only when the LOS path is blocked. This means that for surveillance applications, it may not be sufficient to monitor the LOS path only but other small-scale parameters should additionally be used. A generic approach was presented to model temporally correlated samples of the narrowband channel. The time-variant Doppler spectrum of the channel's scattered components was shown to have a distinct pattern associated with the walking person (intruder). These characteristics can be valuable for early intruder detection schemes since significant spectral peaks are visible before the LOS crossing instant.

I wrote the manuscript, performed the analysis and modeling, except for the spectrum modeling of the channel's residue component, to which Telmo Santos has contributed. Amit Singh and I did the measurements. Prof. Andreas F. Molisch and Dr. Fredrik Tufvesson supervised the work.

## 5.2 Conclusions and Future Work

The wireless propagation channel significantly influences the received signal, so that it needs to be modeled effectively. Extensive measurements are required both for investigating the validity of theoretical models and postulating models based on measurements. Such measurements, analysis, and modeling have been the topic of this thesis.

Channel models are required to capture essential properties of the channel, e.g., it is well known that link-correlations in a MIMO channel will influence the type of gain achievable by MIMO techniques. Simultaneously, a model is also desired to be simple to use. In the context of MIMO systems, e.g., the Kronecker model has found widespread use in part because of its simple implementation, a factor that cannot be overlooked. Especially now, as MIMO systems are gradually incorporated into standards and products, the trade-off between complexity and feature-richness will be more in focus. While one is proposing simple models, I believe that clearly listing both the *strengths* and *limitations* of the model would help the intended user to make informed choices. On the other hand, for more complex models that may require many independent measurements to put numbers to parameters, I think it might help prospective users if the model were presented in a modular fashion with the possibility to have increasing feature-richness with complexity.

For double-directional analysis, different channel parameter estimation algorithms are in use in the research community. For paper I, we use the SAGE and later for paper II a commercial RIMAX implementation is used. It would be of interest to set up reference measurement scenarios where the performance of the two algorithms could be compared, with complete antenna data models. In this context it would be useful to gather additional information on the effects of incomplete data models as pointed out by Landmann et al [63].

The use of MPC clusters to describe the wireless channel has gained gradual acceptance. All major channel models, e.g. 3GPP SCM, WINNER, COST 273 etc. are based on the concept of MPC clusters. In view of the typically large volumes of data generated by processed MIMO measurements, I think that automated approaches for cluster identification should be the preferred way for doing cluster analysis. Furthermore, this approach also provides an inherent definition of a cluster.

The WSS assumption is invariably used in the theoretical analysis of wireless channels. Though in measured channels, stationarity intervals occur side by side with periods of non-stationarity such that, for analysis, the extent of a stationarity interval needs to be determined. I think this aspect should always be given careful consideration when analyzing measurement data. Of course one also has to consider the often competing requirement of having sufficient independent samples for statistical analysis. In paper II a moving average of Rx power is used to determine stationarity regions whereas in paper III the correlation between averaged power delay profiles is used for the same purpose. This is however an open topic of research and I think new methods will continue to be proposed.

For sensor scenarios, it would be of interest to track in time the location of the one or more people influencing the links during measurements. Also, I think that investigating the link correlations in more detail would be of interest in the context of distributed MIMO systems.

# References

[1] B. A. Austin, "Oliver Lodge - The Forgotten Man of Radio?," in *The Radioscientist & Bulletin*, vol. 5, (URSI, Gent, Belgium), pp. 12–16, March 1994.

[2] R. Simmons, "Guglielmo Marconi and early systems of wireless communications," *GEC Review*, vol. 11, no. 1, pp. 37–55, 1996.

[3] G. Heine, *GSM Networks: Protocols, Terminology and Implementation*. Artech House Publishers, 1998.

[4] V. Erceg, L. Schumacher, P. Kyritsi, D. S. Baum, A. F. Molisch, and A. Y. Gorokhov, "Indoor MIMO WLAN channel models," in *Standardization drafts of IEEE 802 meeting Dallas*, March 2003.

[5] D. Bakker, D. M. Gilster, and R. Gilster, *Bluetooth End to End*. USA: Wiley, 1st ed., 2002.

[6] J. A. Gutiérrez, E. H. Callaway, and R. L. Barrett, *Low-Rate Wireless Personal Area Networks: Enabling Wireless Sensors with IEEE 802.15.4*. IEEE Press, 2003.

[7] J. H. Winters, "On the capacity of radio communications systems with diversity in Rayleigh fading environments," *IEEE Journal on Selected Areas in Communications*, vol. 5, pp. 871–878, June 1987.

[8] G. J. Foschini and M. J. Gans, "On limits of wireless communications in a fading environment when using multiple antennas," *Wireless Personal Communications: An International Journal*, vol. 6, pp. 311–335, 1998.

[9] I. E. Telatar, "Capacity of multi-antenna Gaussian channels," *European Transactions on Telecommunications*, vol. 10, November–December 1999.

[10] A. F. Molisch, *Wireless Communications*. Chichester, U.K.: IEEE Press - Wiley, 2005.

[11] A. Paulraj, D. Gore, R. Nabar, and H. Bolcskei, “An overview of MIMO communications - a key to gigabit wireless,” *Proceedings of the IEEE*, vol. 92, no. 2, pp. 198–218, 2004.

[12] IEEE P802.11n/D1.0 March 2006, “Draft amendment to standard for information technology telecommunications and information exchange between systems - local and metropolitan networks - specific requirements part 11: Wireless LAN medium access control (MAC) and physical layer (PHY) specifications: Enhancements for higher throughput,” tech. rep., 2006.

[13] 3GPP TR 25.814 V1.2.2, “Physical layer aspects for evolved UTRA (Release 7),” tech. rep., 3GPP and 3GPP2, March, 2006.

[14] W. Weichselberger, *Spatial Structure of Multiple Antenna Radio Channels.* PhD thesis, Vienna University of Technology, Austria, 2003.

[15] A. Paulraj, D. Gore, and R. Nabar, *Multiple antenna systems.* Cambridge, U.K.: Cambridge University Press, 2003.

[16] J. B. Andersen, “Array gain and capacity for known random channels with multiple element arrays at both ends,” *IEEE Journal on Selected Areas in Communications*, vol. 18, pp. 2172–2178, November 2000.

[17] R. Vaughan and J. B. Andersen, *Channels, Propagation and Antennas for Mobile Communications.* London, U.K.: IEE, 1st ed., 2003.

[18] G. L. Stuber, *Principles of Mobile Communication.* Massachusetts, USA: Kluwer Academic Publishers, 2nd ed., 2001.

[19] V. Tarokh, A. Naguib, N. Seshadri, and A. Calderbank, “Combined array processing and space-time coding,” *Information Theory, IEEE Transactions on*, vol. 45, no. 4, pp. 1121–1128, 1999.

[20] V. Tarokh, N. Seshadri, and A. Calderbank, “Space-time codes for high data rate wireless communication: performance criterion and code construction,” *Information Theory, IEEE Transactions on*, vol. 44, no. 2, pp. 744–765, 1998.

[21] D. Gesbert, M. Shafi, D. Shiu, P. J. Smith, and A. Naguib, “From theory to practice: An overview of MIMO space time coded wireless systems,” *IEEE Journal on Selected Areas in Communications*, vol. 21, pp. 281–302, April 2003.

[22] A. Willig, K. Matheus, and A. Wolisz, “Wireless technology in industrial networks,” *Proceedings of the IEEE*, vol. 93, no. 6, pp. 1130–1151, 2005.

[23] J. Yick, B. Mukherjee, and D. Ghosal, “Wireless sensor network survey,” *Computer Networks*, vol. 52, no. 12, p. 2292, 2008.

[24] I. F. Akyildiz, T. Melodia, and K. R. Chowdhury, “A survey on wireless multimedia sensor networks,” *Computer Networks*, vol. 51, pp. 921–960, October 2007.

[25] O. Gassmann and H. Meixner(eds.), *Sensors in intelligent buildings*. Wiley-VCH, sensor applications vol. 2 ed., 2001.

[26] P. Zhang and M. Chen, “A remote health care system based on wireless sensor networks,” in *Proc. International Conference on Computer Supported Cooperative Work in Design*, pp. 1102–1106, 2008.

[27] Y. Hong, W. Huang, F. Chiu, and C. Kuo, “Cooperative communications in resource-constrained wireless networks,” *IEEE Signal Processing Magazine*, vol. 24, no. 3, pp. 47–57, 2007.

[28] J. N. Laneman, D. N. C. Tse, and G. W. Wornell, “Cooperative diversity in wireless networks:efficient protocols and outage behaviour,” *IEEE transactions on information theory*, vol. 50, pp. 3062–3080, December 2004.

[29] I. Howitt and J. Gutierrez, “IEEE 802.15.4 low rate - wireless personal area network coexistence issues,” *Wireless Communications and Networking*, vol. 3, pp. 1481–1486, 2003.

[30] ZigBee: wireless control that simply works http://www.zigbee.org.

[31] Hart - The logical wireless solution http://www.hartcomm2.org.

[32] J. D. Parsons, *The mobile radio propagation channel*. Chichester, U.K.: John Wiley and Sons, 2nd ed., 2001.

[33] A. Saleh and R. A. Valenzuela, “A statistical model for indoor multipath propagation,” *IEEE J. Selected Areas Comm.*, vol. 5, pp. 128–137, February 1987.

[34] A. F. Molisch, “Ultrawideband propagation channels - theory, measurement, and modeling,” *IEEE Transactions on Vehicular Technology*, vol. 54, no. 5, pp. 1528–1545, 2005.

[35] T. S. Rappaport, *Wireless Communications: Principles and Practice*. New Jersey: Prentice Hall, 2nd ed., 2002.

[36] J. G. Proakis, *Digital Communications.* N.Y.: Mc Graw Hill, 4th ed., 2001.

[37] P. A. Bello, “Characterization of randomly time-variant linear channels,” *IEEE Transactions*, pp. 360–393, December 1963.

[38] A. Gehring, M. Steinbauer, I. Gaspard, and M. Grigat, “Empirical channel stationarity in urban environments,” in *Proc. 4th European Personal Mobile Communications Conference (EPMCC '01)*, (Vienna, Austria), February 2001.

[39] R. Bultitude, “Methods for estimating and modeling consistency intervals, and the detection and simulation of changes on mobile radio channels,” in *COST 2100, TD(08) 424*, (Wroclaw, Poland), February 2008.

[40] M. Herdin and E. Bonek, “A MIMO correlation matrix based metric for characterizing non-stationarity,” in *Proc. IST Mobile and Wireless Communications Summit*, (Lyon, France), June 2004.

[41] P. Almers, E. Bonek, A. Burr, N. Czink, M. Debbah, V. Degli-Esposti, H. Hofstetter, P. Kyoesti, D. Laurenson, G. Matz, A. Molisch, C. Oestges, and H. Oezcelik, “Survey of channel and radio propagation models for wireless MIMO systems,” *EURASIP J. Wireless Commun. Networking*, vol. 2007, 2007.

[42] M. Steinbauer, A. F. Molisch, and E. Bonek, “The double-directional radio channel,” *IEEE Antennas and Propagation Magazine*, vol. 43, pp. 51–63, August 2001.

[43] M. Steinbauer and A. F. Molisch, “Directional channel models,” in *Flexible Personalized Wireless Communications* (L. Correia, ed.), ch. 3.2, pp. 135–144, Wiley, 2001.

[44] B. H. Fleury, M. Tschudin, R. Heddergott, D. Dahlhaus, and K. Pedersen, “Channel parameter estimation in mobile radio environments using the SAGE algorithm,” *IEEE Journal on Selected Areas in Communications*, vol. 17, pp. 434–450, March 1999.

[45] A. Richter, *Estimation of Radio Channel Parameters: Models and Algorithms.* PhD thesis, Ilmenau Technical University, Germany, 2005.

[46] G. DelGaldo, V. Algeier, N. Czink, and M. Haardt, “Objects spatial localization from high-resolution parameter estimation on measurements,” in *NEWCOM-ACORN Workshop*, (Vienna, Austria), 2006.

[47] M. Landmann, M. Kaeske, R. Thoma, J. Takada, and I. Ida, “Measurement based parametric channel modeling considering diffuse scattering and specular components,” in *Proc. International Symposium on Antennas and Propagation*, (Niigata, Japan), August 2007.

[48] D. Hampicke, C. Schneider, M. Landmann, A. Richter, G. Sommerkorn, and R. S. Thoma, “Measurement-based simulation of mobile radio channels with multiple antennas using a directional parametric data model,” in *Proc. IEEE Vehicular Technology Conference VTC-2001 Fall*, vol. 2, pp. 1073–1077, 2001.

[49] R. Valenzuela, “A ray tracing approach to predicting indoor wireless transmission,” in *Proc. IEEE Vehicular Technology Conference*, pp. 214–218, 1993.

[50] M. Lawton and J. McGeehan, “The application of a deterministic ray launching algorithm for the prediction of radio channel characteristics in small-cell environments,” *IEEE Transactions on Vehicular Technology*, vol. 43, pp. 955–969, Nov 1994.

[51] A. F. Molisch, “A generic channel model for MIMO wireless propagation channels in macro- and microcells,” *IEEE Trans. Signal Processing*, vol. 52, pp. 61–71, Jan. 2004.

[52] J. W. Wallace and M. A. Jensen, “Modeling the indoor MIMO wireless channel,” *Antennas and Propagation, IEEE Transactions on*, vol. 50, no. 5, pp. 591–599, 2002.

[53] P. Soma, D. S. Baum, V. Erceg, R. Krishnamoorthy, and A. J. Paulraj, “Analysis and modeling of multiple-input multiple-output (MIMO) radio channel based on outdoor measurements conducted at 2.5 GHz for fixed BWA applications,” in *Proc. IEEE ICC 2002*, vol. 1, pp. 272–276.

[54] J. P. Kermoal, L. Schumacher, K. I. Pedersen, P. E. Mogensen, and F. Frederiksen, “A stochastic MIMO radio channel model with experimental validation,” *IEEE Journal on Selected Areas in Communications*, vol. 20, pp. 1211–1226, August 2002.

[55] W. Weichselberger, M. Herdin, H. Özcelik, and E. Bonek, “A stochastic MIMO channel model with joint correlation of both link ends,” *IEEE Transactions on wireless Communications*, vol. 5, pp. 90–100, January 2006.

[56] A. M. Sayeed, “Deconstructing multiantenna fading channels,” *IEEE Transactions on Signal processing*, vol. 50, pp. 2563–2579, October 2002.

[57] 3GPP-3GPP2 Spatial Channel Model Ad-hoc Group 3GPP TR 25.996, "Spatial channel model for multiple input multiple output MIMO simulations," tech. rep., 2003. v6.1.0(2003-09).

[58] L. Correia, ed., *COST 273 final report: Towards mobile broadband multimedia networks.* Amsterdam, The Netherlands: Elsevier, 2006.

[59] MEDAV GmbH, http://www.channelsounder.de.

[60] T. Pedersen, C. Pedersen, X. Yin, and B. Fleury, "Optimization of spatiotemporal apertures in channel sounding," *Signal Processing, IEEE Transactions on*, vol. 56, pp. 4810–4824, October 2008.

[61] R. Thomae, D. Hampicke, A. Richter, G. Sommerkorn, A. Schneider, U. Trautwein, and W. Wirnitzer, "Identification of the time-variant directional mobile radio channels," *IEEE Trans. Instrum. Meas.*, vol. 49, pp. 357–364, 2000.

[62] M. Haardt and J. Nossek, "Unitary esprit: how to obtain increased estimation accuracy with a reduced computational burden," *IEEE Transactions on Signal Processing*, vol. 43, pp. 1232–1242, May 1995.

[63] M. Landmann, W. Kotterman, and R. Thoma, "On the influence of incomplete data models on estimated angular distributions in channel characterisation," in *Proc. European Conference on Antennas and Propagation (EuCAP)*, 2007.

[64] L. Vuokko, P. Vainikainen, and J. Takada, "Clusters extracted from measured propagation channels in macrocellular environments," *IEEE Transactions on Antennas and Propagation*, vol. 53, pp. 4089–4098, December 2005.

[65] J. Fuhl, A. F. Molisch, and E. Bonek, "Unified channel model for mobile radio systems with smart antennas," in *Proc. IEE Radar, Sonar and Navigation*, vol. 145, pp. 32–41, February 1998.

[66] N. Czink, *The Random-Cluster Model - A Stochastic Channel Model for Broadband Wireless Communication Systems of the 3rd Generation and Beyond.* PhD thesis, Vienna University of Technology, Austria, 2007.

[67] N. Czink, P. Cera, J. Salo, E. Bonek, J.-P. Nuutinen, and J. Ylitalo, "A framework for automatic clustering of parametric MIMO channel data including path powers," in *Proc. IEEE Vehicular Technology Conference (VTC-2006 Fall)*, (Montreal, Canada), September 2006.

[68] M. Steinbauer, H. Özcelik, H. Hofstetter, C. F. Mecklenbräuker, and E. Bonek, “How to quantify multipath separation,” *IEICE Trans. Electron.*, vol. E85-C, pp. 552–557, March 2002.

[69] J. Han and M. Kamber, *Data Mining, Concepts, and Techniques.* San Francisco, USA: Morgan Kaufmann Publishers, 2001.

# Part II

# Included Papers

# *Paper I*

# Outdoor-to-Indoor Office MIMO Measurements and Analysis at 5.2 GHz

## Abstract

The outdoor-to-indoor wireless propagation channel is of interest for cellular and wireless LAN applications. This paper presents measurement results and analysis based on our multiple-input multiple-output (MIMO) measurement campaign, which is one of the first to characterize the outdoor-to-indoor channel. Measurements were performed at 5.2 GHz; the receiver was placed indoors at 53 different locations in an office building, the transmitter was placed at three ”base station” positions on a nearby rooftop. We report on the root mean square (RMS) angular spread, building penetration, and other statistical parameters characterizing the channel. Our analysis is focused on three MIMO channel assumptions often used in stochastic models. (i) It is commonly assumed that the channel matrix can be represented as a sum of a line-of-sight (LOS) contribution and a zero-mean complex Gaussian distribution; our investigation shows that this model does *not* adequately represent our measurement data. (ii) It is often assumed that the Rician $K$-factor is equal to the power ratio of the LOS component and the other multipath components (MPCs); we show that this is not the case and we highlight the difference between the Ricean $K$-factor often associated with LOS channels, and a similar power ratio for the estimated LOS MPC. (iii) A widespread assumption is that the full correlation matrix of the channel can be decomposed into a Kronecker product of the correlation matrices at transmit and receive array. Our investigations show that the direction-of-arrival (DOA) spectrum depends noticeably on the direction-of-departure (DOD), therefore the Kronecker model is not applicable and models with less restrictive assumptions on the channel, e.g., the Weichselberger model or the full correlation model, should be used.

---

S. Wyne, A. F. Molisch, P. Almers, G. Eriksson, J. Karedal and F. Tufvesson,
“Outdoor-to-Indoor Office MIMO Measurements and Analysis at 5.2 GHz,”
in *IEEE Transactions on Vehicular Technology*, vol. 57, no. 3, pp. 1374–1386, May 2008.

# 1 Introduction

MIMO systems can result in tremendous capacity improvements over single antenna systems [1], [2]. However, the capacity gains depend on the propagation channel in which the system operates. The most important requirement for any channel model is agreement with reality, hence measurement of propagation channels and subsequent parameterization of models based on these measurements are critically important. There are a number of double-directional outdoor-to-outdoor and indoor-to-indoor measurement results reported in the literature, e.g., [3], [4], [5], [6], and [7]. However, there has been a remarkable lack of outdoor-to-indoor measurement results, though the outdoor-to-indoor scenario has important applications for voice-data transmission in third generation cellular systems, as well as wireless LANs. The measurement campaign reported in this paper (first published in [8]), together with [9] and [10] are the first published results of outdoor-to-indoor measurements characterizing the MIMO channel.

There are two main categories of channel models for MIMO systems, both of which will be used in this paper; the *double-directional* channel models [3] describe the MIMO channel by parameters of the multipath components; DOD, DOA, delay, and complex amplitudes. A double-directional channel characterization is highly useful because it is independent of antenna configurations and describes the physical propagation alone, and serves to point out the dominant propagation mechanisms. On the other hand, *analytical* channel models describe the statistics of the transfer function matrix; each entry in that matrix gives the transfer function from the $i$-th transmit to the $j$-th receive antenna element. Almost all of the analytical channel models, with the exception of the keyhole model [11], are based on the assumption that the entries of the transfer function matrix are *zero-mean* complex Gaussian, with the possible addition of a LOS component. Furthermore, many models describe the correlation matrix of those entries as a Kronecker product of the correlation matrices at the transmit and receive side. The first assumption has, to our knowledge, generally remained unquestioned.[2] The Kronecker assumption has been discussed more extensively recently [13], [7]. While measurement data from outdoor scenarios seem to indicate good agreement with this assumption [13], indoor data seem to deviate more [14], and as a consequence a more general model has, e.g., been developed by Weichselberger et al. [7].

In this paper we present the results of a double-directional MIMO channel measurement campaign, for an outdoor-to-indoor office scenario, carried out at 5.2 GHz, and evaluate the validity of the standard assumptions of analytical channel models (first results were published in [15]). Our main contributions are:

- We analyze the DOD and DOA, and discuss the dominant propagation mechanisms.
- We give the distributions of RMS directional spreads and delay spreads.

---

[2] With the exception of the rare “keyhole scenario”, see [11], [12].

- We present a statistical analysis of the measured fading and compare it with popular models.
- We investigate the validity of the “LOS-plus-Gaussian-remainder” assumption, and show that it does not hold for all measurement locations in our campaign.
- We explain this result by investigating in detail the difference between “LOS power factor” and “Rician $K$-factor”.
- We analyze the validity of the Kronecker model, and present detailed results on the coupling between DOAs and DODs.

The paper is organized as follows: Sec. II describes the measurement setup and scenario, and the procedure for data evaluation, whereas in Sec. III, the physical propagation processes are described. Furthermore, Sec. IV contains an analysis of the dispersion in angular and delay domains, and Sec. V compares three analytical channel models. Finally, in Sec. VI, we summarize the results.

# 2 Measurement Setup and Evaluation

## 2.1 Equipment and Scenario

For the measurements, we used the RUSK ATM [16] channel sounder to measure the transfer function between transmit (Tx) and receive (Rx) antenna elements. This sounder uses the multiplexing principle (subsequently connecting the Tx, and Rx, antenna elements to the RF chains) for obtaining MIMO transfer function matrices. Measurements were performed at a center frequency of 5.2 GHz and a signal bandwidth of 120 MHz, using a transmit power of 33 dBm. The Tx antenna was an 8-element dual polarized uniform linear array (ULA) of patch elements with element spacing $\approx \lambda/2$ (half-wavelength); we only considered the 8 vertically polarized elements in our analysis. The Rx antenna was a 16-element uniform circular array (UCA) of vertically polarized monopole elements, radius $\approx \lambda$. Both array configurations were calibrated prior to measurement so that array response data was available for application of high resolution algorithms. The Tx signal had a period of 1.6 $\mu$s and the sampling time for one MIMO snapshot was 819 $\mu$s, which is within the coherence time of the channel. At each Rx location, 13 snapshots were measured with a time spacing of 4.1 ms between successive snapshots. Our measurement results directly give the channel transfer function matrix sampled at 193 frequency sub-channels. For the double-directional channel characterization, we needed the parameters delay, DOA, DOD, and complex amplitude of the MPCs. Those were obtained with the high-resolution SAGE algorithm [17], see Sec. 2.2 for details.

The test site is the E building at LTH, Lund University, Sweden; a map of the site is shown in Fig. 1. The transmitter was placed at 3 different positions on the roof of a nearby building. For each Tx position, the receiver was placed at 53 measurement positions located in 8 different rooms and the corridor between the rooms. Measurement positions in each room were placed on a $3 \times 3$ grid spanning an area of approximately $6 \times 3$ m$^2$; the three positions in north - south direction were

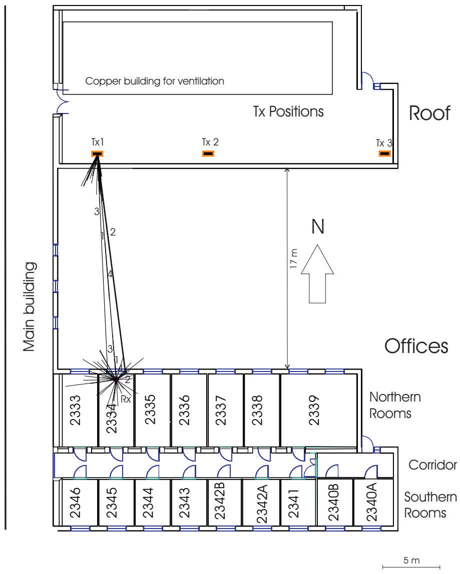

**Figure 1:** Site map showing locations of Tx (2nd floor) and Rx positions (1st floor). The free space distance between the blocks is also indicated. 4-7 positions were measured in room: 2334, 2336, 2337,2339 (referred to as north) and 2345, 2343, 2342A, 2340B (referred to as south).

denoted north, middle and south, and the three positions in east - west direction were denoted east, middle and west. The Rx position in a room was described by a pair of letters suffixed to the room number, to indicate north-south and east-west position, respectively. As a sample result, Fig. 1 shows the strongest four of the estimated MPCs for Tx position 1, and receiver placed at 2334NM.

## 2.2 SAGE Analysis

### Signal Model

The data evaluation is based on the assumption that the received and transmitted signals can be described as a finite number of plane waves [18]:

$$h_{m,n}\left(k,i,\alpha_l,\tau_l,\phi_l^{\mathrm{Rx}},\phi_l^{\mathrm{Tx}},\nu_l\right)= \tag{1}$$

$$\sum_{l=1}^{L}\alpha_l e^{-j2\pi\Delta f\tau_l k}G_{\mathrm{Tx}}\left(n,\phi_l^{\mathrm{Tx}}\right)G_{\mathrm{Rx}}\left(m,\phi_l^{\mathrm{Rx}}\right)e^{j2\pi\Delta t\nu_l i},$$

where $L$ is the total number of extracted MPCs, $\alpha_l, \tau_l, \phi_l^{\mathrm{Rx}}, \phi_l^{\mathrm{Tx}}, \nu_l$ are complex amplitude, delay, DOA in azimuth, DOD in azimuth and Doppler frequency, respectively, of the $l-$th MPC. The impact of elevation is neglected. Furthermore $k, i, m, n, G_{\mathrm{Rx}}$, $G_{\mathrm{Tx}}$ are frequency sub-channel index, snapshot index, Rx element number, Tx element number, Rx antenna pattern and Tx antenna pattern, respectively. Based on this data model the SAGE algorithm can, using an iterative method, provide a maximum-likelihood estimate of the MPC parameters from the measured transfer functions. In our evaluations, we used 30 iterations of the algorithm.

All 13 snapshots that were taken at a given Rx position were used in data processing, 40 MPCs being extracted from each measurement position. The path parameters, DOA, DOD, and delay were cross-checked at a number of positions with the geometry of the measurement site, and provided a good match. It must be stressed that high-resolution algorithms based on the sum-of-plane-waves model cannot explain all possible propagation processes. For example, diffuse reflections, as well as spherical waves, are not covered by the model of Eq. (1). For this reason, the total power of the MPCs extracted by SAGE does not necessarily equal the total power of the signals observed at the antenna elements. This can be compounded by the fact that for some locations, more than 40 MPCs might carry significant energy. A quantitative discussion of this is given in Sec. 2.2.

The estimated Doppler frequency for most MPCs was less than 1 Hz, though at a few locations, Doppler frequencies of around 2-3 Hz were measured. Since the inverse of the Doppler frequency was significantly larger than the total measurement duration of 13 snapshots, this indicates a relatively static measurement scenario.

### Relative Extracted Power

The received power estimated by SAGE is dependent on, e.g., the environment and the number of extracted MPCs, $L$. The relative extracted power is computed as[3]

$$Q(L) = \frac{\left\|\hat{\mathbf{H}}(L)\right\|_F^2}{\|\mathbf{H}_{\mathrm{meas}}\|_F^2 - \hat{\sigma}_n^2}, \tag{2}$$

where $\mathbf{H}_{\mathrm{meas}}$ is the measured transfer matrix, $\hat{\mathbf{H}}(L)$ is the channel matrix reconstructed from the SAGE estimates of $L = 40$ MPCs inserted into the channel model of Eq. 1. The estimate of the noise power, $\hat{\sigma}_n^2$, was calculated at each measurement

---

[3] We use the following notation throughout the paper: $\hat{\mathbf{A}}$ denotes estimate of $\mathbf{A}$, $\|\mathbf{A}\|_F$ denotes Frobenius norm of matrix $\mathbf{A}$, $\mathbf{A}^T$ denotes transpose($\mathbf{A}$), $\mathbf{A}^*$ denotes conjugate($\mathbf{A}$), $\mathbf{A}^H$ denotes $(\mathbf{A}^*)^T$, and $\mathbf{A}^{\frac{1}{2}}$ is the matrix square-root defined in this work as $\mathbf{A}^{\frac{1}{2}}\left(\mathbf{A}^{\frac{1}{2}}\right)^H = \mathbf{A}$. The operator vec$\{\mathbf{A}\}$ stacks the columns of $\mathbf{A}$ on top of each other, and un-vec$\{\mathbf{A}\}$ is the inverse operation. Furthermore, $tr\{\mathbf{A}\}$ is trace($\mathbf{A}$), $\mathbf{A}_{ij}$ is the entry in $i$-th row and $j$-th column of $\mathbf{A}$, and $\mathbf{A} \odot \mathbf{B}$ is the element-wise product of $\mathbf{A}$ with matrix $\mathbf{B}$. Lastly, $\mathbf{G}$ is a random matrix with elements which are independent identically distributed *zero-mean* circularly symmetric complex Gaussian random variables with unit variance.

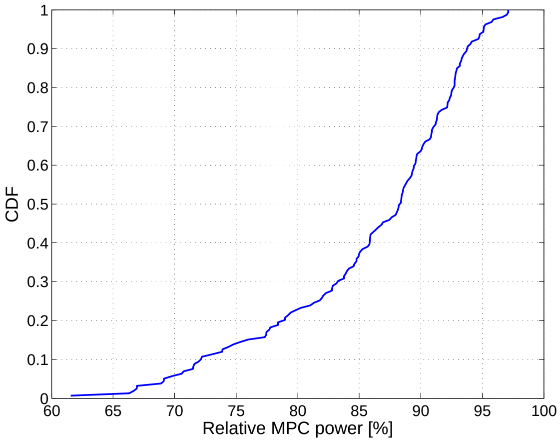

**Figure 2:** CDF of power captured by 40 estimated MPCs, expressed as the percentage of the power calculated from measured transfer matrix. All 159 measurement positions have been used in calculating the CDF.

position as

$$\hat{\sigma}_n^2 = \sum_{i=1}^{I-1} \frac{\|\mathbf{H}_{i+1} - \mathbf{H}_i\|_F^2}{2\,(I-1)} \tag{3}$$

where $\mathbf{H}_i$ is the measured channel transfer matrix for the $i-$th snapshot, and $I$ is the total number of snapshots. This noise estimation was possible because we have an (approximately) time-invariant channel, which we confirmed from our measurements (see above). The cumulative distribution function (CDF) of the relative extracted power is shown for all 159 locations in Fig. 2. As seen from the figure, the extracted power with a source order of 40, varies significantly over the measurement locations. In the majority of measurement locations more than 85% of the power is captured, though at some positions only about 60% of the power is captured.

## Source order Effects

For different initial estimates of the source order, we have investigated the mean square reconstruction error between measured data and the matrix reconstructed from MPC parameters estimated by SAGE. For each initial estimate of the source order, in the range from 1 to 100 MPCs, the mean square relative reconstruction error

($MSRRE$) was defined as

$$MSRRE = E\left[\frac{\left\|\mathbf{H}_{\text{meas}} - \hat{\mathbf{H}}_{\text{reconstruct}}\right\|_F^2}{\left\|\mathbf{H}_{\text{meas}}\right\|_F^2}\right], \tag{4}$$

where $\mathbf{H}_{\text{meas}}$ is the $N_R \times N_T$ measured channel and $\hat{\mathbf{H}}_{\text{reconstruct}}$ is the matrix reconstructed by Eq. (1) from MPCs estimated by SAGE. The expectation is over different frequency sub channels in one measured time snapshot which we use as realizations of the channel. The error from Eq. (4) is plotted in Fig. 3 for a typical LOS and NLOS scenario. It can be observed from Fig. 3 that as we increase the source order (collect more MPCs), the slope of the reconstruction error flattens out which can be interpreted as an indication that we begin to estimate noise spikes (or that we begin to estimate wave parameters that have small correlation peaks in the M-step of the SAGE). By extracting 40 MPCs at each location, we are not in the flat part of the reconstruction error curve which suggests that we do not estimate noise spikes as specular components. As a further check, we have also verified for each measurement that the difference in power between the strongest and weakest MPCs estimated by SAGE is within the dynamic range of our channel sounder, and within the sum (in dB) of the correlation gain provided by SAGE and the measurement SNR at the respective location so as to lower the probability that we estimate noise spikes. Though Fig. 3 may suggest that extracting 40 MPCs could lead to an under-estimated source order, especially for the NLOS scenarios, we believe (based on sample evaluations not presented here) that the potential difference in source order will not alter significantly the results presented in this paper. In general, correct source order estimation is an open research topic, and in the extreme case a source order of a few thousand has been used [19].

# 3 Physical Propagation Processes

In Fig. 4 the 40 extracted MPCs are plotted for each of the 53 Rx positions corresponding to Tx position 1. The line lengths represent the MPC amplitudes at each measurement location, relative to the strongest MPC at the same location.

This figure allows us to make some important conclusions about the dominant propagation processes:

- In the north rooms, propagation through walls and windows shows almost equal efficiency, as one can see from the (relative) strength of the LOS components in the different rooms. The reason lies in the strong attenuation by the windows as well as the walls. The (exterior) walls consist of bricks and reinforced concrete, whereas the windows are coated with a metallic film for energy conservation.[4] Additional measurements of the propagation characteristics of walls

---

[4] In most countries with cold climate, such metal-coated windows are typically used in residential and office buildings.

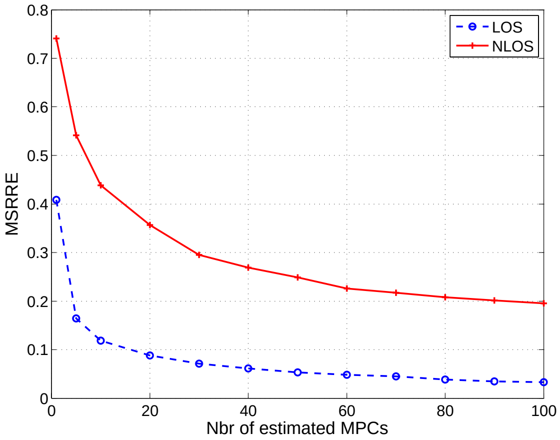

**Figure 3:** Mean square relative reconstruction error between measured data and the SAGE signal model for different souce order. A typical LOS and NLOS scenario are shown.

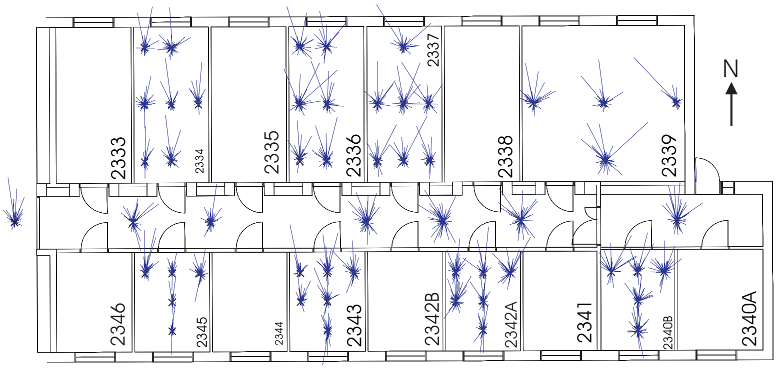

**Figure 4:** DOAs at all receiver positions for transmit position 1. North corresponds to 180° DOA

and windows showed that the attenuation of the windows is actually slightly larger than the attenuation of the walls.

- Reflection and diffraction by the window frames are efficient propagation mechanisms. This is evident, e.g., from the DOAs in the rooms 2334 and 2336. It is especially noteworthy that the propagation via the frames of the windows results in an attenuation similar to the attenuation of the brick wall, e.g., see the delay-azimuth plots for position Tx1Rx2336NM in Fig. 5.
- Each window is split into two glass panes, by a horizontal middle section with a metal handle and locking mechanism. There are strong MPCs coming from the window direction, see e.g., position Tx1Rx2336NM. The delay-azimuth plot in Fig. 5 shows a number of MPCs of similar strength and very similar delays (note that the DOAs are around 180° which corresponds to the window direction).
- For some south rooms, propagation through north rooms via doors constitutes a strong propagation mechanism. This is clearly seen, e.g., in the delay-azimuth plot for position Tx1Rx2343SM in Fig. 5.
- There are strong reflections observed in the south rooms, coming from south. These reflections are from structures along the south walls of the rooms, e.g., metal pipes of heaters mounted on the south wall; refer Fig. 5 for position Tx1Rx2343SM.
- While the strengths of the MPCs are differing widely, the directions of the MPCs are more uniformly distributed. Typically, only two or three MPCs show similar DOAs, e.g., refer Fig. 4. All DODs, on the other hand, are closely grouped together.

Similar results were observed for all three Tx positions.

# 4 Statistical Analysis of Angular and Delay Dispersion

## 4.1 Angular Dispersion

The angular dispersion is an important parameter for the characterization of a spatial channel. In this paper we use *direction-spread* [20] as a measure for the angular dispersion. The *direction-spread* parameter does not suffer from the ambiguity related to the choice of the origin of the coordinate system. The RMS direction-spread is calculated as[5]

$$\sigma_{\text{ang}} = \sqrt{\sum_{l=1}^{L} \left| e^{j\phi_l} - \mu_{\text{ang}} \right|^2 P_{\text{ang}}\left(\phi_l\right)}, \tag{5}$$

---

[5] In [20] "direction" is given by the unity vector in the spherical coordinate system. The *direction-spread* is a dimensionless quantity.

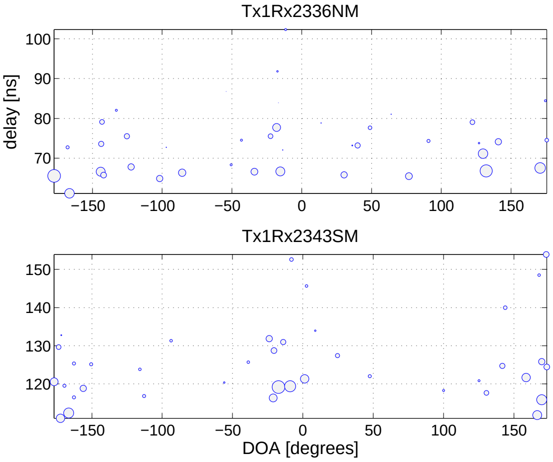

**Figure 5:** Joint delay-azimuth plot for two Rx positions. The marker diameter is scaled according to the relative power (dB) of each MPC, and the MPC powers are normalized with the power of the strongest MPC extracted at the respective Rx position. Measurement position is indicated in each subplot. Note the different scaling for the delay axis.

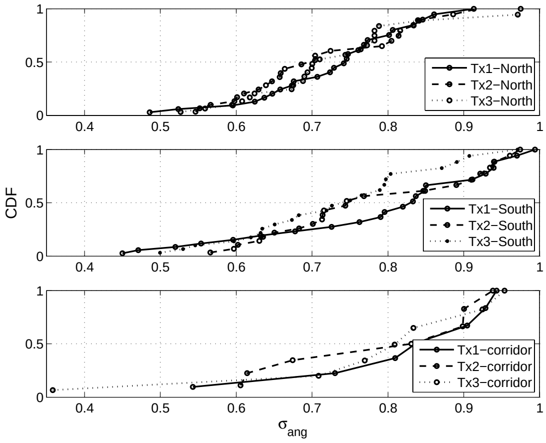

**Figure 6:** CDFs of the RMS DOA spread. The subplots from top to bottom are for the north rooms, south rooms, and the corridor, respectively.

where

$$\mu_{\text{ang}} = \sum_{l=1}^{L} e^{j\phi_l} P_{\text{ang}}(\phi_l) \,. \tag{6}$$

$P_{\text{ang}}(\phi_l)$ is the angular power spectrum normalized as $\sum_L P_{\text{ang}}(\phi_l) = 1$. Figs. 6 and 7 present the CDF of the DOA and DOD spreads for different Tx and Rx locations. The differences between the north and the south rooms are evident, especially at the Rx side. In the corridor, the spread is close to that of the south offices. The mean direction-spreads are presented in Table 1. We can see immediately that the angular dispersion at the Rx is markedly higher than for the Tx; this result is intuitive, as the Tx is located outdoors and radiates only towards the Rx, while the Rx sees MPCs that can come through the windows and walls, or are reflected from walls all around the Rx. Furthermore, it is evident that the transmit position does not affect the mean value of the DOA spread, and there is no large difference in mean spread for the north rooms, corridor, and the south rooms. However, there are large differences in the DOD spread for the different transmit positions. The coupling between the DOAs and DODs will be discussed in Sec. 5.3

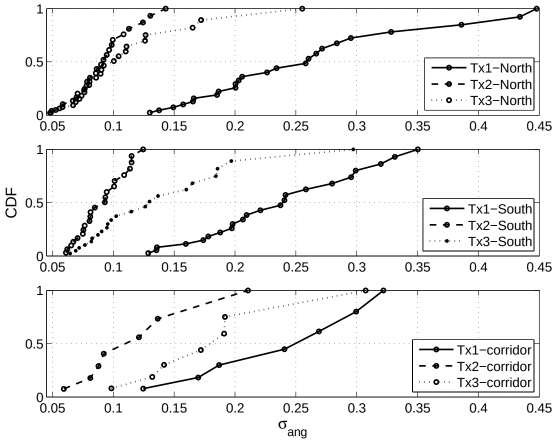

**Figure 7:** CDFs of the RMS DOD spread. The subplots from top to bottom are for the north rooms, south rooms, and the corridor, respectively.

**Table 1:** Mean direction spread.

| DOA | $\bar{\sigma}_{\text{ang}}$ | | |
|---|---|---|---|
| | north rooms | corridor | south rooms |
| Tx1 | 0.69 | 0.82 | 0.75 |
| Tx2 | 0.69 | 0.75 | 0.75 |
| Tx3 | 0.69 | 0.75 | 0.69 |

| DOD | $\bar{\sigma}_{\text{ang}}$ | | |
|---|---|---|---|
| | north rooms | corridor | south rooms |
| Tx1 | 0.24 | 0.24 | 0.23 |
| Tx2 | 0.09 | 0.11 | 0.09 |
| Tx3 | 0.10 | 0.18 | 0.13 |

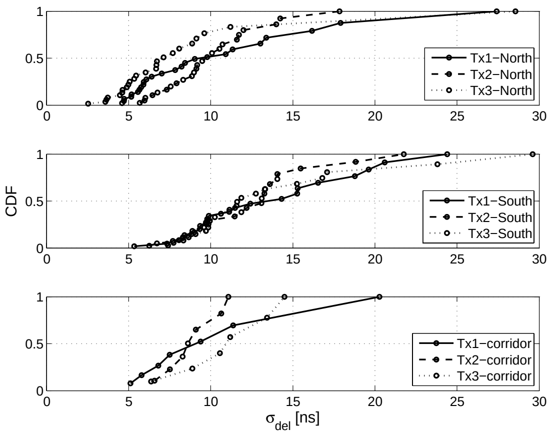

**Figure 8:** CDF of the RMS delay spread for the north and south rooms and the corridor.

## 4.2 Delay Dispersion

The RMS delay spread roughly characterizes the multipath propagation in the delay domain and is conventionally defined as [21]

$$\sigma_\tau = \sqrt{\bar{\tau^2} - (\bar{\tau})^2}, \tag{7}$$

where the mean excess delay, $\bar{\tau}$, and the non-central second moment of the average power delay profile, $\bar{\tau^2}$, are defined as [21]

$$\bar{\tau} = \frac{\sum\limits_{L} P_{\mathrm{del}}\left(\tau_l\right)\tau_l}{\sum\limits_{L} P_{\mathrm{del}}\left(\tau_l\right)} \text{ and } \bar{\tau^2} = \frac{\sum\limits_{L} P_{\mathrm{del}}\left(\tau_l\right)\tau_l^2}{\sum\limits_{L} P_{\mathrm{del}}\left(\tau_l\right)}, \tag{8}$$

where $P_{\mathrm{del}}\left(\tau_l\right)$ is the delay power spectrum and $\tau_l$ is the delay of the $l-$th MPC. Fig. 8 presents the CDF for the RMS delay spread in the north and south rooms. The delay spread has been evaluated using the MPCs as extracted from the SAGE algorithm. This has the drawback that diffuse contributions are not reflected in the obtained delay spreads (which therefore tend to be somewhat low). On the other hand, delay spread values that are extracted directly from the measured power delay profiles show much too high values, as noise contributions at large delays have a disproportionate influence. The usual technique of thresholding the PDP (for noise reduction) cannot be applied in our case, since in some cases the measurement SNRs are too low for this purpose.[6] Therefore, the delay spread values obtained from the MPC parameters were deemed more reliable.

For the measured outdoor-to-indoor scenario, a cluster analysis of the MPCs has also been performed in the delay-DOA-DOD parameter space. The results are reported in [22].

# 5 Statistical Analysis

## 5.1 LOS Scenario - Fading Statistics

It is widely assumed that in LOS scenarios the channel coefficients have a *non-zero* mean complex Gaussian distribution, this results in a Rician distribution of the amplitudes. The measured channel matrix can be modeled as the weighted sum of an estimated LOS contribution (deterministic), and a residue component drawn from a *zero-mean* complex Gaussian distribution [23]

$$\begin{aligned}\mathbf{H}_{\text{model}}(m) &= \sqrt{\kappa}\mathbf{H}_{\text{LOS}}^{(n)} + \sqrt{1-\kappa}\mathbf{H}_{\text{res}}^{(n)}(m) \qquad (9)\\ &= \sqrt{\kappa}\mathbf{H}_{\text{LOS}}^{(n)} + \sqrt{1-\kappa}\cdot\text{un-vec}\left\{\mathbf{R}^{1/2}\mathbf{G}\right\}, \qquad (10)\end{aligned}$$

where $\mathbf{H}_{\text{LOS}}$ is the LOS contribution, and $\mathbf{H}_{\text{res}}(m)$ is the residue in the $m$-th realization of the channel model, the superscript $(n)$ represents the fact that the matrices are normalized as $E\left[\|\mathbf{H}\|_F^2\right] = N_R N_T$. The scalar $\kappa = \frac{K_{\text{LOS}}}{K_{\text{LOS}}+1}$, where $K_{\text{LOS}}$ is the LOS power factor defined as $K_{\text{LOS}} = \frac{\text{power in LOS component}}{\text{power in all other components}}$ (see 5.2). The full-channel correlation matrix, $\mathbf{R}$, is estimated as

$$\hat{\mathbf{R}} = \frac{1}{M}\sum_{\mathbf{m=1}}^{\mathbf{M}} \text{vec}\left\{\hat{\mathbf{H}}_{\text{res}}^{(n)}(m)\right\}\text{vec}\left\{\hat{\mathbf{H}}_{\text{res}}^{(n)}(m)\right\}^H. \qquad (11)$$

In this work, a measured scenario is treated as a LOS scenario if the strongest estimated MPC has a DOA and DOD that correspond to the hypothetical line connecting Tx antenna to Rx antenna. Note that due to this definition of the LOS, a specific antenna element need not have LOS, even though the array is defined to be in an LOS scenario. We have analyzed the validity of the modeling approach in Eq. (9) for our LOS scenarios and found that it is not well fulfilled for all our measured data. For example, the data in Fig. 9 have been taken from a LOS scenario; the top figure shows that the magnitudes of the measured channel coefficients do not

---

[6] Note that the low SNR problem is mitigated when evaluating delay spread based on the MPCs. The SAGE algorithm estimates MPC parameters including delays by maximizing a correlation function. Due to a large correlation gain accumulated over a typical number of space, time, and frequency samples employed in measurements, the wave parameters can be reliably estimated from a noisy environment. The correlation gain from our measurement parameters, 16 × 8 MIMO, 193 frequency subchannels, and 13 time snapshots is in excess of 50 dB.

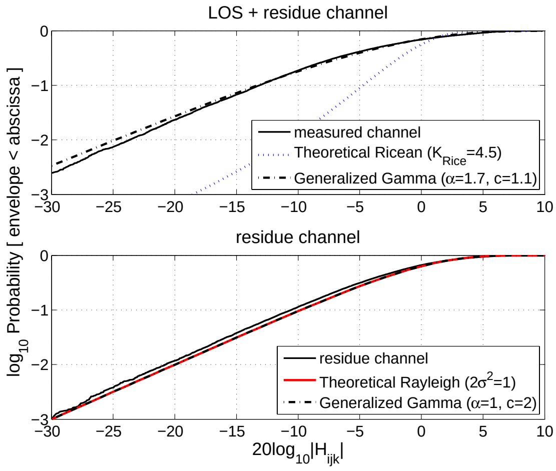

**Figure 9:** Generalized Gamma CDF fit to data distribution for position Tx1Rx2334SM. The top figure shows the measured channel, whereas the bottom figure shows the estimated residue channel. Note that in the bottom figure, the Generalized Gamma curve is traced exactly over the Rayleigh curve.

exhibit a Rician distribution, though after subtracting the estimated LOS contribution, the residue component has a Rayleigh distribution. The CDF is based on the data from a single measurement location, such that both spatial realizations and the 193 frequency sub-channels constitute the statistical ensemble. In an attempt to fit various theoretical distributions to the amplitude of the LOS data, we found that the *generalized Gamma* distribution [24], [25] best represented our measurements. The CDF of the distribution can be expressed as the *incomplete Gamma* function [26]

$$\mathrm{Prob}_{GG}\left(r < r_0\right) = P\left(\alpha, \left(\frac{r_0}{\beta}\right)^c\right), \tag{12}$$

where $P\left(\cdot\right)$ is the incomplete Gamma function, and $\alpha, \beta$, and $c$ are the distribution parameters with $\beta = \sqrt{E\left[r^2\right] \frac{\Gamma(\alpha)}{\Gamma\left(\frac{c\alpha+2}{c}\right)}}$, and $\Gamma\left(\cdot\right)$ is the Gamma function [27]. For all LOS scenarios that were analyzed, the theoretical CDF of Eq. (12) provided a good fit to the measured data with $\alpha$ in the range $1.2 - 3.5$ and $c$ in the range $0.7 - 1.6$. For the residue channel as well as NLOS scenarios, the parameter values $c = 2$, $\alpha = 1$, corresponding to a Rayleigh fading statistic [25], provide a good match to the measured data distribution.

The Generalized Gamma distribution has been used by [28] to represent a composite fading distribution. We investigated possible reasons why the fading distribution in our LOS scenarios deviated from the “standard” model, and found that some Rx elements experienced shadow fading, i.e., mean received power at the Rx elements varied considerably over the array. The shadow fading was a consequence of the absorber[7] which was part of the array construction, see Fig. 10 (a). The Fig. 10 (b) together with Fig. 11 illustrates how the absorber attenuates the LOS contribution received at the back elements of the array. Therefore, the fading distribution of the channel coefficients becomes a function of which Rx elements are considered for the ensemble. We conjecture that a similar effect would be found with a circular array of patch antennas. Thus, as an important consequence of our investigation, we find that the “standard” model of Eq. (9) is applicable for some specific receiver configurations, and the definition of, e.g., a Rice factor based on the model is meaningful. However, the model is not universally applicable, i.e., in LOS scenarios the small-scale fading statistics may not necessarily be Rician. In our case, it is shadowing due to the array configuration which causes a composite fading distribution over a small-scale area, the Rx array, and the Generalized Gamma distribution rather than the Rician is in good agreement with the measured LOS data.

---

[7] The absorber suppresses the back-lobe of the elements; this means a lower probability of locking into false and local minima in the iterative estimation procedure and hence better performance of the high-resolution algorithm.

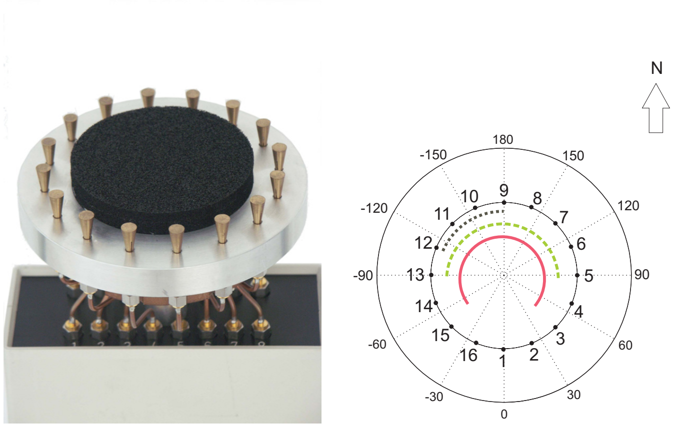

(a) (b)

**Figure 10:** (a) Rx array is a 16-element vertically polarized uniform circular array, absorber shown in the middle (b) Orientation of UCA elements with respect to angle measure 0 to 180 deg in either direction of rotation. The element numbers (1-16) are indicated along the circumference of the UCA, and the arrows relate Rx elements to corresponding CDFs in Fig. 11

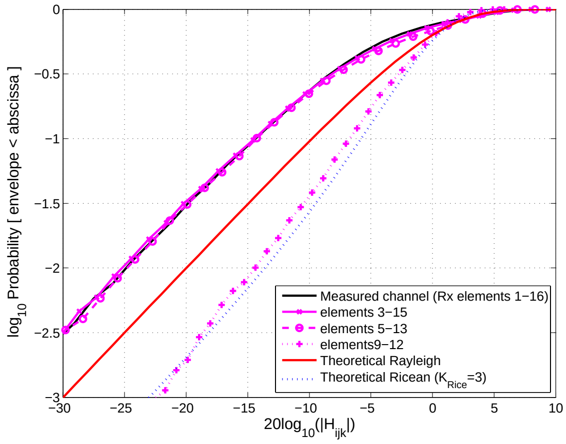

**Figure 11:** Measured channel: Effect of selecting Rx elements on the fading distribution of the channel coefficients. Position Tx2Rx2337ME

## 5.2 LOS Power Factor and Rician $K$-factor

We make a distinction between the conventional Rician $K$-factor, $K_{\mathrm{Rice}}$ and what we term the LOS-power-factor, $K_{\mathrm{LOS}}$. We define the latter as

$$K_{\mathrm{LOS}} = \frac{E\left[\left\|\hat{\mathbf{H}}_{\mathrm{LOS}}\right\|_F^2\right]}{E\left[\left\|\hat{\mathbf{H}}_{\mathrm{res}}\right\|_F^2\right]}. \tag{13}$$

It is essentially the ratio between the power in the estimated LOS component and the power in all other components. The LOS estimate, $\hat{\mathbf{H}}_{\mathrm{LOS}}$, can be extracted from a high resolution algorithm, such as SAGE, by inserting channel parameters of the LOS path into the signal model assumed by the algorithm. Note that matrices with un-normalized power are used in calculating $K_{\mathrm{LOS}}$.

It should be stressed that $K_{\mathrm{LOS}}$ is different from $K_{\mathrm{Rice}}$; the LOS power factor relates physically to the LOS component, which is strong, but not necessarily the only strong component present in the measured scenario. Still, it can be uniquely identified in a MIMO scenario by its DOA, and DOD (they have to agree with the angles that correspond to the “direct line” between Tx and Rx antennas). On the other hand, $K_{\mathrm{Rice}}$ is a characteristic parameter of the Rician amplitude distribution. It is conventionally related to the *narrowband* amplitude distribution; even when it is used to describe the amplitude characteristics of the first delay bin, it does not have a strict correspondence to the LOS component. The Rician K-factors can be extracted, e.g., with the method-of-moments as suggested by Greenstein et al. [29]. Table 2 compares the estimated values of $K_{\mathrm{Rice}}$ and $K_{\mathrm{LOS}}$ in some of our measured locations. A fair comparison between the two parameters requires that the fading distribution in question is Rician, as it would only then be meaningful to talk of a Rician $K$-factor. To avoid the absorber effect discussed in Sec. 5.1, we selected a subset of 4 consecutive Rx elements at each measurement location (column 2 in Table 2). The selected elements for each measurement position form an arc, which contains the DOA of the respective LOS MPC. The results shown in Table 2 indicate a general trend that the LOS power factor is different from $K_{\mathrm{Rice}}$. Furthermore, we propose to use $K_{\mathrm{LOS}}$ rather than $K_{\mathrm{Rice}}$ in modeling LOS scenarios as in Eq. (9). The relative performance of the two metrics in modeling a LOS scenario is discussed further in Sec. 5.3, refer Fig. 14.

## 5.3 Inter-Connection Between DOAs and DODs

As a third topic of our investigation, we analyze the coupling between the DOAs and DODs. In Fig. 12 the joint DOA-DOD spectrum is shown for one Rx position corresponding to Tx position 1. The plot shows that the joint DOA-DOD spectrum is not separable into the marginal angular spectra. To quantify this effect, we investigate three analytical channel models that make different assumptions about the coupling between DOAs and DODs. All three models share the common assumption that the channel matrix has *zero-mean* complex Gaussian entries. For analyzing the LOS

**Table 2:** Comparison of LOS power factor and Ricean $K$-factor in a Ricean channel.

| Position | Rx elements | $K_{\mathrm{LOS}}$ | $K_{\mathrm{Rice}}$ |
|---|---|---|---|
| Tx1 Rx2334MM | 8-11 | 2.5 | 4.3 |
| Tx1 Rx2334SM | 8-11 | 1.6 | 2.4 |
| Tx1 Rx2337NM | 7-10 | 1.9 | 2.6 |
| Tx2 Rx2337ME | 9-12 | 2.8 | 3.0 |
| Tx2 Rx2336NM | 7-10 | 2.2 | 2.1 |

scenarios, we consider only a subset of the full LOS channel matrix, i.e., those rows in the matrix that correspond to Rx elements which receive the LOS component free from absorber effect. The analysis in Sec. 5.1 and 5.2 guarantees that the subset channel has Rician fading. We then model this subset channel according to Eq. (9), where only $\mathbf{H}_{\mathrm{res}}$ is modeled by the zero-mean Gaussian models. For NLOS scenarios, no such limitation exists and we can test the model validity for larger channel matrices.

### Kronecker model

The Kronecker model [13] [6] approximates the full channel correlation matrix, $\mathbf{R}$, by the Kronecker product of the transmit and receive antenna correlation matrices; $\mathbf{R}_{\mathrm{Tx}}$ and $\mathbf{R}_{\mathrm{Rx}}$ respectively. Equivalently, the MIMO channel matrix is modeled as

$$\mathbf{H}_{\mathrm{Kron}} = \frac{1}{\sqrt{tr\{\hat{\mathbf{R}}_{\mathrm{Rx}}\}}} \hat{\mathbf{R}}_{\mathrm{Rx}}^{\frac{1}{2}} \mathbf{G} \hat{\mathbf{R}}_{\mathrm{Tx}}^{\frac{T}{2}}. \tag{14}$$

The Kronecker model assumes that the DOA spectrum, and hence the structure of the Rx correlation matrix does not change for different DODs.[8] In the context of Fig. 12, the Kronecker assumption when fulfilled would imply a rectangular structure, i.e., if one groups estimated DODs into narrow angular bins, where each bin results in a set of DOAs and path powers according to Eq. (1), the Kronecker assumption is considered fulfilled if the DOA power spectrum for each of the DOD bins is similar. We have analyzed the validity of the Kronecker model both for LOS and NLOS scenarios. Fig. 13 shows the modeled ergodic capacity plotted against the measured one for a number of measurement locations. In the top-figure, a $2 \times 8$ LOS setup, the Kronecker model deviates only very little from the measured results. This nice fit is due to the small rank of the channel matrix [30]. The bottom half of Fig. 13 is a $16 \times 8$ NLOS setup. This setup shows large deviations between the modeled and measured capacity due to the Kronecker assumption about the joint DOA-DOD spectrum. In [7] it is suggested that the Kronecker model, in general, underestimates the channel capacity. This is validated for the outdoor-to-indoor scenario by our results.

---

[8] However, the total power in the spectrum, a scale factor for the correlation matrix, is allowed to change.

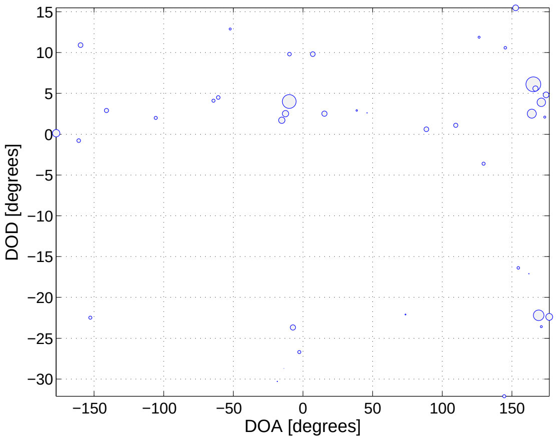

**Figure 12:** Joint DOA DOD plot for Rx position Tx1Rx2345SM. The marker diameter is scaled according to the power of each MPC, relative to the power of the strongest component [dB scale].

Note that LOS locations considered in Fig. 13 have a measured SNR in the range of 14–20 dB. When computing ergodic capacity at those locations, evaluation SNR in the capacity formula was always set to 10 dB below the corresponding measured value. In previous work [12] that analyzes the impact of measurement noise on capacity, it was established that even for a "keyhole" MIMO channel (in which the capacity is very sensitive to measurement noise) the capacity is correct as long as the measurement SNR is 10 dB better than the evaluation SNR. Thus our reported results are not influenced by measurement noise. For NLOS scenarios considered in Fig. 13, the measurement SNR was in a considerably lower range of 1-13 dB. However, we mitigated measurement noise at each location by coherently averaging channel matrices over the available 13 time snapshots; this improves measurement SNR by a factor exceeding 10 dB. For capacity evaluation we always use the noise-suppressed channel matrices and set evaluation-SNR in the capacity formula to the unprocessed value of measured SNR so that we have a 10 dB difference between measured and evaluation SNR. Therefore, our NLOS capacity results also represent the true channel capacity.

## Virtual Channel Representation

The virtual channel representation (VCR) was introduced in [31] for a ULA at each link end, and allows arbitrary coupling between pre-determined directions at the Tx and Rx sides. The model uses discrete Fourier transform matrices $\mathbf{A}_{\mathrm{Rx}}$ and $\mathbf{A}_{\mathrm{Tx}}$ at respective link ends, such that the measured channel and the virtual channel are unitarily equivalent. The realizations of the channel model can be generated as

$$\mathbf{H}_{\mathrm{VCR}} = \mathbf{A}_{\mathrm{Rx}} \left( \tilde{\mathbf{\Omega}} \odot \mathbf{G} \right) \mathbf{A}_{\mathrm{Tx}}^{T}. \tag{15}$$

The columns of $\mathbf{A}_{\mathrm{Rx}}$ and $\mathbf{A}_{\mathrm{Tx}}$are based on the array response (steering) vectors computed at fixed virtual directions, and the matrix $\tilde{\mathbf{\Omega}}$ is the element-wise square root of the power coupling matrix $\mathbf{\Omega}$; the entry $\mathbf{\Omega}_{ij}$ gives the average power coupled between the $i$-th receive and $j$-th transmit direction. This beamforming approach thus incorporates the antenna array effects. However, since the directions are pre-determined and scatterers within the spatial resolution of the array will not be resolved, it is possible that the true spatial characteristics of the channel will not be rendered accurately for some scenarios.

In our measurement setup, the Rx array was not a ULA, but rather a UCA with an absorber in the center. We thus use a generalization of Eq. (15) that combines the standard (virtual channel model) at the Tx side, with a “canonical” representation, based on the channel statistics, at the Rx side

$$\mathbf{H}_{\mathrm{VCR}} = \hat{\mathbf{U}}_{\mathrm{Rx}} \left( \tilde{\mathbf{\Omega}} \odot \mathbf{G} \right) \mathbf{A}_{\mathrm{Tx}}^{T},$$

where $\hat{\mathbf{U}}_{\mathrm{Rx}}$ is an estimate of the receive eigenvector matrix obtained by eigenvalue decomposition of $\hat{\mathbf{R}}_{\mathrm{Rx}}$. In Fig. 13 the ergodic capacities computed from this model are also shown. For the 16 × 8 NLOS setup, the capacity from this model tends to slightly over-estimate the measured values.

### Weichselberger Model

Like the Kronecker model, the Weichselberger model [7] represents the measured channel in the eigenvector domain, though unlike the Kronecker model, it strives to model channel correlations jointly at both link ends. This is achieved by defining a power coupling matrix between the eigenvectors of the two link ends. The Weichselberger model assumes that the eigenvector matrix at the Rx is independent of which spatial Tx weight vector, i.e., DOD is considered. However, the corresponding eigenvalues of the spatial correlation matrix at Rx can differ for different DOD. The same argument applies to the reverse link. The physical interpretation of the modeling assumptions can be found in [7] wherein the channel is modeled as

$$\hat{\mathbf{H}}_{\mathrm{weichsel}} = \hat{\mathbf{U}}_{\mathrm{Rx}} \left( \tilde{\mathbf{\Omega}} \odot \mathbf{G} \right) \hat{\mathbf{U}}_{\mathrm{Tx}}^{T}, \tag{16}$$

where $\hat{\mathbf{U}}_{\mathrm{Rx}}$ and $\hat{\mathbf{U}}_{\mathrm{Tx}}$ are estimates of receive and transmit eigenvector matrices, obtained by eigenvalue decomposition of $\hat{\mathbf{R}}_{\mathrm{Rx}}$ and $\hat{\mathbf{R}}_{\mathrm{Tx}}$ respectively. The elements of the power coupling matrix $\mathbf{\Omega}_{ij}$ now give the average power coupled between the $i$-th receive and $j$-th transmit eigenvector; the matrix is estimated as

$$\hat{\mathbf{\Omega}} = \frac{1}{M} \sum_{m=1}^{M} \left[ \mathbf{K} \odot \mathbf{K}^{*} \right], \tag{17}$$

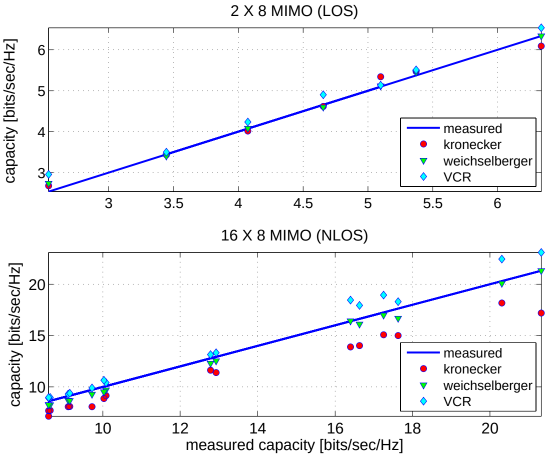

**Figure 13:** Scatter plot of average modeled capacity against average measured capacity of the channel. Top figure is for LOS 2X8 MIMO, bottom figure is for NLOS 16X8 MIMO. The identity line indicates points of no modelling error.

where $\mathbf{K} = \left(\hat{\mathbf{U}}_{\mathrm{Rx}}^{H}\mathbf{H}\left(m\right)\hat{\mathbf{U}}_{\mathrm{Tx}}^{*}\right)$, and $\mathbf{H}\left(m\right)$ is the $m-$th channel realizaton. It should be noted that the Kronecker model is a special case of the Weichselberger model. In Fig. 13 the ergodic capacity computed from the Weichselberger model is shown for the same measurement locations as for previous cases. Compared to the Kronecker model, the Weichselberger model provides a better fit to the measured data. This result is expected from Fig. 12, where the joint spectrum is not separable into the marginal spectra. The Weichselberger models fits measured data better than the VCR case as well. This can be explained because in the former case, the channel statistics determine the unitary matrices at *both* link ends. Our results, obtained for the outdoor-to-indoor scenario, are consistent with the observations in [7] which considered the pure indoor and outdoor cases separately. As a follow-up to Sec. 5.2, we use the Weichselberger model and the ergodic capacity as a metric to compare performance of $K_{\mathrm{Rice}}$ and $K_{\mathrm{LOS}}$ in modelling a LOS scenario according to Eq. (9). The plots are shown in Fig. 14 for a $2 \times 8$ LOS setup. Though, the restriction to use a small rank LOS channel will result in a convergence of performance of the two metrics, from the figure the $K_{\mathrm{LOS}}$ metric appears to perform better.

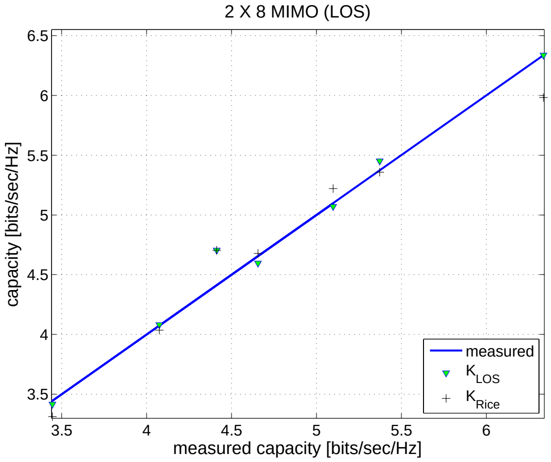

**Figure 14:** Performance comparison of $K_{\mathrm{LOS}}$ and $K_{\mathrm{Rice}}$ in modelling an LOS scenario. The Weichselberger model is used in both cases.

# 6 Conclusions

In this paper we have presented the results of a double-directional measurement campaign for an outdoor-to-indoor office scenario. Our characterization of the outdoor-to-indoor scenario indicates that the angular dispersion at the outdoor link end is rather small, the mean direction-spread is in the range $0.09 - 0.24$. At the indoor link end, MPCs of significant energy arrive from all directions and consequently the angular dispersion is much larger, we observed mean direction-spreads in the range $0.69 - 0.82$. The delay spread was measured to be in the range of $5 - 25$ ns. By considering 40 MPC at each measured position, more than 85% of the received power could be accounted for in 60% of the 159 measurement locations.

Our statistical analysis shows that the widely used assumption in MIMO channel modeling, that the channel can be represented as a sum of a weighted LOS component plus a zero-mean complex Gaussian distribution may not adequately represent measured data; in general the small-scale fading in a LOS scenario may not be Rician; we observed a composite fading distribution, caused by our antenna configuration and found the Generalized Gamma distribution a useful tool for verifying this. Furthermore, we have highlighted the difference between the LOS power factor and the Rician $K$-factor, and support this assertion with measured data from a Rician fading channel. We show that the DOA spectrum depends noticeably on the DOD. Using ergodic channel capacity as a metric, we have compared the performance of the Kronecker, VCR, and Weichselberger models for the outdoor-to-indoor scenario. The Kronecker model is not applicable in our case due to the breakdown of the DOA-DOD decoupling assumptions; this holds true even for the NLOS scenarios. Compared to the VCR model, the Weichselberger model provides a better fit to the measured capacity for both LOS and NLOS scenarios.

Our results can serve as a basis for understanding outdoor-to-indoor MIMO channels, and have served as an input to the COST 273 MIMO channel model [32].

## Acknowledgment

Part of this work was financed by an INGVAR grant of the Swedish Foundation for Strategic Research, a grant from the Swedish Science Council, and the SSF inter-university Center of Excellence for High-Speed Wireless Communications. We would like to thank Prof. Larry Greenstein, Prof. Ernst Bonek, and members of the COST 273 subworking group 2.1 for fruitful discussions regarding the Rician $K$-factor. We would also like to acknowledge the informative input from Dr. Akbar Sayeed regarding the generalization of the VCR to UCAs. TU Ilmenau is kindly acknowledged for the loan of their antenna arrays.

## References

[1] J. H. Winters, “On the capacity of radio communications systems with diversity in Rayleigh fading environments,” *IEEE Journal on Selected Areas in Communications*, vol. 5, pp. 871–878, June 1987.

[2] G. J. Foschini and M. J. Gans, “On limits of wireless communications in a fading environment when using multiple antennas,” *Wireless Personal Communications: An International Journal*, vol. 6, pp. 311–335, 1998.

[3] M. Steinbauer, A. F. Molisch, and E. Bonek, “The double-directional radio channel,” *IEEE Antennas and Propagation Magazine*, vol. 43, pp. 51–63, August 2001.

[4] D. Chizhik, J. Ling, P. W. Wolniansky, R. A. Valenzuela, N. Costa, and K. Huber, “Multiple-input-multiple-output measurements and modeling in Manhattan,” *IEEE Journal on Selected Areas in Communications*, vol. 21, pp. 321–331, April 2003.

[5] R. Thomä, D. Hampicke, M. Landmann, G. Sommerkorn, and A. Richter, “MIMO measurement for double-directional channel modelling,” in *Proc. IEE Seminar on MIMO: Communications Systems from Concept to Implementations (Ref. No. 2001/175)*, pp. 1/1–1/7, December 2001.

[6] K. Yu, M. Bengtsson, B. Ottersten, D. McNamara, P. Karlsson, and M. Beach, “Second order statistics of NLOS indoor MIMO channels based on 5.2 GHz measurements,” in *Proc. IEEE Globecom 2001*, vol. 1, pp. 156–160.

[7] W. Weichselberger, M. Herdin, H. Özcelik, and E. Bonek, “A stochastic MIMO channel model with joint correlation of both link ends,” *IEEE Transactions on wireless Communications*, vol. 5, pp. 90–100, January 2006.

[8] S. Wyne, P. Almers, G. Eriksson, J. Karedal, F. Tufvesson, and A. F. Molisch, "Outdoor to indoor office MIMO measurements at 5.2 GHz," in *Proc. IEEE VTC 2004 Fall*, (Los Angeles, USA), pp. 101–105.

[9] J. Medbo, F. Harrysson, H. Asplund, and J. E. Berg, "Measurements and analysis of a MIMO macrocell outdoor-indoor scenario at 1947 MHz," in *Proc. IEEE VTC 2004-Spring*, vol. 1, pp. 261–265.

[10] H. T. Nguyen, J. B. Andersen, and G. F. Pedersen, "Characterization of the indoor/outdoor to indoor MIMO radio channel at 2.140 GHz," *Wireless Personal Communications: An International Journal*, vol. 35, pp. 289–309, November 2005.

[11] D. Gesbert, H. Blcskei, D. A. Gore, and A. J. Paulraj, "Outdoor MIMO wireless channels: models and performance prediction," *IEEE Transactions on Communications*, vol. 50, pp. 1926–1934, December 2002.

[12] P. Almers, F. Tufvesson, and A. F. Molisch, "Keyhole effect in MIMO wireless channels: Measurements and theory," *IEEE Transactions on Wireless Communications*, vol. 5, no. 12, pp. 3596–3604, 2006.

[13] J. P. Kermoal, L. Schumacher, K. I. Pedersen, P. E. Mogensen, and F. Frederiksen, "A stochastic MIMO radio channel model with experimental validation," *IEEE Journal on Selected Areas in Communications*, vol. 20, pp. 1211–1226, August 2002.

[14] H. Özcelik, N. Czink, and E. Bonek, "What makes a good MIMO channel model," in *Proc. IEEE VTC 2005 Spring*, (Stockholm, Sweden), pp. 156–160, May/June 2005.

[15] S. Wyne, A. F. Molisch, P. Almers, G. Eriksson, J. Karedal, and F. Tufvesson, "Statistical evaluation of outdoor-to-indoor office MIMO measurements at 5.2 GHz," in *Proc. IEEE VTC 2005 Spring*, (Stockholm, Sweden), pp. 146–150.

[16] MEDAV GmbH, http://www.channelsounder.de.

[17] B. H. Fleury, M. Tschudin, R. Heddergott, D. Dahlhaus, and K. Pedersen, "Channel parameter estimation in mobile radio environments using the SAGE algorithm," *IEEE Journal on Selected Areas in Communications*, vol. 17, pp. 434–450, March 1999.

[18] A. F. Molisch, *Wireless Communications*. Chichester, U.K.: Wiley, 2005.

[19] J. Medbo, M. Riback, H. Asplund, and J. Berg, "MIMO channel characteristics in a small macrocell measured at 5.25 GHz and 200 MHz bandwidth," in *Proc. IEEE VTC 2005 Fall*, vol. 1, pp. 372–376.

[20] B. H. Fleury, "First- and second-order characterization of direction dispersion and space selectivity in the radio channel," *IEEE Transactions on Information Theory*, vol. 46, pp. 2027–2044, September 2000.

[21] P. A. Bello, "Characterization of randomly time-variant linear channels," *IEEE Transactions*, pp. 360–393, December 1963.

[22] S. Wyne, N. Czink, J. Karedal, P. Almers, F. Tufvesson, and A. F. Molisch, "A cluster-based analysis of outdoor-to-indoor office MIMO measurements at 5.2 GHz," in *Proc. IEEE VTC 2006 Fall*, (Montreal, Canada).

[23] P. Soma, D. S. Baum, V. Erceg, R. Krishnamoorthy, and A. J. Paulraj, "Analysis and modeling of multiple-input multiple-output (MIMO) radio channel based on outdoor measurements conducted at 2.5 GHz for fixed BWA applications," in *Proc. IEEE ICC 2002*, vol. 1, pp. 272–276.

[24] E. W. Stacy, "A generalisation of the Gamma function," *Annals of Mathematical Statistics*, vol. 33, pp. 1187–1192, 1962.

[25] J. Griffiths and J. McGeehan, "Interrelationship between some statistical distributions used in radio wave propagation," in *IEE Proc.*, vol. 129 part F, pp. 411–417, IEE, December 1982.

[26] R. Vaughan and J. B. Andersen, *Channels, Propagation and Antennas for Mobile Communications*. London, U.K.: IEE, 1st ed., 2003.

[27] M. Abramowitz and I. Stegun, *Handbook of Mathematical Functions*. Dover, 1966.

[28] A. J. Coulson, A. G. Williamson, and R. G. Vaughan, "Improved fading distribution for mobile radio," in *IEE Proc. - Communications*, vol. 145, pp. 197–202, IEE, June 1998.

[29] L. J. Greenstein, D. G. Michelson, and V. Erceg, "Moment-method estimation of the Ricean K-factor," *IEEE Communications Letters*, vol. 3, pp. 175–176, June 1999.

[30] M. A. Jensen and J. Wallace, "A review of antennas and propagation for MIMO wireless communications," *IEEE Transactions on Antennas and Propagation*, vol. 52, pp. 2810–2824, November 2004.

[31] A. M. Sayeed, "Deconstructing multiantenna fading channels," *IEEE Transactions on Signal processing*, vol. 50, pp. 2563–2579, October 2002.

[32] L. Correia, ed., *COST 273 final report: Towards mobile broadband multimedia networks*. Amsterdam, The Netherlands: Elsevier, 2006.

# *Paper II*

# A Cluster-based Analysis of Outdoor-to-Indoor Office MIMO Measurements at 5.2 GHz

## Abstract

In this paper, we present a cluster based analysis of an outdoor-to-indoor Multiple-Input Multiple-Output (MIMO) measurement campaign, and extract model parameters for the COST273 channel model. The measurements were performed at 5.2 GHz for 159 measurement locations in an office building. Multipath component (MPC) parameters have been extracted for these positions using a high-resolution algorithm. We analyze the clustering of MPCs, i.e., grouping together of MPCs with similar DOAs, DODs, and delays. We compare cluster identification by visual inspection to automatic identification by the recently proposed algorithm of Czink et al. In the paper we include results on the intercluster properties such as the distribution of the number of clusters and the cluster powers, as well as intracluster properties such as the angle and delay spreads within the clusters. In particular, we extract parameters for the COST 273 channel model, a standardized generic model for MIMO propagation channels.

---

S. Wyne, N. Czink, J. Karedal, P. Almers, F. Tufvesson, and A. F. Molisch,
“A Cluster-based Analysis of Outdoor-to-Indoor Office MIMO
Measurements at 5.2 GHz,”
in Proc. *IEEE Vehicular Technology Conference (VTC-2006 Fall)*, Montreal , Canada,
vol. 1, pp. 22-26, September 2006.

# 1 Introduction

Multiple antennas at both receiver and transmitter can result in tremendous capacity improvements compared to single antenna systems. Ultimately, the capacity gains depend on the propagation channel in which the system is operating. The establishment of good channel models is therefore essential both for the development of new algorithms for signal processing, modulation and coding, and for the unified testing of different system proposals. A number of standardized channel models have been developed for the testing of specific systems, e.g., the 3GPP model for outdoor cellular communications [1] and the 802.11n model for indoor wireless LANs [2]. However, those models do not cover some important scenarios, especially the case where the base station is outdoors, and the mobile station is indoors. In recent conference contributions [3] [4], we presented measurement results for the outdoor-to-indoor case and presented some typical parameters like total rms angular spread. In the current paper, we use those measurements to derive a subset of the COST 273 model parameters that can be implemented for system testing.

In measured MIMO propagation channels the MPCs tend to occur in clusters, i.e., groups of MPCs with similar parameters, delay, direction of arrival (DOA), and direction of departure (DOD) [5], [6]. It is important that channel models correctly reflect this clustering property [7]. For example, the results in [8], indicate that channel models disregarding clustering effects overestimate capacity. Furthermore, from an aspect of system-level testing, it is convenient to model the propagation channel in terms of cluster properties rather than modeling the behavior of individual MPCs. It is for these reasons that clustering in MIMO propagation channels is actively researched, e.g., [6] [9] [10], and also included in many channel models. In particular, the European COST 273 [11] action has developed a general MIMO channel model that describes parameters for the MPC clusters occurring in the propagation channel. This description can be broadly categorized as *intercluster* and *intracluster* parameters which characterize the clusters and MPCs within clusters, respectively. The model is general enough to allow description of many different scenarios, e.g., cellular, WLAN, fixed wireless, and peer-to-peer communications.

In this paper we establish a set of parameters, for the clustered stochastic MIMO channel model for the outdoor-to-indoor case. The parameters are based on the COST 273 generic channel model and fitted with the results from our measurements. Though the COST 273 model is applicable both to time-variant and static channels, in this paper we characterize a static environment only. For that goal, we first perform a cluster identification; using both visual inspection and an automatic clustering algorithm [12]. In the remainder of the paper we include detailed results on the intercluster and intracluster properties, including cluster power distributions, and intracluster delay spreads and angular spreads.

## 2 Measurement setup

The measurement setup is described in detail in [3] and summarized here for the convenience of the reader. Measurement data were recorded with the RUSK ATM channel sounder. The measurements were performed at a center frequency of 5.2 GHz and a signal bandwidth of 120 MHz. The transmit antenna was an 8 element dual polarized uniform linear patch array and the receive antenna was a 16-element uniform circular array with vertically polarized monopole elements. The channel was seen to be static and this was confirmed by the measurements.

We have extracted MPC parameters for the 159 measurement positions using the high-resolution RIMAX algorithm [13]. At each measurement position we have extracted the parameters delay, DOA, DOD, and complex path-weights for up to 50 MPCs. It must be stressed that high-resolution algorithms based on the sum-of-plane-waves model cannot explain all possible propagation processes, especially not in the indoor environment where the receive antenna sometimes was located close to some scatterers. However, the RIMAX algorithm estimates the parameters for the diffuse scattering component of the measured channel. The path parameters, DOA, DOD, and delay were cross-checked at a number of positions with the geometry of the measurement site, and provided a good match.

## 3 Comparison of Clustering Approaches

Clustering of MPCs, i.e., identification of MPCs that have similar parameters, is conventionally performed by visual inspection, e.g., [10], [14], [15]. To utilize the large data set from our 159 measurement locations, we have performed clustering with an automated algorithm proposed in [12]. For selected measurement locations, we also performed a *visual cluster identification* by a *joint-inspection* of parameter extraction results. The delay, DOA azimuth and DOD azimuth domains were jointly employed for clustering in both methods. Note that our cluster analysis is based on plane waves only and disregards the diffuse contributions.

For the visual inspection, a cluster was *identified* as a set of MPCs with similar delay, DOA, and DOD parameters - note that we require that *all* of the parameters must be similar in order for the MPCs to form a cluster. We also investigated the physical propagation mechanisms of the MPCs (e.g., reflections via specific objects), and required that MPCs belonging to a cluster should have the same physical propagation mechanisms. To avoid a bias by the observer, the clustering by visual inspection was performed $before$ automated clustering results were available. For the automated cluster identification, which was performed for *all* measurement locations, we *defined* clusters based on a power-weighted "multipath component distance" metric as defined in [12], [16]. Since powers of the extracted MPCs exhibit a large dynamic range, we limited our analysis to MPCs with powers within 30 dB of the strongest component. The weaker components have negligible influence on the calculation of statistical spreads but would introduce inaccuracies when calculating probability density functions such as for the number of clusters and number of MPCs

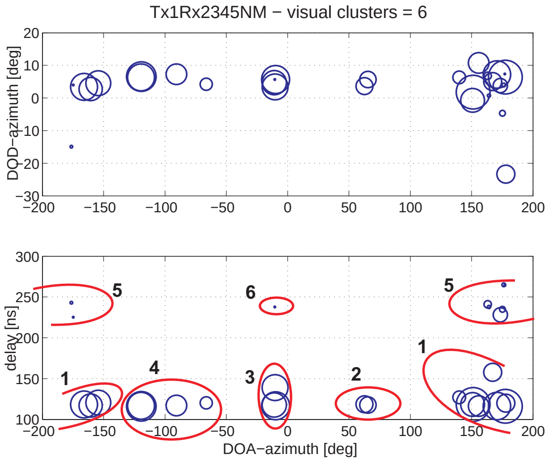

**Figure 1:** Clusters identified by visual inspection at location Tx1Rx2345NM [3]. Circle diameters are scaled to relative powers of MPCs. Clusters 1 and 5 represent energy coming through the door, which opens into the office corridor. Clusters 4 (West wall) and 2 (East wall) represent reflections from metal objects on wall-racks. Clusters 3 and 6 are due to reflections from metal pipes of heater/ window handles along South wall. Clusters 5 and 6 are delayed from their earlier arriving counterparts, due to multiple reflection between the two buildings where Tx and Rx are placed.

per cluster.

The clustering for one measurement location is compared in Fig. 1 (visual) and Fig. 2 (algorithm). The clusters defined by the algorithm appear in reasonable agreement with the visually identified clusters. The algorithm defines three separate clusters for the MPCs otherwise identified as cluster 1 by visual inspection, similarly cluster 4 from visual identification is defined as two adjacent clusters. To compare the two clustering approaches, for all locations where visual inspection was performed, the respective CDFs for the intracluster spreads for delay, DOA and DOD are plotted in Figs. 3, 4, and 5. Note that for comparing the two clustering methods only a statistical measure, a CDF of the spreads, is employed because our final objective is to characterize the channel with statistical parameters rather than describe physical propagation. Based on the CDFs of the intracluster spreads, the two clustering approaches are in good agreement. The results in the remainder of the paper are based on automated clustering only.

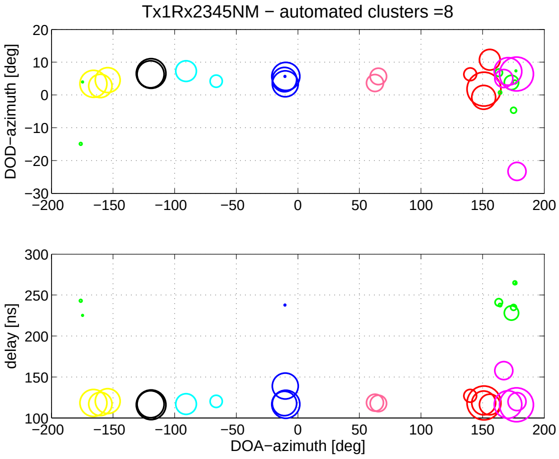

**Figure 2:** Clusters defined by the algorithm at location Tx1Rx2345NM. The MPCs are color coded to indicate cluster association.

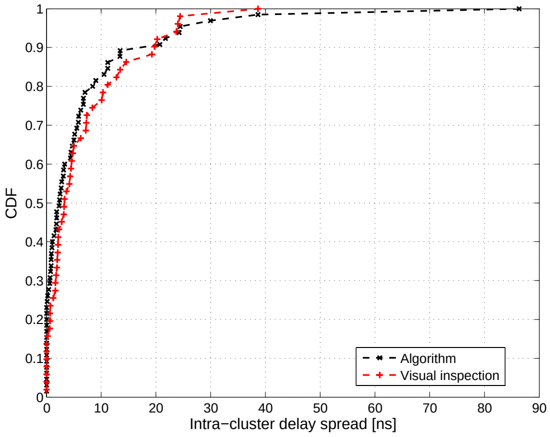

**Figure 3:** Algorithm vs. visual inspection, comparison of CDFs of intra-cluster delay spread.

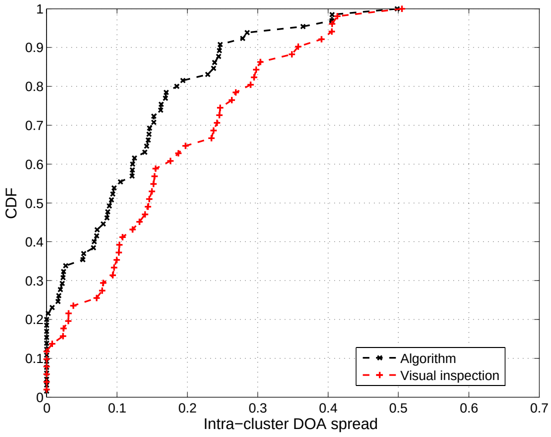

**Figure 4:** Algorithm vs. visual inspection, comparison of CDFs of intra-cluster DOA spread.

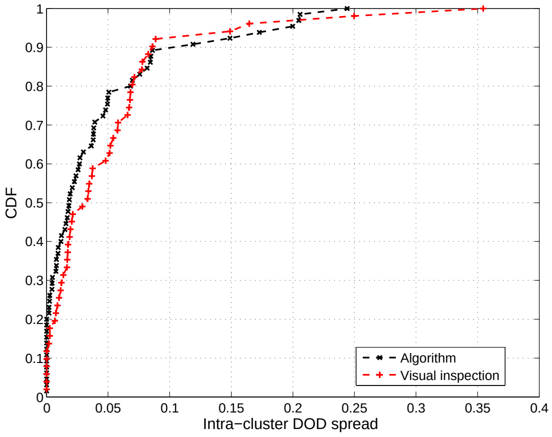

**Figure 5:** Algorithm vs. visual inspection, comparison of CDFs of intra-cluster DOD spread.

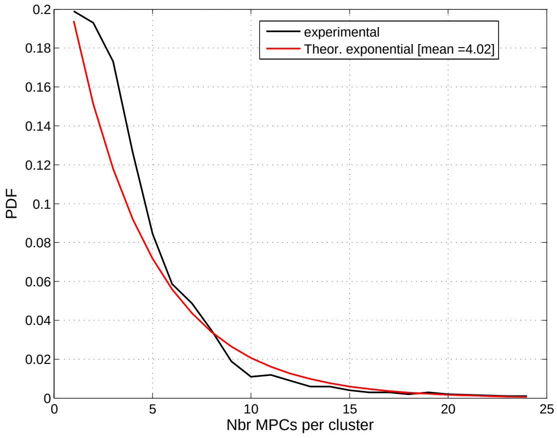

**Figure 6:** Distribution of number of MPCs in a cluster.

# 4 Results

The clustering algorithm[9] was applied to all 159 measurement locations and a total of 1005 clusters were extracted. These form the statistical ensemble for the statistical analysis reported in this section. The results have been categorized as intra- and intercluster properties.

## 4.1 Intra-cluster properties

The distribution of the number of MPCs per cluster is plotted in Fig. 6. The median number of MPCs is 3 whereas the mean is 4.02. An Exponential distribution with the indicated mean provides a good fit to the empirical pdf. The distribution of the intracluster delay spread is plotted in Fig. 7. The spread[10] is calculated as the conventional rms delay spread [5], of MPCs within a cluster. Note that the apparently large occurence of spreads around 150 ns is due to the fact that isolated occurences of the delay spread, in excess of 150 ns, have been collected into this

---

[9] A delay-scaling factor of 5 was used to assign more significance to delay during clustering. The Cluster-pruning feature of the algorith was not used owing to the upper limit of 50 MPCs extracted per position by RIMAX and a further 30 dB power limit on MPCs to be considered for cluster analysis.

[10] The delay spread model of COST 273 is distance-dependent, i.e., the delay spread is the product of $d^{-0.5}$ times the lognormal variable, where $d$ is the Tx-Rx distance. However, we omit this scaling in our analysis because the distance variation in our measurements, between nearest and farthest Rx location relative to Tx, never exceeds a factor of 2.

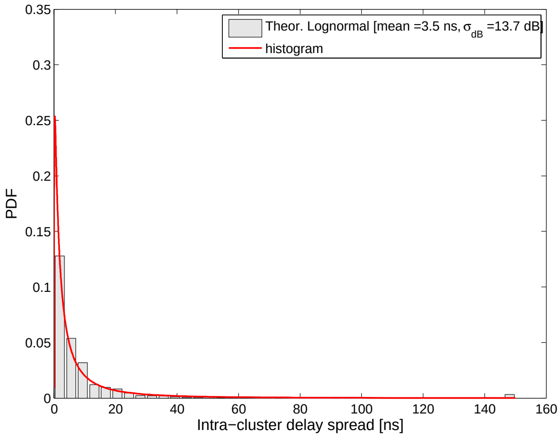

**Figure 7:** Distribution of delay spread within a cluster.

single bin. According to the COST 273 model, a Lognormal pdf has been fitted to all intracluster spreads. For the delay spread, a mean of 3.5 ns and standard deviation of 13.7 dB provides a reasonable fit to the histogram. The distribution of the spreads in direction of arrival and departure, azimuth only, are plotted in Figs. 8 and 9. To avoid the ambiguity caused by the origin of the coordinate system, the Fleury definition [17] is used to calculate the spreads[11]. Note that in Figs. 7, 8, and 9 the singletone[12] clusters, which by definition have zero spread, are not plotted. A total of 200 out of the 1005 clusters were observed to be singletone clusters. For the DOA spread, a Lognormal pdf with mean 0.08 and deviation 10.5 dB has been fitted to the empirical PDF. For the DOD spread, a Lognormal with a mean of 0.02 and deviation of 12.3 dB fits our empirical results.

## 4.2 Inter-cluster properties

The distribution of the number of clusters at each measurement location is plotted in Fig. 10. The horizontal axis begins at 3 since at each measurement location, this is the lower limit of the range of possible number of clusters from which the algorithm selects the optimum cluster set. According to the COST 273 model, the total number of clusters is $N_{C_{\min}} + X$, where $N_{C_{\min}}$ is the minimum number of clusters occuring at each position (3 in our case) and $X$ is a random variable with Poisson

---

[11] The Fleury definition of direction spread can, for small values, be used as the angular spread in units of radians.

[12] Clusters consisting of a single MPC

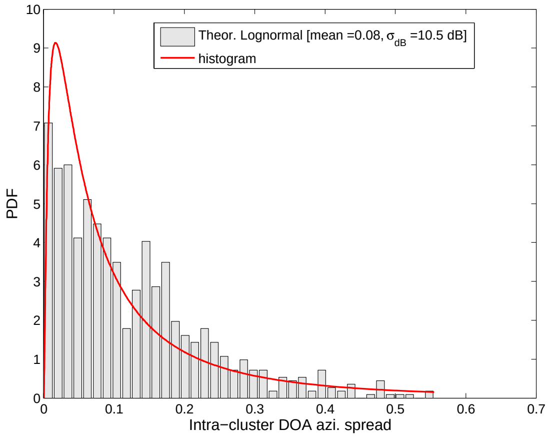

**Figure 8:** Distribution of the DOA spread within a cluster.

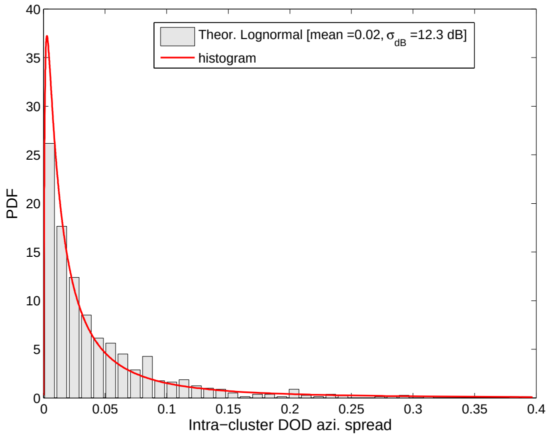

**Figure 9:** Distribution of DOD spread within a cluster.

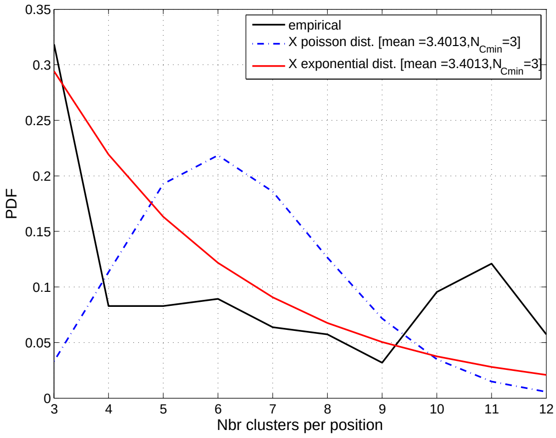

**Figure 10:** Distribution of the number of clusters.

distribution. Though, this functional relation does not describe our measurements well, and choosing $X$ as Exponential distributed seems to fit better. The mean number of clusters was found to be 6.4 while the median value was 6. The distribution of the minimum delays of the clusters, i.e., first-arriving component of each cluster is plotted in Fig. 11. The occurence of minimum delay values in excess of 400 ns is due to singletone clusters ocurring at this delay. A Lognormal distribution with mean 106 ns and deviation 4.4 dB was found to fit the empirical data. Due to space constraints in the paper, we omit our results on the distributions of the mean angle of arrival and departure. These results, together with the correlations between the cluster spreads and the cluster powers, will be discussed in a follow-up publication. In Fig. 12 the normalized cluster powers are plotted as a function of the excess minimum delays of the clusters, i.e., cluster delays relative to minimum delay of the first arriving cluster at the respective measurement location. The cluster powers are normalized by the power of the same cluster. Thus we are able to compare clusters from different measurement locations. The solid line in Fig. 12 is the linear regression of the cluster powers in dB on the excess minimum delays of the clusters, and indicates addittional attenuation depending on excess delays of the clusters. An attenuation coefficient of 25 dB/$\mu$s is observed from this plot. Note that we do not use a cut-off delay in plotting Fig. 12 because we have some late arriving clusters with strong powers. The deviation of the cluster powers from the linear regression is a measure of the cluster power shadow fading. In Fig. 13 an empirical PDF of the deviation is plotted together with a Gaussian fit with zero-mean and standard deviation of 9 dB. In Figs. 12 and 13 the first arriving clusters at each location, which have been used for normalization, are not plotted; these clusters would have

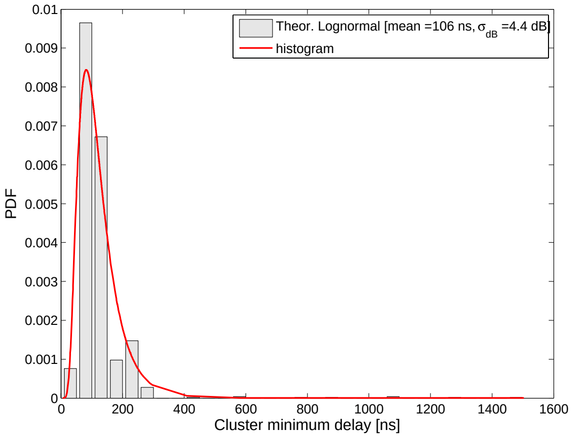

**Figure 11:** Distribution of the minimum delay of the clusters.

coordinates $(0, 0)$ in Fig. 12 and would appear as a large peak around 0 in Fig. 13.

# 5 Summary

We have performed a statistical analysis of MPC clusters observed in our measurements at 159 locations in an outdoor-to-indoor office scenario. We extracted a subset of the model parameters of the COST273 channel model, valid for this scenario. For the intracluster properties, the number of MPCs per cluster was observed to be Exponentially distributed, the intra-cluster spreads followed a Lognormal distribution. For the intercluster properties, the distribution of number of clusters was better fit by an Exponential rather than the Poisson distribution specified in the model. The cluster delay was observed to follow a Lognormal distribution. The cluster attenuation coefficient was measured to be 25 dB/$\mu$s.

# Acknowledgment

We would like to thank Markus Landmann for useful inputs and TU Ilmenau for providing the antennas used in measurements. Part of this work was financed by an INGVAR grant of the Swedish Foundation for Strategic Research and a grant from the Swedish Science Council. This work was partly conducted within the EC-funded Network-of-Excellence NEWCOM.

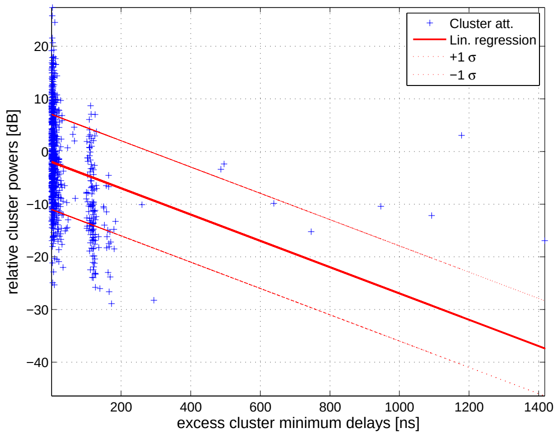

**Figure 12:** Attenuation of cluster powers as a function of excess delay.

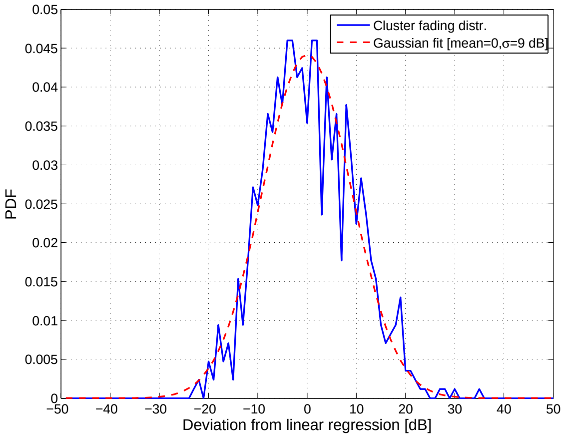

**Figure 13:** Distribution of cluster shadow fading, and a zero-mean Gaussian fit.

# References

[1] 3GPP - 3GPP2 Spatial Channel Model Ad-hoc Group, "Spatial channel model for MIMO systems," tech. rep., 3GPP and 3GPP2; download at http://www.3gpp.org, 2003.

[2] A. K. Jagannatham and V. Erceg, "MIMO indoor WLAN channel measurements and parameter modeling at 5.25 GHz," in *Proc. IEEE VTC 2004 Fall*, vol. 1, pp. 106–110, September 2004.

[3] S. Wyne, P. Almers, G. Eriksson, J. Karedal, F. Tufvesson, and A. F. Molisch, "Outdoor to indoor office MIMO measurements at 5.2 GHz," in *Proc. IEEE VTC 2004 Fall*, (Los Angeles, USA), pp. 101–105.

[4] S. Wyne, A. F. Molisch, P. Almers, G. Eriksson, J. Karedal, and F. Tufvesson, "Statistical evaluation of outdoor-to-indoor office MIMO measurements at 5.2 GHz," in *Proc. IEEE VTC 2005 Spring*, (Stockholm, Sweden), pp. 146–150.

[5] A. Saleh and R. A. Valenzuela, "A statistical model for indoor multipath propagation," *IEEE J. Selected Areas Comm.*, vol. 5, pp. 128–137, February 1987.

[6] J. Fuhl, A. F. Molisch, and E. Bonek, "Unified channel model for mobile radio systems with smart antennas," in *Proc. IEE Radar, Sonar and Navigation*, vol. 145, pp. 32–41, February 1998.

[7] A. F. Molisch, "Effect of far scatterer clusters in MIMO outdoor channel models," in *Proc. IEEE VTC 2003 Spring*, (South Korea), pp. 534–538, April 2003.

[8] K. Li, M. Ingram, and A. V. Nguyen, "Impact of clustering in statistical indoor propagation models on link capacity," *IEEE Transactions on Communications*, vol. 50, pp. 521–523, April 2002.

[9] M. Steinbauer and A. F. Molisch(eds.), "Directional channel models," in *Wireless Flexible Personalized Communications* (L. Correia, ed.), ch. 3.2, pp. 132–193, Wiley, 2001.

[10] L. Vuokko, P. Vainikainen, and J. Takada, "Clusters extracted from measured propagation channels in macrocellular environments," *IEEE Transactions on Antennas and Propagation*, vol. 53, pp. 4089–4098, December 2005.

[11] L. Correia, ed., *COST 273 final report: Towards mobile broadband multimedia networks*. Amsterdam, The Netherlands: Elsevier, 2006.

[12] N. Czink, P. Cera, J. Salo, E. Bonek, J.-P. Nuutinen, and J. Ylitalo, "A framework for automatic clustering of parametric MIMO channel data including path powers," in *Proc. IEEE Vehicular Technology Conference (VTC-2006 Fall)*, (Montreal, Canada), September 2006.

[13] A. Richter, *Estimation of Radio Channel Parameters: Models and Algorithms*. PhD thesis, Ilmenau Technical University, Germany, 2005.

[14] N. Czink, X. Yin, E. Bonek, and B. Fleury, "Cluster angular spreads in a MIMO indoor propagation environment," in *PIMRC'05*, (Berlin, Germany), 2005.

[15] M. Toeltsch, J. Laurila, K. Kalliola, A. F. Molisch, P. Vainikainen, and E. Bonek, "Statistical characterization of urban spatial radio channels," *IEEE Journal on Selected Areas in Communications*, vol. 20, pp. 539–549, April 2002.

[16] M. Steinbauer, H. Özcelik, H. Hofstetter, C. F. Mecklenbräuker, and E. Bonek, "How to quantify multipath separation," *IEICE Trans. Electron.*, vol. E85-C, pp. 552–557, March 2002.

[17] B. H. Fleury, "First- and second-order characterization of direction dispersion and space selectivity in the radio channel," *IEEE Transactions on Information Theory*, vol. 46, pp. 2027–2044, September 2000.

# *Paper III*

# A Statistical Model for Indoor Office Wireless Sensor Channels

## Abstract

Sensor networks and Ad-hoc networks, where nodes inter-communicate without fixed infrastructure, have recently attracted interest due to potential use in industrial, environmental, and safety-related applications. The fading statistics of the propagation channels between sensor nodes are essential to determine the possible data rate, outage, and latency of sensor networks. This paper presents (to the best of our knowledge) the first in-depth analysis, based on measurements, of the propagation channels between typical sensor node locations in office environments. We find that the amplitude fading distribution can be characterized as Ricean. The Rice factor is analyzed as a function of distance and it is determined that it is *not* a monotonically decreasing function. Even in pure LOS situations, Rice factors show a random behavior and are on the order of 10 or less. We propose models for the small- and large-scale fading correlation. A simulation model based on our analysis is also provided. Our results have relevance for the analysis of bit error rates, diversity order, and diversity/multiplexing tradeoff in clustered sensor networks.

---

Accepted with minor revisions and resubmitted to *IEEE Transactions on Wireless Communications*, February 2009, as
S. Wyne, A. Singh, F. Tufvesson, and A. F. Molisch,
"A Statistical Model for Indoor Office Wireless Sensor Channels."

# 1 Introduction

[13]Wireless sensor networks have been very actively researched in the last few years. A wireless sensor network consists of a number of low-cost, low-power sensor nodes, which can perform sensing, simple computation, and communication over short distances [2]. Such networks essentially gather information pertaining to the surrounding environment and transmit the data to a nearby sink either directly or via intermediate nodes. In the indoor scenario, wireless sensor networks have potential applications ranging from security surveillance and inventory management to telemedicine sensors for advanced health care services [3]. The radio resources for such networks are often constrained, i.e., bandwidth is shared among a large number of nodes and the transmit power is usually limited. Furthermore, the network may face diverse channel conditions among its nodes. These issues can be alleviated through multihop relaying [4] or cooperative communication among the nodes [5], [6], [7], [8].

The performance of sensor networks, e.g., capacity, reliability, energy consumption, and latency, under any of the above schemes depends on the statistics of the propagation channels between the sensor nodes. For example, the fading statistics between sensor node pairs determines the amount of cooperation required between nodes to achieve a certain outage probability [9]. Furthermore, the popular interpretation of clustered sensor networks as distributed MIMO systems critically hinges on statistics of the propagation channels within each node cluster [10], [11]. Despite this fundamental importance of propagation channel statistics, few measurements of channels between sensor nodes are available. To our best knowledge there are no in-depth experimental investigations of the fading statistics of the indoor propagation channel for sensor network communications. This is in stark contrast to the extensive measurements of indoor cellular or wireless LAN links, which exhibit different placements and heights of the nodes, and therefore different channel characteristics, see e.g. [12], [13] among others.

In this paper, we present the results of an extensive measurement campaign and a model that for the first time describes the fading statistics for such indoor sensor networks. The nodes are placed in an office environment, always in close proximity to the walls, at heights of 20, 60, and 100 cm above the floor. Such node placements, at typical heights of work-table/ wall power-socket, are probable in a scenario of intercommunicating sensor nodes, e.g., in ambient intelligence networks [14]. The measurement frequency is 2.6 GHz, which is close enough to the 2.45 GHz ISM band to yield similar propagation characteristics, but separated enough that the measurements did not suffer from interference from microwave ovens, wireless LANs, etc. Based on those measurements, we derive a stochastic channel model for the distance-dependent fading applicable to inter-sensor communication in the indoor office scenario. We find that the distribution of the narrowband fading amplitude can be modeled as Ricean in a majority of the cases, though the values of the Ricean

---

[13†] Preliminary results from a subset of the measurements were presented at Globecom 2007 [1].

$K$-factor, $K_{\mathrm{Rice}}$, are generally not very large.[14] Furthermore, $K_{\mathrm{Rice}}$ values do not necessarily increase monotonically with decreasing separation between transmit (Tx) and receive (Rx) nodes. Since a Ricean fading channel with large $K_{\mathrm{Rice}}$ approximates an additive white Gaussian noise (AWGN) channel, our results show that the AWGN assumption is not guaranteed at small Tx-Rx separation - a fact that can have important consequences for cooperative communications in the investigated scenarios. Our work also addresses the large-scale fading characteristics of the channel. A channel model has been proposed for the correlated fading amplitudes, and is parametrized from our measurements.

The remainder of the paper is organized as follows. In section II, we describe the measurement setup and post processing. Section III contains the results and a model discussion. Section IV outlines model validation and implementation steps. Finally, conclusions are provided in section V.

# 2 Measurement setup and processing

## 2.1 Equipment

The channel transfer functions between different locations of the sensor node antennas were recorded with the RUSK LUND wideband channel sounder that measures the transfer function by means of a multicarrier signal [15]. The measurements were performed at a center frequency of 2.6 GHz with a signal bandwidth of 200 MHz, spanned by 321 subcarriers. The Tx signal was repeated with a period of 1.6 $\mu$s, and had an output power of 27 dBm. The propagation channel was measured along designated routes at regular spatial intervals of $\frac{\lambda}{4}$. At each spatial position, a block of ten snapshots was recorded for enhancement of the measurement signal-to-noise ratio (SNR) through coherent averaging.

The single-element Tx and Rx antennas used in the measurements were commercial Skycross (SMT-2TO6M-A) meander line antennas with linear polarization and dimensions $2.8 \times 2.2 \times 0.3$ cm$^3$ [16]. The azimuth pattern (in the plane perpendicular to axis of the antenna) of those antennas is approximately omnidirectional whereas the elevation pattern exhibits pronounced radiation lobes. The antenna patterns are provided in [1].

## 2.2 Scenario

The measurements were performed in the E-building at LTH, Lund, Sweden in five office rooms[15], each of dimension $6\times3$ m$^2$. The channel sounder's Tx and Rx unit were

---

[14] $K_{\mathrm{Rice}}$ is defined as the power ratio between the deterministic and diffuse components of the channel.

[15] The rooms were selected from separate corridors of the building and had different propagation environments in terms of placement of computers (desktops and/ or laptops) as well as location of furniture that was made of metal, plastic, and wood. The room walls were a mix of brick and light concrete, and the windows had metalized glass, which is a typical

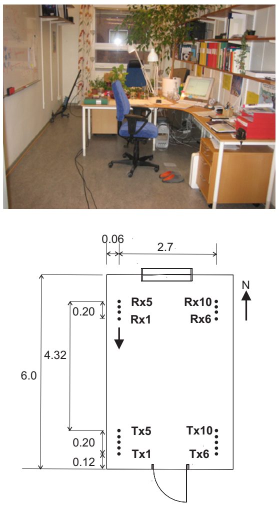

**Figure 1:** Room 2364, window on North wall (Top) and Measurement plan (Bottom).

always placed in the corridor outside the measured room, and antenna cables were partially taped to the floor of the room to avoid their free movement. Furthermore, the fixtures holding the Tx and Rx antenna were made of plastic material. These steps were taken to ensure minimal disturbance of the measured environment. The measurement layout is shown in Fig. 1. A (Rx) measurement run was defined as - the Tx antenna fixed at one of the locations shown in Fig. 1 and the Rx antenna moved slowly towards the Tx antenna, from a start position corresponding to that Tx position. For any fixed Tx position, there exist exactly two corresponding start positions for the Rx measurement run. For example, for Tx placed at position Tx1 in Fig. 1, a Rx measurement run could only initiate from position Rx1 or Rx6. Similarly, for Tx5 position the corresponding Rx start positions were Rx5 or Rx10.[16] The trajectory of the measurement runs was always parallel to the 6 m walls. The channel transfer function was measured along a measurement run at regular spatial intervals of $\frac{\lambda}{4}$. During any measurement run, both Tx and Rx antenna maintained a proximity of 6 cm to one of the 6 m walls. A measurement run where both the Rx and Tx antenna were 6 cm from the same wall, is referred to as a *same-wall* measurement, e.g., Tx at Tx1 and Rx run initiated from Rx1. When this was not the case, e.g., Tx on Tx1 and Rx run initiated from Rx6, then such measurement runs

---

construction in northern Europe and in modern office buildings elsewhere.

[16] This arrangement was used to ensure equi-length measurement runs, i.e., around 4 m length for any same-wall run and around 4.3 m length for an opposite-wall measurement run.

are referred to as *opposite-wall* measurements in the sequel.

The measurement runs were performed at four different combinations of Rx and *nominal* Tx antenna heights; in three cases equal antenna heights were employed, e.g., when both Tx and Rx antenna were placed at 20 cm above floor, this configuration was referred to as Tx20Rx20. Similarly a Tx60Rx60 and a Tx100Rx100 configuration was used. Finally, a measurement configuration with unequal antenna heights, where Tx and Rx antenna were set at 100 cm and 20 cm, respectively, above the floor was also used.

To increase the number of measurement runs, i.e., to increase the ensemble size for statistical analysis, each measurement run was repeated with the Tx antenna raised by 5 cm relative to it's *nominal* height. Taking the example of Tx20Rx20 configuration, this meant that measurement runs were performed with the Tx antenna at 20 and 25 cm above floor. Therefore, a total of 200 runs (5 rooms × 10 Tx positions × 2 Tx heights × 2 Rx start positions) were measured for the Tx20Rx20 configuration. This number includes 100 same- and 100 opposite-wall runs, respectively. The same number of measurement runs was accumulated for the other three height configurations. This set of measurement runs constituted the statistical ensemble used for subsequent analysis of the fading.

For the same-wall measurements the antenna axes were rotated 90 degrees, in the vertical-plane perpendicular to the wall, such that the uniform azimuth pattern became the uniform elevation pattern in the rotated position. This was done because a uniform elevation pattern allows an accurate characterization of the floor reflections in the same-wall case; otherwise the strength of the floor-reflected component would have been materially influenced by the lobes of the elevation pattern. Furthermore, with a 6 cm separation to the nearest wall, the small angular separation between the direct and wall-reflected components results in similar antenna gain in the direction of the direct and wall-reflected components in the same-wall case.

## 2.3 Data Post Processing

In a fading channel the total power gain, $G$, experienced by the received signal, is conventionally modeled as [17]

$$\begin{aligned} G_{\mathrm{dB}}(d) &= P_{\mathrm{Rx,dB}} - P_{\mathrm{Tx,dB}} \\ &= G_{0,\mathrm{dB}} - n10\log(d) + X_{\mathrm{SSF,dB}} + X_{\mathrm{LSF,dB}}, \end{aligned} \tag{1}$$

where $d$ is the Tx to Rx distance, $G_{0,\mathrm{dB}}$ is the path power gain in dBs at the reference distance, $d_0 = 1$ m, and $n$ is the pathloss exponent. Furthermore, $X_{\mathrm{SSF}}$ is the small-scale fading (SSF) contribution, i.e., the random variation of signal level due to multipath interference observed over one small-scale area[17] (SSA). Finally, $X_{\mathrm{LSF}}$ is the large-scale fading (LSF) contribution, i.e., the random variation in local average of Rx power observed over a spatial extent of multiple SSAs. In our analysis, these

---

[17] Small-scale refers to the spatial extent of such a region, which is on the order of a few carrier wavelengths, $\lambda$.

contributions were extracted from each measurement run through post-processing. The parameters $G_{0,\mathrm{dB}}$ and $n$ were estimated by a least squares fit of $G_{0,\mathrm{dB}} - n10\log(d)$ to the dB values of Rx power averaged over all tones. The deterministic path gain was then removed by multiplying the channel coefficients, in linear-scale, with an appropriate distance dependent term. Next, the LSF at the $i$-th spatial sample was estimated by averaging over the SSF contribution as,

$$X_{\mathrm{LSF},i} = \frac{d^n}{G_0} \cdot \hat{E}_{\mathrm{SSF}}\left[|H_{ij}|^2\right], \tag{2}$$

$$\hat{E}_{\mathrm{SSF}}\left[|H_{ij}|^2\right] = \frac{1}{20F}\sum_{i=1}^{20}\sum_{j=1}^{F}|H_{ij}|^2, \tag{3}$$

where, $H_{ij}$ is the channel coefficient measured at the $i$-th spatial sample and $j$-th subcarrier, $G_0 = 10^{\frac{G_{0,\mathrm{dB}}}{10}}$, $F$ is the number of subcarriers in the signaling bandwidth, and finally $\frac{1}{20}\sum_{i=1}^{20}(\cdot)$ represents a sliding-window average of the received power along a measurement run. It is assumed here that averaging over space and frequency are equivalent for small-scale analysis [18].[18] Subsequently, the SSF contribution, $X_{\mathrm{SSF},ij} = H_{ij}^{\mathrm{norm}}$, to the amplitude of the measured channel coefficients can be obtained as,

$$H_{ij}^{\mathrm{norm}} = \sqrt{\frac{d^n}{G_0} \cdot \frac{1}{X_{\mathrm{LSF},i}}} \cdot H_{ij}. \tag{4}$$

The SSF statistics were analyzed along the length of a measurement run using a sliding window segment of 20 adjacent spatial samples[19]. Each of these $4\frac{3}{4}\lambda$ length segments was treated as an SSA for the small-scale analysis.

For each SSA, small-scale statistics such as $K_{\mathrm{Rice}}$ were estimated from 6420 samples of the channel coefficients, $H_{ij}^{\mathrm{norm}}$ (20 spatial samples $\times$ 321 frequency samples). Amongst these samples, approximately 170 are considered to be statistically independent [1]. This estimate is based on the working that within an SSA length of $\approx 5\lambda$, a small-scale decorrelation distance of approximately $\frac{\lambda}{2}$ gives 10 independent spatial samples. Furthermore, a median coherence bandwidth estimated at 12 MHz gives 17 independent samples over 200 MHz measurement bandwidth. These 17 samples from frequency domain are available at each of the 10 spatial samples, giving the approximate figure of 170 independent samples. We note that this number is relatively low, and may lead to uncertainties in the estimated parameters. However, a limitation on the number of independent samples is inherent in the analyzed scenario, and cannot be eliminated by increasing length of the SSA or measurement bandwidth:

---

[18] The small-scale fading is caused by phase-changes of the interfering multipath components. These phase-changes may occur due to traversing small-scale distance, or at a fixed delay by traversing the spectral lines across the 200 MHz measurement bandwith. Therefore, small-scale averaging can be performed equivalently over space and time for our measurements.

[19] The number 20 comes from a trade-off between two conflicting requirements; to have sufficient statistical samples, and the necessity, by definition of a small-scale region [17], to have negligible variation in the mean Rx power. See also the discussion later in this section.

(i) Increasing the length of the SSA: The SSA segment of length $4\frac{3}{4}$ wavelengths is smaller than the $10 - 20$ $\lambda$ that are commonly used as SSA window length. This smaller window size was selected empirically[20] to satisfy the requirement that the running average of Rx power should not exhibit appreciable change ($<$ 5dB) within the span of the window. Hence wide sense stationarity can be assumed to hold over the length of an SSA segment.

(ii) Increasing the measurement bandwidth: although this approach would lead to a larger number of independent samples; it is difficult to implement, and also faces fundamental problems. When the measurement bandwidth exceeds 10 - 20 % of the carrier frequency, channel statistics may differ among different sub-bands of the measurement spectrum due to frequency selective interactions with scatterers [19]. Hence, the uncorrelated-scattering assumption of [20] is violated[21].

# 3 Results

## 3.1 Small-Scale Statistics

### Envelope Distribution

A number of different distributions have been proposed for the small-scale amplitude fading in indoor office environments, and various justifications have been given for them. The most prominent among them are Rayleigh and Rice distributions. The former two are usually justified by means of the central limit theorem (CLT), implying that a large number of multipath components, having the same statistical properties are present. In our case, the theoretical conditions for the validity of the CLT are not necessarily fulfilled, since - for the same-wall measurements - we can expect three strong components (direct component, floor reflection, and wall reflection) plus a number of weaker multipath components. Still, we consider Rayleigh and Rice distributions as appropriate *functional fits* to the measured fading distributions. In addition to our work in [1], the Nakagami-m, Weibull and lognormal distributions are also considered in this work as potential candidates to model the amplitude fading. These distributions have been frequently used in modeling indoor scenarios, see e.g., [21], [22] and references therein. Several other fading distributions have been introduced in the literature [23], [24], [25], but those tend to have a larger number of free parameters. They do not appear to be in widespread use and we do not consider them here any further.

We use Akaike's Information Criteria (AIC)[26] to select among the candidate distributions; Rayleigh, Rice, Nakagami-m, Weibull, and lognormal, the model that best fits the empirical distribution of the fading amplitudes. The latter distribution

---

[20] After comparing various lengths of the averaging window for different measurement routes.

[21] The wide sense stationarity condition may still be valid. Though, a violation of the uncorrelated scattering assumption means that the channel modeling effort will be frequency specific.

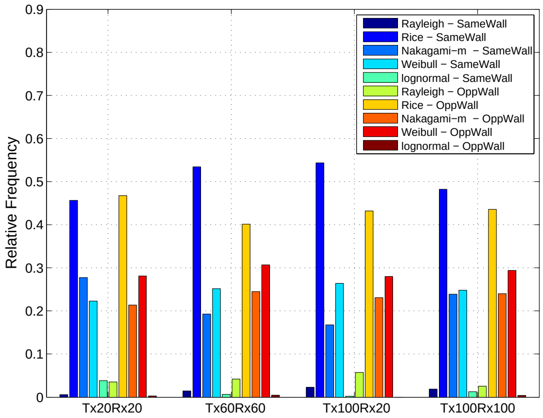

**Figure 2:** Relative frequencies of AIC selecting a candidate distribution as best fit to empirical distribution of small-scale fading amplitudes. The ensemble of SSAs is drawn from measurement runs in all the rooms.

is also known as the operating model in this context. The application of AIC to the problem of selecting an appropriate small-scale fading model was recently proposed by [21]. The AIC is an asymptotically (in sample size) unbiased estimator of the relative expected Kullback-Leibler (KL) distance between the operating model and the candidate distributions and thus allows the selection of the model with the smallest KL distance to the measurements [27]. The AIC for the $j$-th candidate distribution that has a probability density function $g_{\theta^j}$, is given by [27],

$$AIC_j = -2 \sum_{n=1}^{N} \log_e g_{\hat{\theta}^j}(x_n) + 2\eta, \tag{5}$$

where $\hat{\theta}^j$ is the maximum likelihood estimate of the distribution's parameter vector, $\theta^j$, obtained from $N$ independent identically distributed (IID) observations, $\mathbf{x} = x_1 \ldots x_N$. Furthermore, $\eta$ is the dimensionality of $\theta^j$, and $\log_e$ denotes natural logarithm. Among the candidate distributions, the best fit will have the minimum value of $AIC_j$. Fig. 2 shows the relative frequency of AIC selecting each of the candidate distributions as best fit. The Ricean distribution provides the best fit in a majority of the cases. This is valid for different antenna height combinations in same- and opposite-wall scenarios. Therefore the Ricean model is concluded to be the best parametric fit, to distribution of the small-scale fading amplitudes. Additionally, sample plots of the empirical cumulative distribution function (CDF) and theoretical model fits are given in Fig. 3. These graphs provide some idea of the suitability of

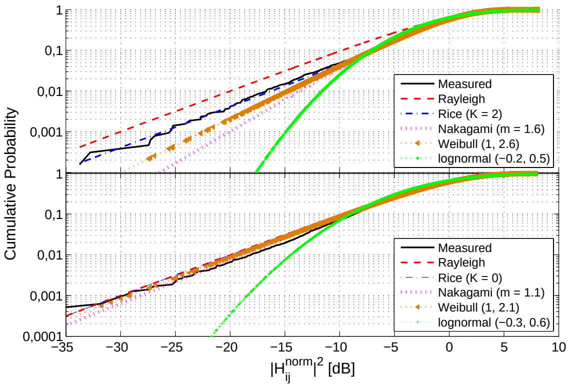

**Figure 3:** Sample empirical CDFs of the small-scale fading amplitudes and their theoretical model fits. Measurements taken in Tx20Rx20 configuration for a same-wall (top plot) and opposite-wall (bottom plot) scenario. The ensemble is scaled to unit mean power, and dB units indicate relation to this mean. The AIC selected Rice in the top plot and Nakagami-m in the bottom plot. Distribution parameters for theoretical fits, e.g., Weibull(shape, scale) and Lognormal(mean, STD) are also provided. Note that the y-axis origin in the plot above is coincident with the (x=0, y=1) point shown on the bottom plot.

proposed theoretical models. For the measured channels, empirical distribution of all non-zero (in linear scale) $K_{\text{Rice}}$ observations is provided in Fig. 4. In comparison to [12], which reports $K_{\text{Rice}}$ values for an indoor access-point type scenario, the $K_{\text{Rice}}$ values observed in our sensor scenario are not too large. This fact together with the observation of spatial variation of $K_{\text{Rice}}$ (refer discussion in Sec. 3.1) has implications for system design.

## Ricean K-factor

Further studies of the Rice factor as a function of distance reveal several interesting observations:

1. *Rice factors are often small enough to allow description of the fading by Rayleigh distributions.* While the AIC rarely gives the Rayleigh distribution as the optimum distribution, in many cases the extracted $K_{\text{Rice}}$ was small enough to be well-approximated as 0.

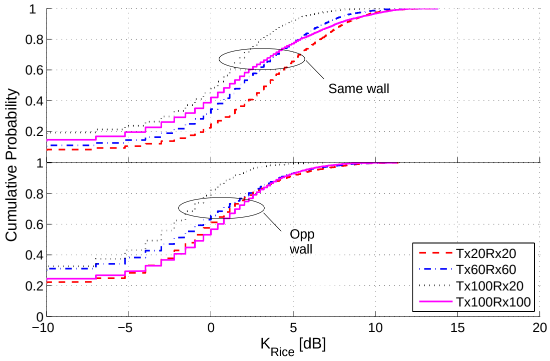

**Figure 4:** Maximum likelihood estimates of $K_{\text{Rice}}$ for the different SSAs. Note that the y-axis origin in the plot of same-wall CDFs is coincident with the (x=0, y=1) point shown on the plot of opp-wall CDFs.

2. *The Rice factor is a lognormally distributed random variable with distance-dependent parameters.* For each given distance, we obtain an ensemble of estimated $K_{\text{Rice}}$ from measurement runs in all the rooms. The logarithms of the samples in this ensemble are normally distributed[22], $\mathcal{N}\left(\mu_{\text{dB}}, \sigma_{\text{dB}}\right)$. In the sequel, the distance dependent variation of $K_{\text{Rice}}$ observed over the ensemble of all measurement runs is described by a mixture model for the probability density function,

$$p_{K_{\text{Rice}}}\left(k_{\text{Rice}}\right) = \alpha \cdot \mathcal{N}\left(\mu_{\text{dB}}, \sigma_{\text{dB}}\right) + (1-\alpha) \cdot \delta\left(k_{\text{Rice}}\right), \tag{6}$$

where $\mathcal{N}$ denotes a lognormal distribution with mean of the logarithmic Rice factor, $\mu_{\text{dB}}$, and standard deviation, $\sigma_{\text{dB}}$, and $\alpha$ is the mixture weight. All three parameters are considered to be functions of the Tx-Rx separation. The Dirac impulse at zero, $\delta\left(k_{\text{Rice}}\right)$, accounts for the cases where the grid-search returns a maximum-likelihood estimate of $\hat{K}_{\text{Rice, ML}} = 0$. The ensemble whose pdf is considered is the measurement runs in the different rooms, and with different Tx positions.

The parameter values in Eq. (6) generally depend on the link distance, $\chi$, defined as the distance between the Tx and the mid-point of the considered SSA. We model this dependence by a polynomial fit, with the fitting parameters

---

[22] The Gaussianity of dB values was verified though plots are not shown here due to space limitations.

**Table 1:** parameters for k-factor mixture model.

| | $\mu_{\text{dB}}$<br>$P(\chi) = c_3\chi^3 + c_2\chi^2 + c_1\chi + c_0$ | | | | $\sigma_{\text{dB}}$<br>$P(\chi) = b_0$ | $\alpha$<br>$P(\chi) = a_1\chi + a_0$ | |
|---|---|---|---|---|---|---|---|
| | $c_3$ | $c_2$ | $c_1$ | $c_0$ | $b_0$ | $a_1$ | $a_0$ |
| Same Wall | | | | | | | |
| Tx20Rx20 | 1.23 | −9.52 | 20.64 | −8.17 | 3.84 | −0.05 | 1.05 |
| Tx60Rx60 | −0.84 | 5.80 | −14.6 | 14.68 | 3.61 | −0.06 | 1.04 |
| Tx100Rx20 | 0.17 | −1.74 | 4.27 | −1.78 | 3.84 | −0.07 | 0.99 |
| Tx100Rx100 | −0.43 | 3.57 | −10.09 | 10.66 | 4.80 | −0.04 | 0.98 |
| Opposite Wall | | | | | | | |
| Tx20Rx20 | 0.79 | −6.41 | 12.06 | 1.58 | 3.75 | −0.13 | 1.25 |
| Tx60Rx60 | −1.72 | 18.62 | −67.55 | 81.64 | 4.47 | −0.11 | 1.12 |
| Tx100Rx20 | 0.16 | −0.73 | −2.01 | 6.61 | 3.76 | −0.06 | 0.93 |
| Tx100Rx100 | −1.40 | 15.13 | −54.8 | 66.72 | 4.14 | −0.02 | 0.85 |

$\chi$ = Distance between Tx and mid-point of modeled SSA [m].

provided in Table 1. Note that for some antenna configurations and small Tx-Rx separation the mixture weight, $\alpha$, values modeled by the least-squares curve may slightly exceed unity, in which case they should be truncated to one. For system simulation with the proposed Ricean fading channel, $K_{\text{Rice}}$ would be drawn from Eq. (6) with values of the distribution parameters determined from Table 1. Furthermore, the SSA under consideration is assumed to be centered at the distance which determines values for the distribution parameters of $K_{\text{Rice}}$.

3. *The mean Rice factor is* ***not a monotonic*** *function of the distance.* Theoretical studies on communication between clusters of sensor nodes often make simplifying assumptions about the propagation channels between the nodes. The two most popular models are (i) Rayleigh fading between *all* nodes, independent of the distance between them, (ii) Rayleigh fading between nodes belonging to different clusters and AWGN (or equivalently Ricean fading with high $K_{\text{Rice}}$) for nodes communicating within a cluster, i.e., at small Tx-Rx separation, see e.g., [10], [11] and references therein. It also seems intuitively pleasing that the Rice factor would increase as the separation between Tx and Rx decreases, and eventually reach very high values for small separations.

   However, our measurements show quite different trends - there is no monotonic increase in $K_{\text{Rice}}$ with decreasing distance. This can be observed from Figs. 5 and 6, which show the mean values of $K_{\text{Rice}}$ (in dB) as a function of Tx-Rx separation for same-wall and opposite-wall measurements, respectively. The mean at each distance is taken over the ensemble of $K_{\text{Rice}}$ observations obtained from measurements in all rooms. An intuitive explanation for this behavior was given in [1] based on the interference pattern of the dominant deterministic compo-

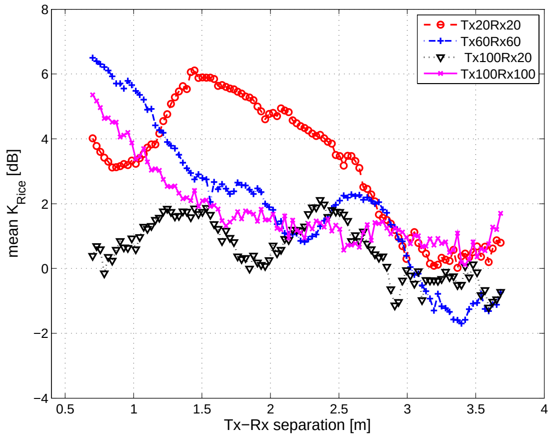

**Figure 5:** Mean of $K_{\text{Rice}}$ in dBs as a function of Tx-Rx separation for same-wall measurements. The mean is taken over measurements in all rooms. The x-coordinates of the plots correspond to the parameter $\chi$ in Table I.

nents (direct component, wall-reflected, and the floor -reflected components).[23]

4. *Rice factors in different SSAs are approximately decorrelated.* For completeness of this modeling approach, we investigated the autocovariance of the $K_{\text{Rice}}$ values along a measurement run. Our analysis, for all antenna heights, reveals that the normalized autocovariance for $K_{\text{Rice}}$ smoothly decays to a value around 0.5 within a distance of 0.55 m, i.e., decorrelation[24] is achieved over the length of one SSA segment. It can therefore be concluded that the model of Eq. (6) can be used to draw $K_{\text{Rice}}$ values for two arbitrary SSAs whose mid-points are separated by the dimensions of one or more SSAs. The case where adjacent SSAs overlap is not within the scope of this model[25].

## Correlation of small-scale fading

Another important characteristic of the small-scale fading is the spatial correlation of the small-scale fading, since it describes achievable spatial diversity. While various

---

[23] Note that such a three-ray model is not exactly compatible with a Ricean fading distribution, but is only used to make some qualitative statements about fading depth.

[24] Refer Sec. 3.1 for discussion.

[25] Modeling aspects are further discussed in Sec. 4.

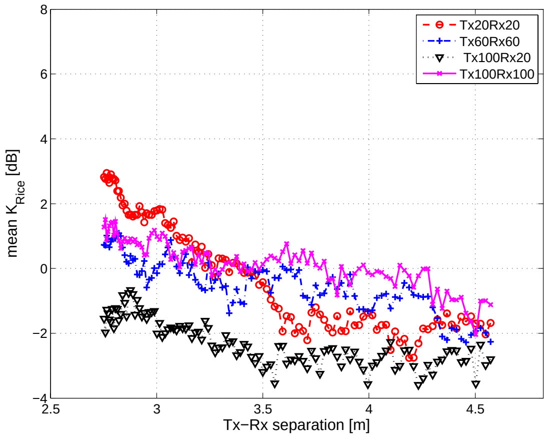

**Figure 6:** Mean of $K_{\text{Rice}}$ in dBs as a function of Tx-Rx separation for opp-wall measurements. The mean is taken over measurements in all rooms. The x-coordinates of the plots correspond to the parameter $\chi$ in Table I.

correlation coefficients can be defined [28], [19], we concentrate here on the autocovariance of the squared envelope of the received signal amplitude, since it determines the spatial selectivity of the received SNR. From measurements the normalized autocovariance of the squared envelope process is estimated from Eq. (7), where $\Delta i = 0, 1, \ldots, (20 - k)$ is the separation between samples of interest (in units of $\frac{\lambda}{4}$), and $k = 10$ is the fixed number of spatial samples used for averaging. Furthermore, $E_{(i \ldots i+k),\ F}\left[\cdot\right]$ denotes statistical expectation over spatial samples $i$ through $i+k$ and all $F$ frequency tones. Similarly $VAR_{(\cdot)}\left[\cdot\right]$ is the statistical variance operator. The other symbols have already been defined for Eq. (2) through (4).

In estimating the autocovariance in Eq. (7), an equal number of statistical samples, $k \cdot F$, has been used to calculate each value. This means that the estimated autocovariance sequence is equally reliable at all considered lags. An analysis in the frequency domain showed that we had a median coherence bandwidth of 12 MHz and so approximately 17 independent samples from the frequency domain per spatial position. This together with the spatial averaging ensures that we use in excess of 50 independent samples in each estimate of the autocovariance.

In the investigations of decorrelation found in published literature, different threshold levels have been used to define decorrelation, e.g., 0.9, 0.7, 0.5 and $e^{-1}$. In this work, decorrelation distance is defined as

$$d_{\text{de-corr}} = \min \left\{ \Delta d : \rho_{\text{COV}} \left( \Delta i \right) \leq 0.5 \right\}, \tag{8}$$

$$\hat{\rho}_{\mathrm{COV}}\left(\Delta i\right) = E_{(i\ldots i+k),(i+\Delta i\ldots i+\Delta i+k),\;F}\left[\frac{\left|H_{ij}^{\mathrm{norm}}\right|^2 - E_{(i\ldots i+k),\;F}\left[\left|H_{ij}^{\mathrm{norm}}\right|^2\right]}{\sqrt{VAR_{(i\ldots i+k),\;F}\left[\left|H_{ij}^{\mathrm{norm}}\right|^2\right]}}\cdot\right.$$

$$\left.\frac{\left|H_{i+\Delta i\;j}^{\mathrm{norm}}\right|^2 - E_{(i+\Delta i\ldots i+\Delta i+k),\;F}\left[\left|H_{i+\Delta i\;j}^{\mathrm{norm}}\right|^2\right]}{\sqrt{VAR_{(i+\Delta i\ldots i+\Delta i+k),\;F}\left[\left|H_{i+\Delta i\;j}^{\mathrm{norm}}\right|^2\right]}}\right], \tag{7}$$

where $\Delta d = \frac{\lambda}{4}\cdot\Delta i$. The distribution of small-scale $d_{\text{de-corr}}$ at different antenna heights is shown in Fig. 7. Some of the CDF curves do not reach unity, which is representative of the fraction of SSAs where decorrelation according to Eq. (8) is not achieved within the observed distance. Otherwise the plots show that in 70 % of the measured SSAs, decorrelation is achieved within one wavelength. We now turn our attention to the auto*correlation*, i.e., including the impact of the mean. Fig. 8 shows the autocorrelation of squared envelope for three different SSAs with corresponding $K_{\mathrm{Rice}}$ values. As expected, the higher $K_{\mathrm{Rice}}$ values result in a more correlated channel. We model the impact of the Rice factor on the autocorrelation function by an equation of the following functional form,

$$\begin{aligned}R\left(\Delta d\right) = &\left[\mathrm{sinc}^2\left(2\frac{\Delta d}{\lambda}\right) + 2K_{\mathrm{Rice}}\cdot\mathrm{sinc}\left(2\frac{\Delta d}{\lambda}\right)\cdot\right.\\ &\left.\cos\left(2\pi\frac{\Delta d}{\lambda}\cos\left(\theta_0\right)\cos\left(\beta_0\right)\right)\right]\cdot\\ &\left(\frac{\Omega}{1+K_{\mathrm{Rice}}}\right)^2 + \Omega^2,\end{aligned} \tag{9}$$

where $\Omega = E\left[\left|H_{ij}^{\mathrm{norm}}\right|^2\right]$, and the pair of angles $(\theta_0, \beta_0)$ specify the specular component's azimuth and elevation, respectively. In our scenario $\theta_0$ is measured with respect to the direction along which spatial samples are measured, and $\beta_0$ is measured relative to the horizontal plane at Rx antenna height. The model in Eq. (9) represents the autocorrelation function of Ricean fading where the diffuse component is due to three-dimensional (3-D) uniform scattering (as obtained from [29], by inserting the results from [30], [31]). This model is not necessarily representative of the physical propagation scenario that may contain more than one dominant specular component. However, as discussed in the sequel, the *functional form* models the autocorrelation reasonably well and has the advantage that simulation models for Ricean fading is a well-investigated topic in the published literature. The normalized autocorrelation

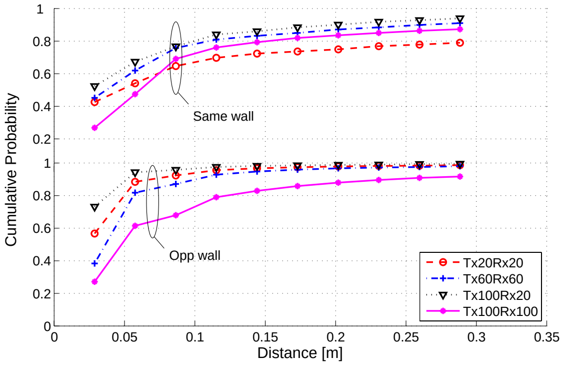

**Figure 7:** Distribution of the small-scale decorrelation distance. Note that the y-axis origin in the plot of same-wall CDFs is coincident with the (x=0, y=1) point shown on the plot of opp-wall CDFs.

model, $\rho\left(\Delta d\right) = \frac{R(\Delta d)}{R(0)}$, is plotted in Fig. 8 together with the corresponding autocorrelations estimated from measurements. We observe that the model matches very well at large $K_{\text{Rice}}$, while at small $K_{\text{Rice}}$ the model fits reasonably well at small lags but shows a smaller correlation than the estimated values at large lags. This can be attributed to the non-isotropic antenna pattern used in the measurements which causes a higher correlation compared to the isotropic antennas assumed in the model. In Fig. 8 for comparison we also show the autocorrelations arising from a channel model where a specular component in 2-D uniform scattering is assumed [32].

## 3.2 Large-Scale Characteristics

### path gain

The path gain averaged over LSF and SSF is conventionally modeled as a power law decay in distance. The pathloss exponent, $n$, in this model is determined by a least-squares fit to a scatter plot of Rx power in dB over log-distance. In our analysis, the parameters $n$ and $G_{0,\text{dB}}$ have been estimated by a least-squares fit of $G_{0,\text{dB}} - n10\log(d)$ to dB values of the narrowband path gain averaged over all tones. The fitting is performed individually for each of the 100 measurement runs (5 rooms × 10 Tx positions × 2 Tx heights) at each nominal antenna height configuration in same- and opposite-wall scenarios. The estimates of $n$ and $G_{0,\text{dB}}$ were observed to be

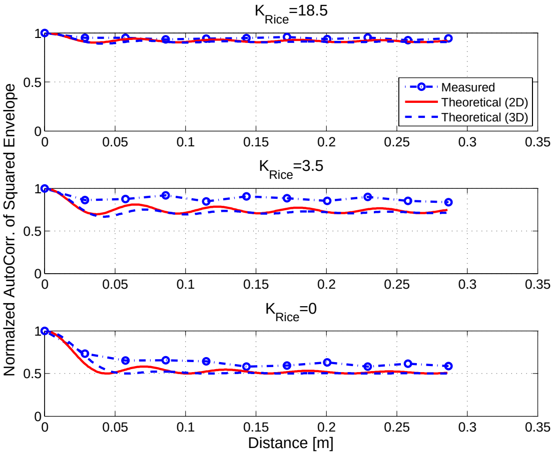

**Figure 8:** Comparison of small-scale autocorrelation model with autocorrelation estimated from measurements at different $K_{\text{Rice}}$. The plots are for Tx20Rx20 antenna configuration in the same-wall scenario, i.e., $\theta_0 = 0$, and $\beta_0 = 0$.

correlated Gaussian random variables[26] with distribution parameters $\mathcal{N}(\mu_n, \sigma_n)$ and $\mathcal{N}(\mu_{G_0,\text{dB}}, \sigma_{G_0,\text{dB}})$, respectively, and were also modeled as such. The correlation between the values of $n$ (in linear scale) and $G_{0,\text{dB}}$ was characterized by the normalized correlation coefficient, $|\rho_{nG_{0,\text{dB}}}| \leq 1$. The distribution parameters are provided in Table 2 for the different antenna height configurations in same-wall and opposite-wall scenarios. From the tabulated values, the pathloss exponent is close to 2 for all four antenna heights in the same-wall scenario. The opposite-wall scenarios have higher exponents owing to the obstructed LOS propagation. Furthermore, $n$ and $G_{0,\text{dB}}$ are weakly correlated for the same-wall scenario whereas this correlation is quite strong for all antenna configurations in the opposite-wall scenario.

### Large-Scale Fading Correlation

The LSF in this work is defined as the random variation in local average of Rx power, observed over the spatial extent of multiple SSAs[27]. The Large-scale fading, $X_{\text{LSF,dB}}$, is conventionally modeled as a zero-mean Gaussian process, i.e., $X_{\text{LSF}}$ has a lognormal distribution. In our analysis, the lognormality of $X_{\text{LSF},i}$ estimated from Eq. (2)

---

[26] The Gaussian fit is not shown here due to space limitations.

[27] The conventional notion of shadowing by objects need not occur, as is the case with same-wall measurements.

**Table 2:** large-scale characteristics.

| | $G_{\mathrm{dB}}\left(d\right) = G_{0,\mathrm{dB}} - n10\log\left(d\right)$ | | | | | |
|---|---|---|---|---|---|---|
| | $\mu_{\mathrm{n}}$ | $\sigma_{\mathrm{n}}$ | $\mu_{\mathrm{G_0,dB}}$ | $\sigma_{\mathrm{G_0,dB}}$ | $\rho_{nG_{0,\mathrm{dB}}}$ | $\sigma_{\mathrm{LSF,dB}}$ |
| Same-wall | | | | | | |
| Tx20Rx20 | 2.5 | 0.3 | −50.9 | 2.7 | 0.1 | 1.5 |
| Tx60Rx60 | 2.6 | 0.3 | −50.6 | 1.8 | 0.0 [a] | 1.4 |
| Tx100Rx20 | 1.7 | 0.3 | −55.8 | 1.9 | −0.1 | 1.5 |
| Tx100Rx100 | 2.2 | 0.4 | −50.0 | 3.0 | −0.3 | 1.7 |
| Opposite-wall | | | | | | |
| Tx20Rx20 | 5.9 | 1.1 | −30.8 | 6.2 | 0.9 | 2.1 |
| Tx60Rx60 | 5.0 | 1.0 | −35.8 | 6.6 | 0.9 | 1.7 |
| Tx100Rx20 | 3.1 | 1.1 | −48.0 | 6.1 | 1.0 | 1.3 |
| Tx100Rx100 | 3.3 | 2 | −41.7 | 10.9 | 1.0 | 1.8 |

[a] After rounding-off to one decimal place.

was verified by checking for Gaussian distribution of $X_{\mathrm{LSF,dB},i}$. We observed that the mean of the empirical Gaussian distribution was always in the range of $1-2$ dB and never exactly zero. This is not un-expected since a least-squares criterion was employed in estimating the deterministic(mean) path gain per measurement run. This however does not guarantee that the deviations with respect to the mean, $X_{\mathrm{LSF,dB},i}$, sum to zero over a run (assuming that the SSF is averaged out and has no effect). In subsequent analysis of the LSF, the process mean was removed, i.e., the mean of the $X_{\mathrm{LSF,dB},i}$ observations from a run was estimated and removed from the measured sequence, before including observations in the statistical ensemble to characterize the LSF. Table 2 lists the standard deviation, $\sigma_{\mathrm{LSF,dB}}$, of the lognormal LSF component at all antenna configurations. This is the root-mean-squared value of $X_{\mathrm{LSF,dB},i}$ observations gathered from all 100 measurement runs at each antenna configuration. It can be observed that the estimated values of $\sigma_{\mathrm{LSF,dB}}$ are quite similar for the different scenarios, and lie in the range of 1.4 to 2.1 dB for all antenna configurations.

The autocorrelation of the zero-mean LSF process was also investigated. To ensure that the estimated autocorrelation does not have a contribution from the sliding window averaging, $X_{\mathrm{LSF,dB},i}$ samples picked from each run were spaced apart by one window-length, i.e., for the LSF correlation analysis $\Delta d$ was always an integer multiple of $\left(20 \cdot \frac{\lambda}{4}\right)$. The autocorrelation of the LSF is shown in Fig. 9, and it can be observed that decorrelation is achieved over the span of one small scale area. This result is interesting in that it contradicts the idea of large-scale fading (i.e., it varies at short scale). This suggests that for the measured indoor scenario, with nodes always proximal to the wall, the small-scale and large-scale fading may no longer be clearly distinguishable processes. The observed LSF correlation was similar for all four antenna configurations both in the same- and opposite-wall scenarios. Therefore we have chosen to model the mean of the curves, i.e., the solid black line in Fig. 9. For this purpose, the conventionally used exponential decay model of [33] has been

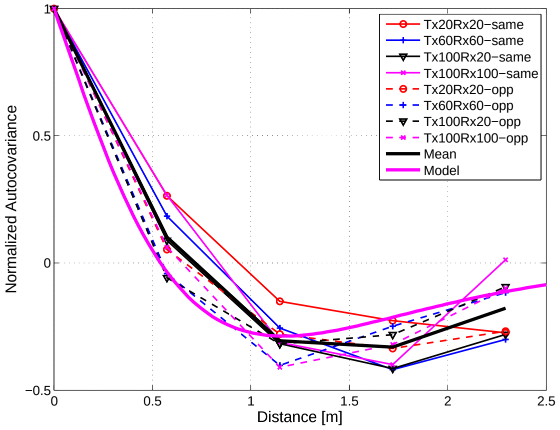

**Figure 9:** Autocorrelation of the Large-scale fading process, empirical results and model.

modified with a cosine term to account for the observed negative correlation. The model is

$$\rho_{dB}(\Delta d) = \exp\left[-\log_e(2)\cdot\frac{\Delta d}{d_{decorr}}\right]\cdot \left(\frac{A\cos\left(C\cdot\frac{\Delta d}{d_{decorr}}\right)+B}{A+B}\right), \tag{10}$$

where $A = 7$, and $B = -6.9$, and $C = 0.1$ have been determined from a least squares fit of Eq. (10) to estimated values of the normalized correlation. From Fig. 9, the model provides a reasonably good fit to the estimated correlation.

## 4 Model implementation and validation

Based on the results provided in Sec. 3, it is possible to model the radio channel by generating a sequence of envelope values that have desired probability distribution, and possess the necessary correlation properties for small- and large-scale fading. The proposed model is useful for SNR investigations and interference analysis between different links (SSAs) in the indoor office sensor scenario. An outline of the necessary steps is provided below:

- For an SSA at given Tx-Rx separation, draw $K_{\text{Rice}}$ from the mixture distribution.

  - Draw a number, $m$, from a uniform distribution, $M \sim U[0,1]$.
  - If $m \leqq \alpha$, draw $K_{\text{Rice}}$ [dB] from the normal distribution, $\mathcal{N}(\mu_{\text{dB}}, \sigma_{\text{dB}})$, otherwise $K_{\text{Rice}} = 0$. Take the parameters $\alpha$, $\mu_{\text{dB}}, \sigma_{\text{dB}}$ from Table 1.

- Generate a sequence, $S_{\text{SSF}}$, of correlated Ricean random variables that represents spatial samples, associated with one SSA, of the small-scale fading channel.

  - This topic is well-investigated in the published literature, see e.g. [34], [35] and the references therein. For the analysis carried out in the sequel, an autoregressive filter of order 20 was used to shape the spectrum of the in-phase component, $r_I$, and quadrature component, $r_Q$, of the sequence of non-zero mean complex Gaussians. Corresponding to the squared envelope autocorrelation given by Eq. (9), the $r_I$ and $r_Q$ sequences both have the autocorrelation

$$R_{r_I r_I}(\Delta d) = \left[\operatorname{sinc}\left(2\frac{\Delta d}{\lambda}\right) + K_{\text{Rice}} \cdot \cos\left(2\pi\frac{\Delta d}{\lambda}\cos(\theta_0)\cos(\beta_0)\right)\right] \cdot \left(\frac{\Omega}{2(1+K_{\text{Rice}})}\right). \tag{11}$$

- Generate a sequence, $S_{\text{LSF}}$, of correlated lognormal random variables, representing the large-scale fading of the channel samples observed over the span of a measurement run.

  - The samples of Rx power in dB, are represented by transforming an IID standard Gaussian sequence into a correlated Gaussian sequence, $\Lambda$, with autocorrelation given by Eq. (10). For results shown in the sequel the sequence, $\Lambda$, was obtained by a matrix product between the matrix square root of the desired autocovariance matrix and the IID Gaussian sequence [36]. The lognormal amplitude sequence, $S_{\text{LSF}}$, is then obtained through the transformation, $S_{\text{LSF}} = 10^{\frac{\Lambda \cdot \sigma_{\text{LSF,dB}}}{20}}$.

- To incorporate SSF and LSF effects simultaneously, i.e., composite fading, generate a third random sequence as the product,

$$S = S_{\text{LSF}} \cdot \acute{S}_{\text{SSF}}. \tag{12}$$

  where the sequence $\acute{S}_{\text{SSF}}$ is the concatenation of six non-overlapping[28] SSA segments, $S_{\text{SSF}}$, which together span the length of a measured run.

- Multiply the sequence with the (distance-dependent) path gain.

---

[28] Refer discussion in Sec. 3.1 on model limitations.

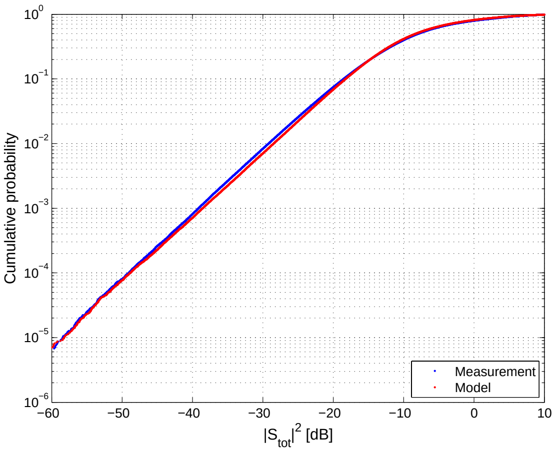

**Figure 10:** Distribution of measured and modeled amplitudes for all SSA realizations in the Tx60Rx60 same-wall scenario.

– Generate the parameters $n$ and $G_{0,\mathrm{dB}}$ as correlated Gaussian random variables. The distance-dependent path gain on dB scale is $G_{0,\mathrm{dB}} - 10nlog\,(d)$. The total path gain, $S_{\mathrm{tot}}$, is then,

$$S_{\mathrm{tot}} = S \cdot 10^{\frac{G_{0,\mathrm{dB}} - 10nlog(d)}{20}}. \tag{13}$$

The model was validated by comparing amplitude distributions obtained from the model and measurement data, respectively. For the measurement CDF, the ensemble is 99 runs × 321 tones per run × 120 spatial channel samples per tone. The number of generated $S_{\mathrm{tot}}$ process realizations is such as to have an equal ensemble size for amplitude CDF of the measurement and model. A sample result for the Tx60Rx60 antenna configuration is shown in Fig. 10.

For the plotted amplitude values, the distance-dependent variation along one run length is always preserved, but for plotting purposes, the full ensemble which consists of multiple runs has been normalized to unit average power. As observed from Fig. 10, the model is in good agreement with measurements down to very small probability levels.

# 5 Summary and Conclusions

This paper has presented results from an extensive indoor office measurement campaign, that characterized the wireless propagation channel for a set of canonical sensor deployment scenarios. Measurements have been performed at four different antenna height configurations, in scenarios where Tx and Rx antenna were located along the same-wall and along opposite-walls of the indoor office room. The small-scale amplitude fading distribution has been analyzed using the Akaike information criteria. Results show that the fading channel is mostly Ricean both for the same-wall and opposite-wall scenarios, though $K_{\mathrm{Rice}}$ values are often not very large. Our measurements indicate that values of $K_{\mathrm{Rice}}$ do not, in general, increase monotonically as the Tx-Rx distance is reduced, these results are contrary to the widely accepted assumption in published literature that the channel is AWGN at a small-enough distance. A probability mixture model has been presented, with distance dependent parameters to account for the distance dependent variations of $K_{\mathrm{Rice}}$. The small-scale spatial selectivity of the channel has been investigated and it has been shown that the correlation drops to 0.5 within a distance of one wavelength in 70% of the SSAs. A $K_{\mathrm{Rice}}$ dependent model for the autocorrelation of the squared envelope has also been provided. Analysis of the large-scale variations of Rx power has shown that the pathloss exponent is close to 2 for the same-wall scenarios, the pathloss exponents for opposite-wall scenarios are larger. The large-scale fading can be modeled as lognormal with a standard deviation around 2 dB for all antenna heights in both the same-wall and opposite-wall scenarios. A correlation model for the large scale fading was also provided. A simulation model was presented according to which a sensor node placed anywhere within the spatial extent of a modeled SSA, is considered to experience the channel statistics applicable to that SSA. Our model is relevant for SNR investigations and interference analysis between different links (SSAs) in the indoor office scenario. The presented results are relevant to communicating within, and between, clusters of nodes and have practical significance because in realistic indoor scenarios the sensors will often be deployed in close proximity to the wall and floor. Strong (but not Rayleigh) fading will occur even between links that have good line-of-sight connection. This means that communication between nodes in a cluster cannot occur with complete reliability, and that the distribution of Rice factors has to be taken into account, in order to arrive at realistic evaluations of the diversity/multiplexing trade-off in ad-hoc networks.

## 6 Acknowledgments

This work was partly financed by High Speed Wireless Center and INGVAR grants of the Swedish Foundation for Strategic Research, and a grant from Vetenskapsrådet, the Swedish Science Council. Perlos AB, Lund is acknowledged for facilitating the antenna pattern measurements. The authors would like to thank the anonymous reviewers for their valuable comments and suggestions.

# References

[1] S. Wyne, T. Santos, F. Tufvesson, and A. F. Molisch, “Channel measurements of an indoor office scenario for wireless sensor applications,” in *Proc. IEEE Globecom 2007*, (Washington DC, USA), 2007.

[2] A. Willig, K. Matheus, and A. Wolisz, “Wireless technology in industrial networks,” *Proceedings of the IEEE*, vol. 93, no. 6, pp. 1130–1151, 2005.

[3] I. F. Akyildiz, T. Melodia, and K. R. Chowdhury, “A survey on wireless multimedia sensor networks,” *Computer Networks*, vol. 51, pp. 921–960, October 2007.

[4] J. A. Gutiérrez, E. H. Callaway, and R. L. Barrett, *Low-Rate Wireless Personal Area Networks: Enabling Wireless Sensors with IEEE 802.15.4*. IEEE Press, 2003.

[5] Y. Hong, W. Huang, F. Chiu, and C. Kuo, “Cooperative communications in resource-constrained wireless networks,” *IEEE Signal Processing Magazine*, vol. 24, no. 3, pp. 47–57, 2007.

[6] J. N. Laneman, D. N. C. Tse, and G. W. Wornell, “Cooperative diversity in wireless networks:efficient protocols and outage behaviour,” *IEEE transactions on information theory*, vol. 50, pp. 3062–3080, December 2004.

[7] A. Sendonaris, E. Erkip, and B. Aazhang, “User cooperation diversity-part I: system description,” *IEEE Transactions on Communications*, vol. 51, no. 11, pp. 1927–1938, 2003.

[8] A. Sendonaris, E. Erkip, and B. Aazhang, “User cooperation diversity-part II: implementation aspects and performance analysis,” *IEEE Transactions on Communications*, vol. 51, no. 11, pp. 1939–1948, 2003.

[9] A. F. Molisch, N. Mehta, J. Yedidia, and J. Zhang, “Performance of fountain codes in collaborative relay networks,” *IEEE Transactions on Wireless Communications*, vol. 6, no. 11, pp. 4108–4119, 2007.

[10] M. Yuksel and E. Erkip, “Diversity gains and clustering in wireless relaying,” in *Proc. IEEE ISIT 2004*, p. 402.

[11] M. Yuksel and E. Erkip, “Multiple-antenna cooperative wireless systems: A diversity-multiplexing tradeoff perspective,” *IEEE Transactions on Information Theory*, vol. 53, no. 10, pp. 3371–3393, 2007.

[12] R. Valenzuela, D. Chizhik, and J. Ling, “Measured and predicted correlation between local average power and small scale fading in indoor wireless communication channels,” in *Proc. IEEE VTC 1998*, vol. 3, pp. 2104–2108.

[13] V. Degli-Eposti, G. Lombardi, C. Passerini, and G. Riva, “Wide-band measurement and ray-tracing simulation of the 1900-MHz indoor propagation channel: comparison criteria and results,” *IEEE Transactions on Antennas and Propagation*, vol. 49, no. 7, pp. 1101–1110, 2001.

[14] C. Ramos, J. Augusto, and D. Shapiro, "Ambient intelligence-the next step for artificial intelligence," *IEEE Intelligent Systems*, vol. 23, no. 2, pp. 15–18, 2008.

[15] R. Thoma, D. Hampicke, A. Richter, G. Sommerkorn, A. Schneider, U. Trautwein, and W. Wirnitzer, "Identification of time-variant directional mobile radio channels," *IEEE Trans. Instrumentation and Measurement*, vol. 49, pp. 357–364, 2000.

[16] http://www.skycross.com.

[17] A. F. Molisch, *Wireless Communications*. Chichester, U.K.: Wiley, 2005.

[18] R. Kattenbach, *Characterization of Time-Variant Indoor Radio Channels by Means of their System and Correlation Functions*. PhD thesis, University of Kassel, Aachen, 1997. in German.

[19] A. F. Molisch, "Ultrawideband propagation channels - theory, measurement, and modeling," *IEEE Transactions on Vehicular Technology*, vol. 54, no. 5, pp. 1528–1545, 2005.

[20] P. A. Bello, "Characterization of randomly time-variant linear channels," *IEEE Transactions*, pp. 360–393, December 1963.

[21] U. Schuster and H. Bolcskei, "Ultrawideband channel modeling on the basis of information-theoretic criteria," *IEEE Transactions on Wireless Communications*, vol. 6, no. 7, pp. 2464–2475, 2007.

[22] D. Cassioli, M. Win, and A. F. Molisch, "The ultra-wide bandwidth indoor channel - from statistical model to simulations," *IEEE Journal on Selected Areas Communications*, vol. 20, pp. 1247–1257, 2002.

[23] D. Polydorou and C. Capsalis, "A new theoretical model for the prediction of rapid fading variations in an indoor environment," *IEEE Transactions on Vehicular Technology*, vol. 46, no. 3, pp. 748–754, 1997.

[24] H. Zhang, T. Udagawa, T. Arita, and M. Nakagawa, "A statistical model for the small-scale multipath fading characteristics of ultra wideband indoor channel," in *Proc. IEEE Conference on Ultra Wideband Systems and Technologies*, pp. 81–85, 2002.

[25] J. Frolik, "A case for considering hyper-rayleigh fading channels," *IEEE Transactions on Wireless Communications*, vol. 6, no. 4, pp. 1235–1239, 2007.

[26] H. Akaike, "Information theory and an extension of the maximum likelihood principle," *Breakthroughs in Statistics, S. Kotz and N. L. Johnson, Eds. originally published in Proc. Int. Symp. Inf. Theory, Budapest, Hungary, 1973*, pp. 610–624, 1992.

[27] K. P. Burnham and D. R. Anderson, *Model Selection and Multimodel Inference: A practical Information-Theoretic Approach, 2nd ed.* New York, U.S.A.: Springer, 2002.

[28] W. C. Jakes, *Microwave Mobile Communications.* IEEE Press, 1974.

[29] T. Aulin, "A modified model for the fading signal at a mobile radio channel," *IEEE Transactions on Vehicular Technology*, vol. 28, no. 3, pp. 182–203, 1979.

[30] F. Vatalaro, "The scattering function of the mobile radio channel in the presence of three-dimensional diffuse multipath," in *Proc. ISITA 1994*, (Sydney, Australia), pp. 1397–1402.

[31] R. H. Clarke and W. L. Khoo, "3-D mobile radio channel statistics," *IEEE Transactions on Vehicular Technology*, vol. 46, no. 3, pp. 798–799, Aug 1997.

[32] G. L. Stuber, *Principles of Mobile Communication*. Massachusetts, USA: Kluwer Academic Publishers, 2nd ed., 2001.

[33] M. Gudmundson, "Correlation model for shadow fading in mobile radio systems," *Electronics Letters*, vol. 27, no. 23, pp. 2145–2146, 1991.

[34] M. Pätzold, *Mobile Fading Channels*. Chichester, U.K.: John Wiley and Sons, 2002.

[35] K. Baddour and N. Beaulieu, "Autoregressive modeling for fading channel simulation," *IEEE Transactions on Wireless Communications*, vol. 4, no. 4, pp. 1650–1662, 2005.

[36] A. Leon-Garcia, *Probability and Random Processes for Electrical Engineering*. Reading, MA: Addison-Wesley, 2 ed., 1994.

# *Paper IV*

# Characterization of a Time-Variant Wireless Propagation Channel for Outdoor Short-Range Sensor Networks

## Abstract

This paper presents sample measurements characterizing the radio channel for outdoor short-range sensor networks. The sensor nodes are placed on the ground in an open area and time-variation of the channel is induced by a person walking in the vicinity of the nodes. The channel statistics of both the line-of-sight component and the overall narrowband signal are non-stationary. The channel (power) gains are found to be significantly influenced by scatterer movement only when the LOS path is blocked. We present a model for the line-of-sight blockage by a person that is similar to that of the referenced work of Pagani and Pajusco, and parameterize and validate it from the measurements. Additionally, we model the time-variant Doppler spectrum of the measured channel's residue (scattered) components. Furthermore, the temporal correlation of small-scale averaged channel statistics, between different links is also investigated.

---

Submitted to *IET Journal on Communications*, February 2009, as
S. Wyne, T. Santos, A. Singh, F. Tufvesson, and A. F. Molisch,
"Characterization of a Time-Variant Wireless Propagation Channel for Outdoor Short-Range Sensor Networks."

# 1 Introduction

Wireless sensor and ad-hoc networks, where nodes communicate without fixed infrastructure, have been a very active research topic in recent times, see e.g., [1], [2], [3], and references therein. Outdoor short-range (inter-node distance less than 10 m) sensor networks are of interest for surveillance, environmental monitoring, and communications applications. The scenario most relevant for practical applications has the nodes at fixed positions near the ground, so that temporal variations occur only due to people/objects moving in the vicinity of the sensors.

As one of the first and most fundamental steps, the wireless propagation channel for such networks needs to be characterized in order to determine performance limits in terms of capacity, reliability, energy consumption, and latency. As an example, the amount of cooperation required between nodes to achieve a certain outage probability is determined by the fading statistics between pairs of sensor nodes [4]. The channel characteristics, in turn, depend on the environment in which the sensor networks are operating. For fixed node wireless links, time-variations are due to motion of scatterers in the vicinity of the nodes. In contrast, when one of the nodes itself is moving, changes in the spatial fading pattern are responsible for the temporal variations of the channel.

To the best of the authors' knowledge, fixed-sensor outdoor channels have not been investigated in detail in the literature. While there is a rich literature on cellular-type outdoor channels [5], cellular transmitters are high above the ground, and thus are significantly different from the scenario we are interested in. Peer-to-peer outdoor communications are usually characterized by the fact that at least one of the devices is moving; furthermore, transceivers are still considerably higher above the ground than in outdoor sensor networks. Several papers, e.g., [6], [7], and [8] measured or modeled outdoor propagation between sensors close to the ground, but did not investigate temporal variations due to moving scatterers, and furthermore concentrated on much larger distances between the sensors. The scenarios in [9], [10], [11] are closest to the ones we are interested in for this paper, in that they measured and modeled temporal variations of the channel due to moving scatterers and in particular considered the effect of people moving through the line-of-sight (LOS). However, those investigations were done in indoor environments.

In this paper we present results for the time-variant narrowband fading statistics from an outdoor measurement campaign where the nodes were static and people were moving in the vicinity of the nodes. While the number of measurement results is not sufficient for a statistically reliable parameterization of a model, we *can* gain qualitative insights into the most important phenomena. The measurements were performed at 2.6 GHz, which is close enough to the 2.45 GHz ISM band to yield similar propagation results, but separated enough that the measurements did not suffer from interference. The antennas, also referred to as nodes, were placed outdoors on the ground in an open grassy field. The nodes were positioned on two parallel rails and measurements were performed with different widths of the rails.

We discuss qualitative effects of a person walking between the rails, particularly when the LOS path[29] is blocked due to this motion. A generic approach is presented to model the temporal variations of the Rx signal strength, arising from a temporary blockage of the LOS path. Our approach has some features common with the method presented in [9]. However, our analysis has the following salient differences:

- We investigate the *narrowband* case of LOS blockage by a moving person, i.e., in addition to characterizing the fading of the first-arriving component, which is extracted from measurements, the fading of the residue (scattered) components of the measured channel is also investigated.
- The contribution of the dominant component is extracted differently.
- The measured scenario is outdoors and consequently the number of significant stationary scatterers is substantially smaller than in a typical indoor environment.
- Multiple links are measured jointly on the rails as opposed to point to point communication links characterized in [9].

It is important to note that the channel statistics are *non-stationary*, as will be reflected in the model we derive from the measurements.

The remainder of the paper is organized as follows. Section II discusses the measurement setup and post processing, section III contains the results and discussion. Finally, the paper is concluded in section IV.

# 2 Measurement setup and processing

## 2.1 Equipment

The channel transfer functions between different sensor nodes were recorded with the RUSK Lund wideband channel sounder that measures the transfer functions, between multiple antenna ports, by means of a multicarrier signal [12]. The measurements were performed at a center frequency of 2.6 GHz and a transmission bandwidth of 200 MHz, spanned by 321 subcarriers (tones). Each of these tones has the interpretation of a separate (possibly correlated) realization of the narrowband channel characterized in this work. The Tx signal was repeated with a period of 1.6 $\mu$s, and had an output power of 27 dBm. The radio channel was measured for all Tx-Rx combinations at a rate of 100 Hz, which is in excess of twice the maximum Doppler frequency due to walking speed of a person.[30] Each measurement record had a duration of 10 sec.

The Tx and Rx antennas were commercial Skycross (SMT-2TO6MB-A) meander line antennas with linear polarization, dimensions $6 \times 3 \times 0.4$ cm$^3$ [13].

Post measurement analysis revealed that only 18 of the 36 SISO channels were actually measured, the same 18 links were used for analysis of all measurement records presented in the sequel.

---

[29] The LOS component is defined as the first-arriving component in the channel impulse response (CIR).

[30] The measurement signal-to-noise ratio was improved by coherently averaging multiple channel snapshots, measured within a span of a few $\mu$s, at the regular 10 ms intervals.

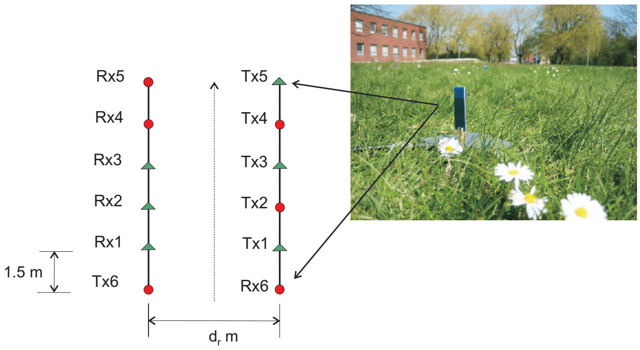

**Figure 1:** Measurement layout for the rails, $d_r = 2, 4$, and 8 m. Nodes that form communication pairs are highlighted by circles or triangles. The movement pattern of the single person walking between the rails is shown by a dashed line. The placement of one of the antennas in the grassy field is also shown.

## 2.2 Scenario

Channel measurements were performed outdoors in a level grassy field near the M-building at LTH campus, Lund, Sweden. The Tx and Rx antennas were fixed at ground level, arranged in two parallel rails, and measurements were performed with spacing of 2, 4, and 8 m between the rails. The time variant behavior of the channel was due to a person walking between the rails and parallel to the orientation of the rails. The measurement configuration is sketched in Fig. 1. The 18 channels measured in each scenario consisted of the following Tx-Rx combinations: Each of Rx elements $1, 2$, and 3 could receive the signal emanating from each of the Tx elements $1, 3$, and 5 ($3 \times 3 = 9$ channels), these nodes are shown by green triangles in Fig. 1. Similarly, each of Rx elements 4,5, and 6 could receive the signals emanating from each of the Tx elements $2, 4$, and 6 ($3 \times 3 = 9$ channels), and these nodes are shown by red circles in Fig. 1. In addition to the opposite-rail channel measured by most of the links, the unique location of Tx6 and Rx6 nodes enables relevant links to measure the same-rail channel, i.e., the channel for which the person moving between the rails does not block the LOS path.

## 2.3 Post Processing

In the analyzed measurements a consistent observation was that the received signal strength of the channel was significantly influenced by the moving person only when the LOS path was blocked by that person. Fig. 2 shows the simultaneous development, over time, of the Rx signal power at various link ends as a person walks between the rails. The Rx power shown for each link is averaged over tones. The influence

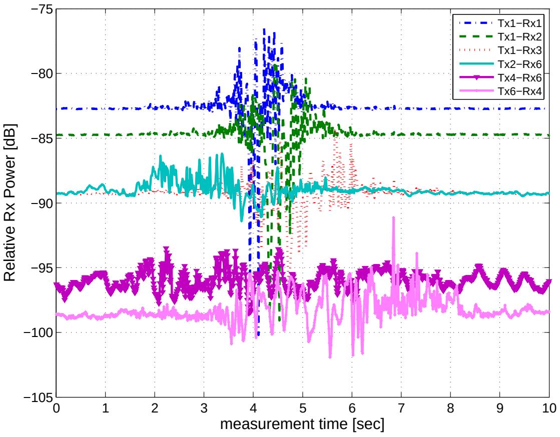

**Figure 2:** Rx power fluctuation at different link ends as one person walks between the rails. The plots are from a 2 m rail measurement. The relative power for each link is averaged over all tones. The three solid-line curves with markers correspond to same-rail links, whereas the other three curves correspond to opposite-rail links.

of the walking person on Rx power is prominently visible for opposite-rail links, e.g., Tx1-Rx1 because the LOS path is blocked temporarily by the person. An interesting observation is that the Rx power is not just continuously attenuated but exhibits oscillations, so that the walking person can increase the signal strength. This can be explained by additional signal energy reaching the receiver after being reflected by the person as long as that person does not block the LOS. In contrast, the same-rail links, whose LOS path is not blocked by the person's motion, exhibit no significant variations of the received power, e.g., refer to the Tx2-Rx6 link.

Besides the overall signal strength, we are interested in the properties of the LOS component only, and the residual channel (scattered components) only. Since the LOS component itself is time-varying, it cannot be retrieved by the standard method of temporally averaging the measured complex channel gains. Rather, we use the following approach: the measured transfer functions, $H_{i,j,k,l}$, are fourier-transformed to the delay domain,

$$h_{i,j,\tau,l} = \frac{1}{K} \cdot \sum_{k=0}^{K-1} H_{i,j,k,l} \cdot \exp\left(j2\pi \frac{k}{K}\tau\right), \tag{1}$$

where $i, j, k, l$ denote Rx and Tx antennas, frequency, and temporal snapshot indexes, respectively, and the variable $\tau$ denotes delay bin index for the channel impulse response (CIR), $h_{i,j,\tau,l}$. Furthermore, $K$ is the number of measured tones. To improve the time-delay of arrival estimate for the LOS peak, the delay grid of the CIR is interpolated with more samples in the inverse FFT than specified by $K$.[31] The interpolation allows plotting the fine details of lobes of the different sinc $(\cdot)$ functions in the CIR, each corresponding to a resolved MPC. The complex gain of the LOS path is estimated as,

$$\begin{aligned} \tau' =& \arg \max_{\tau} \left( |h_{i,j,\tau,l}|^2 \right), \\ h^{\mathrm{LOS}}_{i,j,\tau,l} =& h_{i,j,\tau',l}. \end{aligned} \tag{2}$$

The LOS path's contribution to frequency domain, $H^{\mathrm{LOS}}_{i,j,k,l}$, is subsequently estimated and removed from the measured channel, for future reference we denote as $H^{\mathrm{Res}}_{i,j,k,l}$ the random residue component in the measured channel.[32] The successful removal of the LOS component was verified by a null observed in the residue channel at the location of the removed peak.

Even when averaging out the small-scale fluctuations observed in Fig. 2, we can clearly see that the mean signal power, as well as the power of the LOS component, vary with time. Thus, the fading statistics can be considered to be stationary only within a time window (stationarity interval). The determination of stationarity intervals in our measurements could not be carried out using the method of [14] as it requires high-resolution channel parameter estimation; extension of this method to the distributed physical arrays under consideration is not straightforward. Another method proposed by [15] detects changes in the spatial structure of the channel by thresholding the change in correlation matrix of the MIMO channel. This too could not be applied since the spatial extent of the stationarity region that was to be determined, was on the order of the spatial extent of our distributed antenna arrays. Thus, temporal stationarity lengths for this work were investigated using the method of [16]; a local region of stationarity (LRS) was defined by a set of temporal snapshots where the correlation coefficient between consecutive *averaged* power delay profiles (APDPs) exceeded a pre-defined threshold of 0.5. The correlation coefficient is given by [16],

$$c\left(t_l, \Delta t\right) = \frac{\int \overline{P_h\left(t_l, \tau\right)} \cdot \overline{P_h\left(t_l + \Delta t, \tau\right)} d\tau}{max \left\{ \overline{P_h\left(t_l, \tau\right)}^2 d\tau, \overline{P_h\left(t_l + \Delta t, \tau\right)}^2 d\tau \right\}}, \tag{3}$$

where $\overline{P_h\left(t_l, \tau\right)} = \frac{1}{N} \sum_l^{l+N-1} |h_{i,j,\tau,l}|^2$ is the *averaged*, and $P_h\left(t_l, \tau\right) = |h_{i,j,\tau,l}|^2$ is the *instantaneous* power delay profile (PDP), respectively. Furthermore, $N$ is the number of PDPs to be averaged.

---

[31] For the interpolated version of the CIR, adjacent delay bins are spaced apart by 0.05 ns as opposed to the 5 ns spacing achieved without interpolation. In addition, the FFT is applied with a rectangular window function as this gives the narrowest main-lobe peaks among the different windowing functions.

[32] $H^{\mathrm{Res}}_{i,j,k,l}$ is to be distinguished from $H^{LOS,Res}_{i,j,k,l}$. The latter is the random component within the extracted LOS path, and causes fading of the LOS path.

The correlation coefficient in Eq. (3) is potentially influenced by (i) Number of significant taps in the APDPs, (ii) Averaging length, N, to remove small-scale fading, and (iii) Measurement noise. The suitability of this metric for our measurements was investigated through a simulation study employing stationary realizations of an exponential PDP. Measurement noise was also added corresponding to signal-to-noise ratios observed in our measurements. It was observed that for $N \geq 40$ the correlation always exceeded the threshold over an observation span corresponding to our measurements. In other words, the LRS metric gave the desired infinite duration of stationarity. Consequently, $N = 40$ was also selected for the measurements. Note that this figure is an obvious tradeoff; a larger window size increases the number of independent PDPs available for averaging, while the separability between small- and large-scale effects in the measurements benefits from a small window size. The LRS duration for different measurement scenarios is shown in Fig. 3. It can be observed that $80 - 85\%$ of the intervals of length 0.5 sec can be considered stationary. Consequently, a 0.5 sec interval was considered as the temporal extent of a small-scale area (SSA).

The small-scale characteristics were investigated per SISO link. Within the 0.5 sec wide-sense stationary (WSS) window, the set of $H_{i,j,k,l}$ samples over the indices $k$, and $l$ were considered as a statistical ensemble. Furthermore, the window was slid over the measurement record length of 10 sec to obtain small-scale characteristics in a continuous fashion. As a trade-off between processing time and continuous estimates of small-scale parameters, consecutive windows were set to have 80% overlap, i.e, the start-point of a successive window was advanced by 11 temporal samples with respect to the start point of a preceding window, where a window length is 51 temporal samples.

# 3 Results

## 3.1 Qualitative Behavior of the LOS Component

The received signal, its LOS component, and its scattered components, all exhibit small-scale and large-scale fading that is separated by appropriate signal processing described in Sec. II. In this section, we describe the observed time-varying statistics of these fading processes. The presence of a person moving between the rails causes significant fluctuations, both increase and decrease, of the received signal power. Figure 4 shows a typical example of the power contained in the LOS component, and the signal level averaged over the small-scale fading, i.e., qualitative behavior of signal variations is observed. From Fig. 4 we can infer some qualitative results on the behavior of the LOS path:

1. The extracted LOS path typically exhibits temporal fading, due to the presence of a random component. This is a consequence of finite system bandwidth. Within the delay resolution, leading to 1.5 m spatial resolution in our case, additional multipath components may not be distinguishable from the clean LOS path, and are extracted with it.

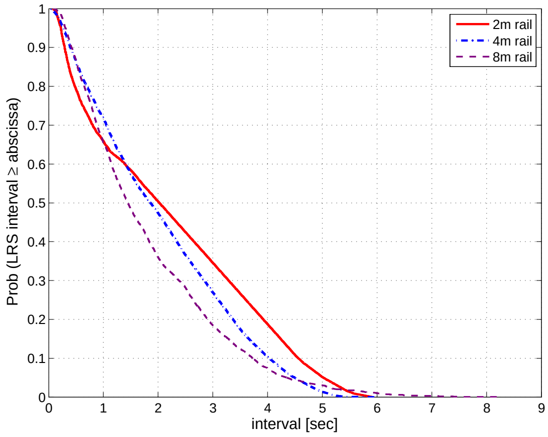

**Figure 3:** Empirical complementary cumulative distribution functions of LRS for different measurements.

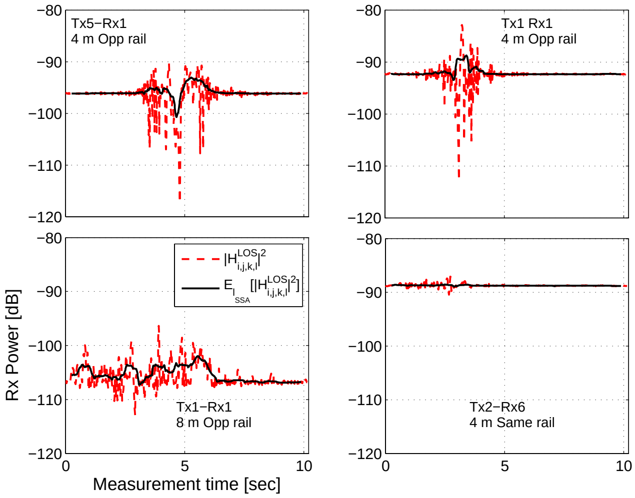

**Figure 4:** Influence of single person moving between rails on the power of $H^{\mathrm{LOS}}_{i,j,k,l}$ (red curve), and moving-average of the power over time (black curve). Various links are shown, as specified by the text in each subplot.

2. The LOS power is not affected unless the link is obstructed by the moving scatterer, e.g., refer to the subplot that shows fluctuations of Rx power on the Tx2-Rx6 (same-rail) link for the 4 m rail.
3. The LOS obstruction by a moving person lasts for less than 1 sec duration, though associated fluctuations typically last 3 sec. This result is partly due to (i) the orientation of the obstructing person, whose trajectory at ordinary walking speed is parallel to the rails, and (ii) the nodes are on the ground and are only obstructed by the leg-region of the moving person.
4. The moving average, over time, of power of the extracted LOS does not always exhibit a significant dip, e.g., in Fig. 4 compare the two subplots in top row. This is, at least partly, due to incomplete separation of the small-scale and the large-scale fading.
5. At large distance (8 m) obstruction of the LOS path does not cause any noticeable attenuation of the LOS power, e.g., refer to bottom-left subplot. This is intuitively explained by the partial/minimal shadowing of the link when spatial extent of the scatterer is small compared to scatterer's distance to either link end.

Inferring from the above observations, for a communications link application the presence of the moving person can be neglected unless the LOS path is obstructed. For surveillance applications, it appears that in that case, monitoring Rx power would not be enough to detect a person in the envisioned scenarios, rather some small-scale fading parameters, e.g., the Ricean $K$-factor ($K_{Rice}$) may have to be monitored to detect an intruder.

## 3.2 Large-Scale Statistics

In order to model the shadowing fluctuations of the LOS component, we find that the model proposed in [9] for the indoor case works well in our scenario as well. The power of the mean component of the Ricean process, $H_{i,j,k,l}^{\mathrm{LOS}}$ exhibits a dip due to LOS blockage, refer to Fig. 4. On a dB-scale, the power of the Ricean mean component can be modeled by a deterministic Gaussian-shaped function, $g\left(t\right)$, written as [9],

$$g(t) = -A_S \cdot \left(1 - \left((t - t_0) \cdot \frac{2}{T_s}\right)^2\right) \cdot \exp\left(-u\left((t - t_0) \cdot \frac{2}{T_s}\right)^2\right). \qquad (4)$$

Based on the 2 and 4 m rail measurements, recommended parameter values are; $A_S = 1$ to 4 dB for the shadowing attenuation, $T_s = 1$ sec for the shadowing duration, and the parameter $u$, which models power gain at the edges of the large-scale fading pattern, has values in the range .5 to 1.[33] Furthermore, $t_0$ represents the shadowing instant, i.e., when the person blocks the LOS, and $t$ is the observation time in seconds. For the 8 m rail, due to a larger link distance, the LOS blockage is minimal such that

---

[33] The positive power gain can be attributed to additional signal energy carried by reflections from the body when it is not blocking the LOS.

the temporal average of LOS power does not exhibit a dip. Therefore, it is proposed to model the 8 m rail scenario by setting $A_S = 0$ in Eq. (4).[34]

To model the temporally varying mean power of the Rayleigh component of the LOS contribution (i.e., the diffuse components that cannot be separated from the *true* LOS component, due to finite system bandwidth), $H_{i,j,k,l}^{\mathrm{LOS,Res}}$, the Rayleigh power is first characterized in relation to power of the mean of $H_{i,j,k,l}^{\mathrm{LOS}}$, i.e., by estimating the temporal $K_{Rice}$ along the recorded length of the extracted LOS, $H_{i,j,k,l}^{\mathrm{LOS}}$. The temporally varying mean power of the LOS Rayleigh component can be expressed in relation to power of the Ricean mean component by a deterministic Gaussian shaped function, $q\left(t\right)$, written on a dB-scale as [9],[35]

$$q(t) = A_{\mathrm{rel}} + A_R \cdot \exp\left(-2\left((t - t_0) \cdot \frac{2}{T_R}\right)^2\right), \tag{5}$$

where $A_{\mathrm{rel}}$ is the dB power difference between the un-obstructed LOS power and the mean power of the random component under those conditions. The values of the parameters were determined by a least-squares fit of the model to measured values; $A_{\mathrm{rel}}$ was typically within the range, $-47$ to $-42$ dB, for both the 2 and 4 m rail measurements. For the 8 m rail measurements, the larger link distance results in $A_{\mathrm{rel}}$ values around $-30$ dB.[36] Furthermore, the range of values for other parameters were $A_R \in [38, 42]$ dB for the 2 and 4 m rails, and $A_R \in [27, 29]$ dB for the 8 m rail. For the width of the bell-shaped curve, $T_R$ is around 6 sec for the 2 and 4 m rails, and $T_R \in [8, 10]$ sec for the 8 m rail. A sample curve for one of the measured links is shown in Fig. 5. One may observe that the modeling approach for the power of the Rayleigh component works reasonably well.

## 3.3 Small-Scale Statistics

### Envelope Distribution

We first investigate the probability density function (PDF) of the *narrowband* case, using the the Akaike information criteria (AIC) [17, 18]. The Rayleigh, Ricean, Nakagami-m, Weibull, and lognormal distributions are considered as potential candidates for modeling the distribution of fading amplitudes.[37] The AIC favors the Ricean

---

[34] This was measured when the person was walking approximately in the middle between the two rails. While the following case was not measured in our campaign, we conjecture that a person walking very closely to either Tx or Rx would result in power fluctuations even for the 8 m case.

[35] With some minor modifications to the original function

[36] The smaller values of $A_{\mathrm{rel}}$ for the 8 m rail can be explained by the drop in the mean power of the deterministic component compared to the power of the random component. The latter is the less affected of the two when the link distance is increased.

[37] Maximum-likelihood estimates of the distribution parameters, required by AIC, were calculated for each small-scale ensemble; using closed-form expressions for Rayleigh and lognormal, grid-search for Ricean model, and results from [19] and [20] for the Nakagami-m and Weibull distributions, respectively.

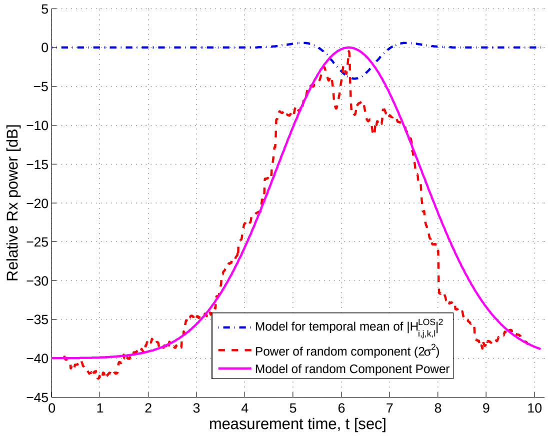

**Figure 5:** Time varying mean power of $H^{\mathrm{LOS,Res}}_{i,j,k,l}$. The intruder crosses the LOS around 6.2 sec. The plot corresponds to the Tx2-Rx5 link for the 2 m rail measurement.

distribution in a majority of the cases covering different rail widths. Therefore the Ricean distribution is selected as a representative model for the fading amplitude distribution of the measured channel, $H_{i,j,k,l}$. To this effect, a representative distribution of the temporal $K_{\mathrm{Rice}}$ is shown for all 18 channels in Fig. 6.

For the LOS component, a reliable determination of the appropriate PDF *shape* is not possible, due to the small number of available samples (note that in the narrowband case, the different tones increase the size of the available statistical ensemble). But from heuristic reasoning, $H^{\mathrm{LOS}}_{i,j,k,l}$ can also be assumed as Ricean, and its parameters determined from the measurements. For the latter Ricean fading process, the mean corresponds to $\sqrt{E_{l_{SSA}}[|H^{\mathrm{LOS}}_{i,j,k,l}|^2]}$, where the expression $E_{l_{SSA}}[\cdot]$ represents a windowed temporal average. The window-length is set to the temporal extent of an SSA. The temporal behavior of the mean can be observed in various subplots of Fig. 4. Furthermore the Rayleigh component of $H^{\mathrm{LOS}}_{i,j,k,l}$, denoted by $H^{\mathrm{LOS,Res}}_{i,j,k,l}$, can be separated as,

$$H^{\mathrm{LOS,Res}}_{i,j,k,l} = \frac{H^{LOS}_{i,j,k,l}}{\sqrt{E_{l_{SSA}}[|H^{LOS}_{i,j,k,l}|^2]}}. \tag{6}$$

In addition to investigating the aggregate measured channel, its random component, $H^{\mathrm{Res}}_{i,j,k,l}$ was also investigated for the relevant fading amplitude distribution. Though AIC determined the Ricean model as best fit in this case as well, the $K$-factors were quite small, $K_{Rice} \in [0, 1.5]$ natural units. In light of these observations,

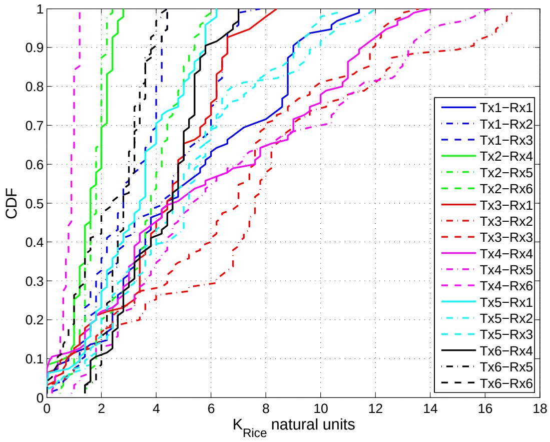

**Figure 6:** Distribution of temporal $K_{Rice}$ measured in the channel for the 4 m rail scenario. All 18 links are shown.

a Rayleigh process is proposed as an appropriate model for the fading of the residue component of the measured channel, $H^{\text{Res}}_{i,j,k,l}$. Quantitative results for the power of those components is discussed in connection with their average Doppler Spectrum, in the next section.

## Temporal Correlation of small-scale fading

The temporal correlation of small-scale fading, within a small-scale fading area, is a measure of how fast the channel changes in time, and is often characterized in terms of Doppler spectrum of the received signal [21]. The spectrum-width is conventionally expressed in terms of the root-mean-square (RMS) *Doppler-spread* [21], $\sigma_{\text{dopp}}$, which can be estimated as,

$$\sigma_{\text{dopp}} = \frac{\sum (f_l - f_m)^2 S(f_l)}{\sum S(f_l)}, \tag{7}$$

where $S(f_l)$ is the power spectral density (PSD) at frequency shift, $f_l$, and $f_m = \frac{\sum f_l S(f_l)}{\sum S(f_l)}$ is the mean Doppler shift. The time-variant Doppler power spectrum for each link was generated by first applying a short-time Fourier transform (STFT) to channel samples measured at each tone, subsequently, the spectra were averaged over the tones to get a unique spectrum associated with the link. The length of the STFT window was taken to be the 0.5 sec stationarity interval.

The Doppler PSD of $H^{\text{LOS,Res}}_{i,j,k,l}$ characterizes scattering of the extracted LOS component, and revealed a Laplacian shape,[38]

$$S_{\mathrm{LOS}}\,(f) = \frac{1}{\sqrt{2}\cdot\sigma_{\mathrm{dopp}}}\cdot\exp\left(-\frac{\sqrt{2}}{\sigma_{\mathrm{dopp}}}\cdot|f|\right). \tag{8}$$

The RMS Doppler spreads calculated according to Eq. (7) had values in the range, $\sigma_{\mathrm{dopp}} \in [8, 12]$ Hz. These spreads are relatively large compared to those measured in indoor environments, e.g., see [9]. However, the larger values of Doppler spreads for the measured outdoor scenario are plausible when one considers that the moving person contributes a greater fraction of the total spectrum power compared to an indoor scenario. This reasoning was validated by performing indoor measurements with a similar setup, where the measured spreads were on the order of 3 Hz.

The Doppler PSD of the random component, $H^{\mathrm{Res}}_{i,j,k,l}$, characterizes the spectral distribution of the residual power of the channel, after the LOS component has been removed. For the 2 and 4 m rails, the reflection off the person's body results in some distinct peaks in the spectrum, whereas for the 8 m rail measurements, no significant peaks were visible in the spectrum. Hence, in the sequel we discuss the spectrum only for the 2 and 4 m rail configurations. In order to simplify the analysis, spectra of different links from the 2 and 4 m rail measurements were combined together in an average spectrum for further investigations, refer to Fig. 7.[39] The spectrum was modeled as a sum of two Gaussian shaped functions. The first of these functions, $D_{\mathrm{s}}(t, f)$, centered at 0 Hz, represents the time-static component of the channel. While the second Gaussian curve, $D_{\mathrm{i}}(t, f)$, represents the time-variant component of the channel. The latter curve has a fixed RMS spread of 15 Hz, a time-varying mean (that goes through zero as the person passes through the LOS), and a time-varying strength (weak at 0, $t_0$, and 10 sec, and strongest when the person creates reflections around $t_0$).[40]. The functional forms of the two Gaussian shapes with their parameters are provided in Table 1. Together, these relations can be used to model the temporal evolution of the non-stationary spectrum of $H^{\mathrm{Res}}_{i,j,k,l}$. Fig. 8 shows the spectrum model generated with the information provided in Table 1. Note that the expressions in Table 1 model the spectrum profile only such that a scale factor needs to be specified separately to relate the residue component's power to the LOS power.

Within the spectrum model, the power scaling of the time-variant component, $D_{\mathrm{i}}(t, f)$, is dependent on the un-obstructed LOS power of the modeled link. Our analysis of the measured spectra revealed that the power ratio between the un-obstructed

---

[38] The Laplacian fit to the spectrum is not shown here due to space constraints.

[39] Prior to averaging, the link spectra were aligned relative to the time instant where the mean Doppler shift crosses 0 Hz. These instants for the spectrogram are interpreted as the LOS crossing instant, $t_0$, of the person walking between the rails. Alternatively, the $t_0$ values were also estimated from a temporal average of the extracted LOS power of each link,i.e., as the location in time of the most negative peak of the temporal average curves. The two approaches returned similar values verifying the estimated values.

[40] The 15 Hz spread is an average of the instantaneous RMS spreads along the measurement record length. While the height is adjusted to match, at each time instant, the area under the Gaussian curve to the power of the averaged spectrum.

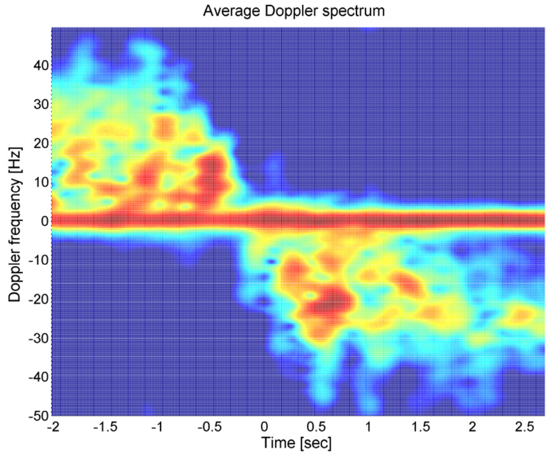

**Figure 7:** Averaged Doppler spectrum of the measured channel's random component $H^{\mathrm{Res}}_{i,j,k,l}$. The averaging is over all tones per link, and over multiple point-to-point links. The time-axis is labeled relative to $t_0$ which is at $t = 0$.

**Table 1:** Model for Doppler spectrum of $H^{\mathrm{Res}}_{i,j,k,l}$

| Symbol | Description | Function | Parameter | Unit |
|---|---|---|---|---|
| $D_{\mathrm{i}}(t,f)$ | Intruder's spectrum | $p(t)\exp\left(-\frac{(f-f_m(t))^2}{2F_{\mathrm{i}}^2}\right)$ | $F_{\mathrm{i}} = 12$ | Hz |
| $p(t)$ | Gaussian peak | $\exp\left(-\frac{(t-T_1)^2}{2W^2}\right) + \exp\left(-\frac{(t-T_2)^2}{2W^2}\right)$ | $T_1 = -0.6$ | sec |
| | | | $T_2 = 0.6$ | sec |
| | | | $W = 0.32$ | sec |
| $f_m(t)$ | Mean Doppler | $-B\frac{2}{\pi}\mathrm{atan}\,(Ct)$ | $B = 22$ | Hz |
| | | | $C = 2.5$ | - |
| $D_{\mathrm{s}}(t,f)$ | Static env. spectrum | $\exp\left(-\frac{f^2}{2F_{\mathrm{s}}^2}\right)$ | $F_{\mathrm{s}} = 1.4$ | Hz |

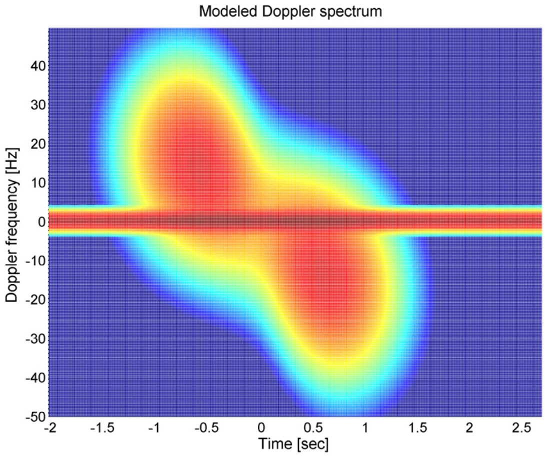

**Figure 8:** Modeled Doppler spectrum of the measured channel's random component $H^{\mathrm{Res}}_{i,j,k,l}$. The time-axis is labeled relative to $t_0$ which is at $t = 0$.

LOS power and the peak (over time) power of the dynamic component (i.e., the inverse temporal narrowband Rice factor), obtained by integrating the corresponding PSD over frequency, lies in the range between $-3$ to $-7$ dB. Furthermore, the power of the dynamic component of the residue channel peaks at the time instants $T_1$ and $T_2$. On the other hand, the power of the time-invariant residual component of the channel, modeled by the spectrum shape $D_{\mathrm{s}}(t, f)$, is independent of the link distance, and depends only on the site geometry such as location of nearby building structures and trees. For our measurements, this component had a constant power (integral of PSD over frequency), calculated to be $-25$ dB below the un-obstructed LOS power when antennas were exactly two meters apart. Note the reference to a particular LOS power is only to make the specification of the static component to be compatible with the rest of the generic modeling approach.

## 3.4 Multi-Channel Characteristics

In sensor network applications, nodes may often be distributed over a spatial region in close proximity to one another. It is of interest to observe, over time, the simultaneous influence of a scatterer's motion on the fading at different spatial positions. Our measurements with nodes on parallel rails provide some useful insights on such MIMO characteristics, i.e., correlation in the temporal evolution of various links. We use the temporal $K$-factor, measured at each link, to show the simultaneous fading behavior over multiple links, when a person walks between the rails, refer to Fig. 9. Some

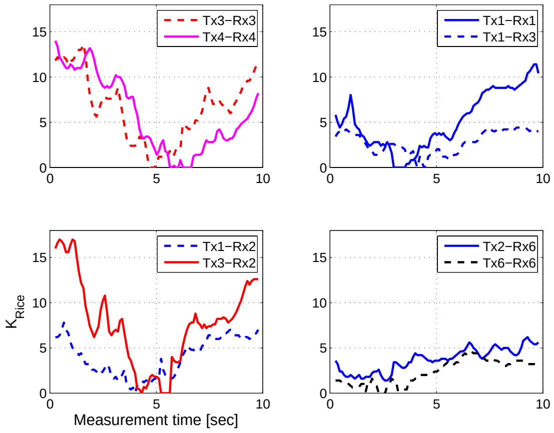

**Figure 9:** Evolution of temporal $K_{Rice}$ at multiple link ends. The plots correspond to a 4 m rail measurement, with a person walking between the rails with the orientation shown in Fig. 1.

qualitative observations on the link correlations are now provided:

- Links that have a similar orientation, relative to the walking person, have highly correlated fading, see e.g., the links Tx3-Rx3 and Tx4-Rx4.
- Consider two opposite-rail links, emanating from the same Tx, such as Tx1-Rx1 and Tx1-Rx3: while $K_{Rice}$ measured on the Tx1-Rx1 link increases in the interval between 4 and 5 sec, $K_{Rice}$ measured on Tx1-Rx3 link decreases during the same period. This behavior is explained when one considers that the walking person is moving away from Rx1, during the 4 to 5 sec period, so that the received time-variant component of the channel is gradually decreasing. Simultaneously, the person is getting closer to Rx3 such that the time-variant power, received at Rx3, from scattering/diffraction off the person's body is increasing. Since the temporal $K_{Rice}$, measured for stationary Tx/Rx, corresponds to a power ratio between the time-invariant component(s) of the channel and the components that are scattered/diffracted by a moving scatterer, the changes in the respective $K_{Rice}$ follow.
- The signal received at Rx2 from two opposite-rail nodes Tx1 and Tx3, which are spaced apart by 3 m on the same rail, are significantly correlated.
- Comparing a same-rail link, Tx2-Rx6, with an opposite-rail link, Tx6-Rx6, that is spatially proximal and has approximately the same link distance, one observes that the time-variant scattering component is stronger for the opposite-rail link, resulting in a smaller $K_{Rice}$ for the first four seconds of measurement time,

i.e., the person passing that end of the rail. When the scattering/reflection component received off the person's body has diminished, the $K_{Rice}$ values become similar for the two links.

It is noteworthy that all of the above effects describe the *temporal* correlation of the *small-scale-averaged* channel statistics; this is completely different from the standard MIMO correlation models, in which the correlation of instantaneous channel realizations is modeled [22].

# 4 Summary and Conclusions

This paper presented a characterization of an outdoor short-range sensor network scenario at 2.6 GHz. The terminals were stationary and placed at ground level in two parallel rails. The time-variance of the channel was due to a person walking between the rails. The influence of the person on Rx signal strength was most pronounced on the links where LOS blockage occurred due to body shadowing. On other links, specular/diffuse reflection off the person's body influenced the Rx signal strength, but to a lesser degree than the body-blockage case. An average stationarity interval of 0.5 sec was established for the small-scale analysis. A narrowband characterization of the channel was performed. The channel was observed to be Ricean fading. The RMS Doppler spreads were measured in the range of 10 to 15 Hz; these relatively high values compared to similar indoor measurements are due to a fewer number of significant stationary scatterers. A generic approach was presented to model temporally correlated samples of the narrowband channel. The time-variant Doppler spectrum of the residue channel was shown to have a distinct pattern associated with the walking person (intruder). These characteristics can be valuable for early intruder detection schemes since significant spectral peaks are visible before the LOS crossing instant. Furthermore, the sign on the Doppler shifts can be used to obtain information on the direction of movement of the intruder, a characteristic which cannot be extracted from the analysis of the LOS component only. Sample results on link correlations were presented that provide useful insight into evolution of joint fading behavior of the links in the measured scenario. Future measurements will focus on a similar characterization for multiple people crossing the link with better tracking of their location during the measurement interval. Furthermore, a wider range of configurations for node placements is needed for a more detailed investigation into the influence of geometry of movement.

# Acknowledgments

This work was partly financed through the Swedish Foundation for Strategic Research, the High Speed Wireless Center at Lund University, and a grant from Vetenskapsrådet, the Swedish Science Council.

# References

[1] J. A. Gutiérrez, E. H. Callaway, and R. L. Barrett, *Low-Rate Wireless Personal Area Networks: Enabling Wireless Sensors with IEEE 802.15.4*. IEEE Press, 2003.

[2] A. Willig, K. Matheus, and A. Wolisz, "Wireless technology in industrial networks," *Proceedings of the IEEE*, vol. 93, no. 6, pp. 1130–1151, 2005.

[3] Y. Hong, W. Huang, F. Chiu, and C. Kuo, "Cooperative communications in resource-constrained wireless networks," *IEEE Signal Processing Magazine*, vol. 24, no. 3, pp. 47–57, 2007.

[4] A. F. Molisch, N. Mehta, J. Yedidia, and J. Zhang, "Performance of fountain codes in collaborative relay networks," *IEEE Transactions on Wireless Communications*, vol. 6, no. 11, pp. 4108–4119, 2007.

[5] A. F. Molisch and F. Tufvesson, "Multipath propagation models for broadband wireless systems," in *Digital Signal Processing for Wireless Communications Handbook* (M. Ibnkahla, ed.), ch. 2, pp. 2.1–2.43, CRC Press, 2004.

[6] C. Anderson, H. Volos, W. Headley, F. Muller, and R. Buehrer, "Low antenna ultra wideband propagation measurements and modeling in a forest environment," *Proc. IEEE Wireless Communications and Networking Conference*, pp. 1229–1234, 2008.

[7] C. See, R. Abd-Alhameed, Y. Hu, and K. Horoshenkov, "Wireless sensor transmission range measurement within the ground level," *Proc. Loughborough Antennas and Propagation Conference*, pp. 225–228, 2008.

[8] W. Merrill, H. Liu, J. Leong, K. Sohrabi, and G. Pottie, "Quantifying short-range surface-to surface communications links," *IEEE Antennas and Propagation Magazine*, vol. 46, no. 3, pp. 36–46, 2004.

[9] P. Pagani and P. Pajusco, "Characterization and modeling of temporal variations on an ultrawideband radio link," *IEEE Transactions on Antennas and Propagation*, vol. 54, no. 11, pp. 3198–3206, 2006.

[10] C. Oestges, D. Vanhoenacker-Janvier, and B. Clerckx, "Channel characterization of indoor wireless personal area networks," *IEEE Transactions on Antennas and Propagation*, vol. 54, no. 11, pp. 3143–3150, 2006.

[11] J. Medbo, J.-E. Berg, and F. Harrysson, "Temporal radio channel variations with stationary terminal," in *Proc. IEEE VTC 2004-Fall*, vol. 1, pp. 91–95.

[12] R. Thoma, D. Hampicke, A. Richter, G. Sommerkorn, A. Schneider, U. Trautwein, and W. Wirnitzer, "Identification of time-variant directional mobile radio channels," *IEEE Trans. Instrumentation and Measurement*, vol. 49, pp. 357–364, 2000.

[13] http://www.skycross.com.

[14] R. Bultitude, “Methods for estimating and modeling consistency intervals, and the detection and simulation of changes on mobile radio channels,” in *COST 2100, TD(08) 424*, (Wroclaw, Poland), February 2008.

[15] M. Herdin and E. Bonek, “A MIMO correlation matrix based metric for characterizing non-stationarity,” in *Proc. IST Mobile and Wireless Communications Summit*, (Lyon, France), June 2004.

[16] A. Gehring, M. Steinbauer, I. Gaspard, and M. Grigat, “Empirical channel stationarity in urban environments,” in *Proc. 4th European Personal Mobile Communications Conference (EPMCC ’01)*, (Vienna, Austria), February 2001.

[17] H. Akaike, “Information theory and an extension of the maximum likelihood principle,” *Breakthroughs in Statistics, S. Kotz and N. L. Johnson, Eds. originally published in Proc. Int. Symp. Inf. Theory, Budapest, Hungary, 1973*, pp. 610–624, 1992.

[18] U. Schuster and H. Bolcskei, “Ultrawideband channel modeling on the basis of information-theoretic criteria,” *IEEE Transactions on Wireless Communications*, vol. 6, no. 7, pp. 2464–2475, 2007.

[19] Y. Chen and N. Beaulieu, “Estimators using noisy channel samples for fading distribution parameters,” *IEEE Transactions on Communications*, vol. 53, pp. 1274–1277, August 2005.

[20] N. Balakrishnan and M. Kateri, “On the maximum likelihood estimation of parameters of weibull distribution based on complete and censored data,” *Statistics and Probability Letters*, vol. 78, no. 17, pp. 2971–2975, 2008.

[21] A. F. Molisch, *Wireless Communications.* Chichester, U.K.: IEEE Press - Wiley, 2005.

[22] P. Almers, E. Bonek, A. Burr, N. Czink, M. Debbah, V. Degli-Esposti, H. Hofstetter, P. Kyoesti, D. Laurenson, G. Matz, A. Molisch, C. Oestges, and H. Oezcelik, “Survey of channel and radio propagation models for wireless MIMO systems,” *EURASIP Journal on Wireless Communications and Networking*, 2007.